Politecnico di Torino

ScuDo
Scuola di Dottorato ~ Doctoral School
WHAT YOU ARE, TAKES YOU FAR

Doctoral Dissertation

Doctoral Program in Electrical, Electronics and Communications Engineering

(36^{th}cycle)

A Novel Adaptive Algorithm for the Modeling and Regulation of Power Converters for Grid Applications

By

Mohammad Ahmed Qureshi

******

Supervisor(s):

Prof. Gianfranco Chicco, Supervisor

Prof. Ettore Francesco Bompard, Co-Supervisor

Politecnico di Torino

2024

Declaration

I hereby declare that, the contents and organization of this dissertation constitute my own original work and does not compromise in any way the rights of third parties, including those relating to the security of personal data.

Mohammad Ahmed Qureshi
2024

* This dissertation is presented in partial fulfillment of the requirements for **Ph.D. degree** in the Graduate School of Politecnico di Torino (ScuDo).

I would like to dedicate this thesis to my parents, my wife and my siblings for their love, patience and unconditional support during this time.

Abstract

While coal, oil, and natural gas contribute more than 60% to global electricity generation, they also bring hazardous issues due to the depletion of fossil fuels and global warming. Fortunately, renewable energy sources (RES) are promising to replace those fossil fuel based energy sources for electricity generation. After intensive research in the past two decades, microgrids composed of RES systems such as Photovoltaic (PV) arrays or wind turbines have emerged as a feasible and attractive alternative to traditional power system structure.

In modern microgrids, power converters are absolutely essential for converting renewable energy into electricity by connecting the converters to the grid. These converters enable bidirectional power flow, which is the defining feature of modern power grid and is essential for integrating distributed energy resources. Power converters also help maintain power quality, stability, and frequency regulation within the grid.

As the penetration of RES increases, the grid-connected converters supplied by RES are expected to establish and maintain voltage and frequency independently in *grid-forming* mode or to operate within the grid in *grid-following* mode.

To enable the converter to fulfill the tasks mentioned above, as well to dynamically respond to changes in load and generation, the control strategy of power converters has become of utmost importance. This thesis is therefore motivated to develop a novel adaptive control strategy for power converters to cope with fast transients and dynamic operating conditions.

This thesis proposes a new control strategy based on an adaptive control approach for regulating different DC-DC power converters as well as DC-AC power inverters. The proposed methodology is based on the Torelli Control Box (TCB) principles originally applied to power converters. The TCB approach is derived using the Lyapunov stability theory and can ensure asymptotic stability of the system. The

application of the TCB approach overcomes the disadvantage of the traditional non-linear control approach, that is, the requirement for the derivation of an appropriate energy function, which can be cumbersome and requires trial and error. The adaptive control approach presented in this thesis derives the control law for the system based on the Lyapunov approach without the need for Lyapunov function derivation while using only information of local measurements and parameters.

In addition to controlling dynamical systems, the TCB approach can also provide an alternative method for modeling systems whose dynamics are constrained by differential-algebraic equations. This is shown by the application of TCB approach for the modeling of Non-Isolated single input Multiple-Output DC-DC converters.

The TCB approach was then used to derive the control law for the regulation of Buck and Boost power converters in both ideal and non-ideal cases. The simulations highlight the effective response of the converter as compared to other nonlinear control techniques. The results were further verified by building hardware prototypes of both converters and testing the control performance in real time.

Similarly, the TCB approach was used for the Maximum Power Point Tracking application using a non-inverted buck-boost converter. The results show robust response and low steady-state errors even under extreme conditions of temperature and irradiance variation.

The approach was further tested on single-phase DC-AC inverter for a bidirectional Vehicle to Grid system. Comprehensive tests were conducted to show the response of the controller under different modes and different operating conditions. The effective performance of the controller in relation to others was highlighted.

Finally, the novel approach was tested for the regulation of three-phase inverters for UPS applications and Grid-Forming operations. The controller performance was tested initially in the Matlab/Simulink environment and further verified on a small-scale inverter prototype in the laboratory. The testing carried out by changing the load showed excellent performance in tracking the targeted output voltage.

Due to the difficulty and safety concerns of building a full-scale GFM inverter, the verification of its controller design was done through the use of a real-time simulator OP 5700 using RT-Lab software. The inverter was simulated using the latest FPGA based solver (ehs) from OPAL-RT. The results matched the ones that were concluded from Matlab/Simulink simulations.

Contents

List of Figures

List of Tables

Nomenclature

Acronyms / Abbreviations

AC	Alternating Current
AI	Artificial Intelligence
CBB	Ćuk Boost Combination
DAE	Differential Algebraic Equations
DC	Direct Current
DER	Distributed Energy Resources
EV	Electric Vehicles
FB	Extended Feedback
FL	Fuzzy logic
GFL	Grid-Following
GFL	Grid-following converters
GFM	Grid-Forming
GMPP	Global Maximum Power Point
HC	Hill-climbing
HCC	Hysteresis Current Control
HVAC	Heating, Ventilation, and Air Conditioning

IBS Integral Back-Stepping

IC Incremental Conductance

IGBT Insulated-gate Bipolar Transistors

ISMC Integral Sliding Mode Control

LC Lyapunov redesign based controller

LE Lyapunov Energy

LMMP Local Maximum Power Point

MOSFET Metal-Oxide-Semiconductor Field-effect Transistors

MPC Model Predictive Control

MPP Maximum Power Point

MPPT Maximum Power Point Tracking

MRAC Model Reference Adaptive Control

NN Neural networks

ODE Ordinary Differential Equation

P&O Perturb and Observe

PAC Phase and Amplitude Control

PB Passivity-Based

PCC Point of Common Coupling

PCFF Predicted Current Control with Fixed Switching Frequency

PID Proportional-Integral-Derivative

PLL Phase-Locked Loop

PP Phase to Phase

PV Photovoltaic

PWM Pulse Width Modulation

RES Renewable Energy sources

SCR Short-Circuit Ratios

SIMO Single-input multiple-output

SMC Sliding Mode Control

SMDVC Sliding Mode Direct Voltage control

TCB Torelli Control Box

THD Total Harmonic Distortion

UPS Uninterruptible Power Supply

V2G Vehicle to Grid

VFD Variable Frequency Drives

VSC Voltage Source Converter

ZBB Zeta Buck-Boost

Chapter 1

Introduction

In recent years, there has been a notable shift in power generation, with partial transitioning from centralized energy systems based on fossil fuels to distributed energy systems powered by renewable energy sources. These distributed energy sources constitute the modern microgrid, which is a localized and self-reliant network that can operate standalone or in coordination with the main grid. By integrating diverse energy sources such as solar or wind, and storage solutions, microgrids reduce the dependence on the centralized infrastructure, hence improving energy security, resilience and reliability of the grid.

The proliferation of microgrids has only been possible through the advancement of renewable energy system technologies such as Photovoltaic (PV) arrays, wind turbines etc. The increasing adoption of Renewable Energy Sources (RES) across the world is a direct result of the increasing efficiency and decreasing cost of these technologies. For contemporary renewable energy systems, interfacing the generators such as PV arrays and wind turbines with a power converter is essential to effectively contribute to the provision of grid power. The efficiency and feasibility of the entire system is dependent on the control and regulation of these power converters. In this thesis, the focus will be on the introduction of a novel adaptive control strategy that can be employed to regulate the output of these RES interfacing power converter topologies.

This chapter provides an overview of microgrids, emphasizing their significance in modern power systems. Additionally, it examines some power converter topologies

utilized to connect renewable energy resources to the grid, followed by a discussion on grid-forming and grid-following control strategies.

Subsequently, a section explores various Lyapunov methodologies, offering insights into their comparative advantages over conventional linear control techniques, followed by a section on the Lyapunov-based Torelli Control Box (TCB) methodology.

1.1 Modern Microgrids

1.1.1 Introduction to Microgrids

Wind and solar power have become key players in meeting the future energy needs and are crucial for achieving carbon neutrality by 2050. Thanks to technological advancements and cost reductions, the capacity of wind and solar photovoltaic systems for generating electricity has largely increased in the last twenty years, as illustrated in Fig. 1.1 [1]. Initially, due to the nature of their intermittent energy production, there were some difficulties over their integration with the conventional centralized power grid. However, the concept of microgrids has gained recognition as a promising way to seamlessly integrate more variable RES with the network. Microgrids offer improved reliability, resilience, and power quality services to address the evolving landscape of renewable energy integration.

Microgrids represent compact energy systems that integrate a variety of Distributed Energy Resources (DERs) and loads. Their distinctive feature lies in their capacity to operate both in connection with the main grid and autonomously in islanded mode. This dual functionality enhances the reliability and adaptability of energy distribution systems .

In comparing microgrids to conventional centralized energy production, the shift is evident. Unlike the traditional model of large-scale, remote power generation, microgrids prioritize local generation and consumption. The management of microgrids can be developed in such a way to minimize network losses, boost energy efficiency, and ensure a robust supply, particularly during disconnection from the main grid [2].

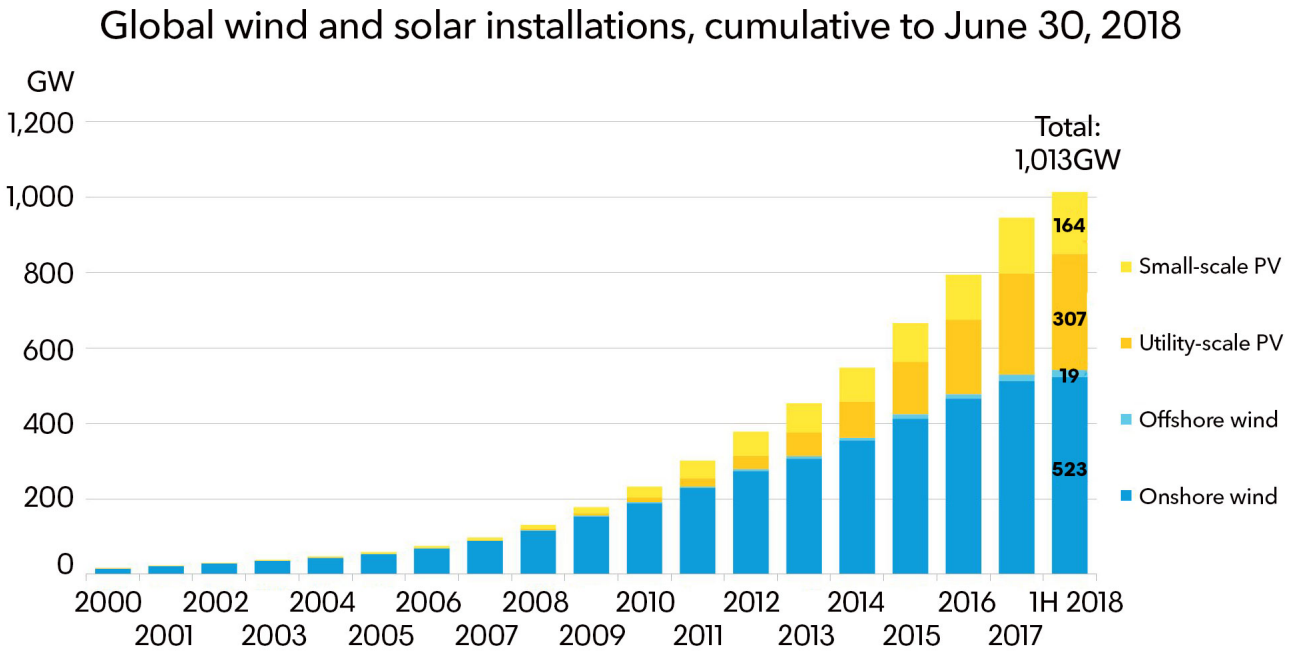

Fig. 1.1 Increase in Global Installed capacity of Solar and Wind Power

Critical to the operation of microgrids is the incorporation of distributed energy storage sources. Batteries, flywheels, and supercapacitors play a pivotal role in balancing supply and demand, managing the RES intermittency, and providing backup power during grid disturbances.

Microgrids also exhibit a unique capability to drive the transition between the grid-connected and islanded modes. In grid-connected mode, the microgrid is synchronized with the main grid, contributing to the overall energy supply. In islanded mode, the microgrid operates independently, ensuring a reliable power supply during grid outages or emergencies. This dual-mode functionality enhances the resilience of the overall energy infrastructure.

The microgrids can be categorized further into Alternating Current (AC) and Direct Current (DC) types, each one with distinct characteristics. AC microgrids operate using the traditional grid-standard alternating current, enabling seamless integration with the existing power infrastructure. This makes them suitable for applications where compatibility with the main grid is crucial. On the other hand,

DC microgrids operate in direct current, often generated through renewable sources like solar panels. DC microgrids offer advantages such as higher efficiency in certain applications, especially in the case of low-voltage distribution. However, challenges arise when attempting to synchronize DC microgrids with the conventional AC grid due to differences in voltage levels and waveform. AC microgrids are more established and widely adopted, benefiting from the existing infrastructure, while DC microgrids showcase potential in specific contexts. The choice between AC and DC microgrids depends on the specific requirements of the application and the existing grid infrastructure.

In conclusion, microgrids embody a transformative approach to energy distribution. From historical experiments to modern technological integration, microgrids represent a resilient and decentralized solution capable of adapting to the evolving needs of the energy sector. The interconnected nature of their components, from diverse energy sources to dual-mode operation, positions microgrids as key assets in the future of sustainable and adaptable energy systems.

1.1.2 Role of Power Converters in Modern Microgrids

In contrast to conventional power systems, microgrid power sources typically rely on one or more power electronic converters to efficiently supply power to the connected loads. This is especially pertinent in the context of renewable energy, where sources such as wind, solar photovoltaic, have intermittent energy production and require a battery energy storage system. As illustrated in Fig. 1.2, these diverse energy sources are powered by power converter topologies and controllers responsible for regulating and maximizing their energy production. These power converters are essential for establishing a desirable DC link before the power is seamlessly integrated into the microgrid network through a voltage-source inverter.

Fig. 1.3 shows some of the basic DC-DC converter topologies used in renewable energy systems. The design and control of power electronics-based sources within the microgrid requires the development of precise mathematical models. These models serve a dual purpose; allowing the analysis of the behavior of the power converters and facilitating the design of their associated controllers that can take the precise nonlinearities of their system dynamics into account. Therefore, this section aims to address the main aspects of modeling these power converters.

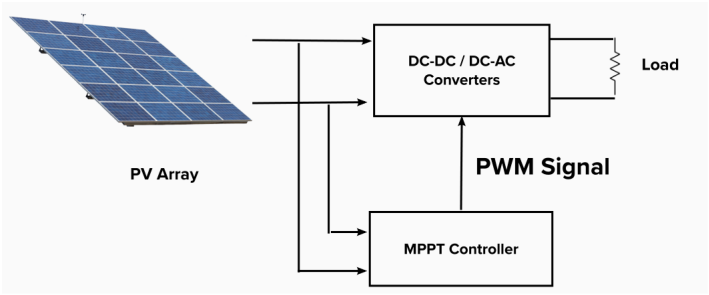

Fig. 1.2 Diagram of PV system interface with power converter and controller

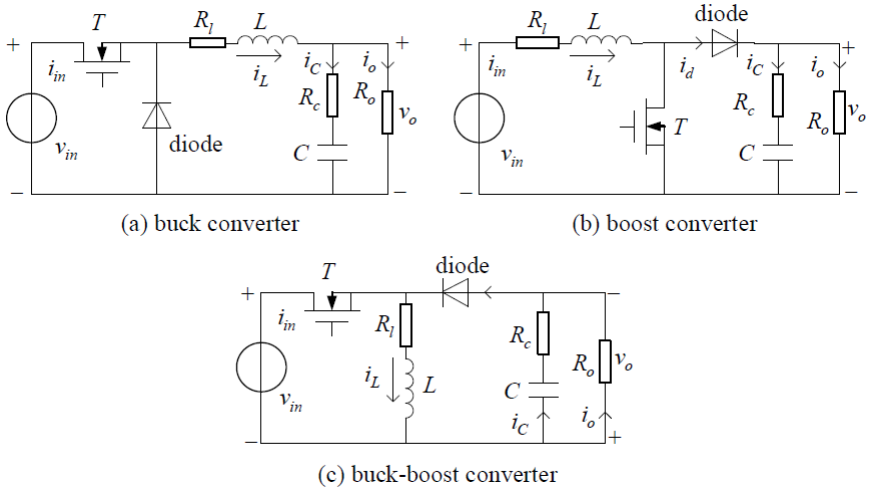

Fig. 1.3 (a) Buck Converter (b) Boost converter (c) Buck-Boost Converter

Steady state analysis and modeling of power converters

In microgrid systems, there is often a need to adjust the DC voltages of Distributed Energy Resources such as solar PV and battery energy storage systems. This adjustment is crucial to provide appropriate DC voltage levels to interface Voltage Source Converter (VSC). DC-DC converters, which perform voltage step-up and step-down functions, play a key role in this process. Common types of these DC converters include the basic buck, boost, and buck-boost converters, as depicted in Fig. 1.3.

Understanding the operational and analytical principles of these DC-DC converters is essential, as they serve as foundational elements for deriving other DC converters. This section focuses on the analysis of steady-state conditions initially, followed by the development of large-signal models for the converters using an averaged Pulse Width Modulation (PWM) switch model. It is important to note that,

in this model, parasitic parameters of the inductor and capacitor are not taken into consideration.

This section includes an example of modeling an ideal DC-DC Buck converter. Buck and Boost converters, frequently studied in literature, are fundamental power converter topologies used to step-down and step-up input voltage, respectively. Figure 1.4 depicts the circuits of these converters, which operate in two distinct modes. The total switching period, represented as T_s, includes a duration where the switch is turned ON, denoted as DT_s. Here, D represents the proportion of time the switch remains ON relative to the complete cycle of switching ON and OFF. In both converters, D serves as the system input and is controlled to regulate the converter voltage.

To derive the averaged mathematical model of Buck and Boost converters, one needs to derive their dynamical equations using the volt-second and charge-second balance.

In mode 1, the switch S in Fig. 1.4 (a) is considered closed. This makes the diode reverse biased. For this mode, one can derive the following equations for inductor voltage V_L and capacitor current I_C using Kirchhoff's voltage and current laws:

$$\begin{cases} V_L = V_g - V_o \\ I_C = I_L - V_o/R \end{cases} \tag{1.1}$$

In mode 2, the switch S is considered open. In this case, the diode is conducting. For this mode, one can derive the following equations for inductor voltage V_L and capacitor current I_C using Kirchhoff's voltage and current laws:

$$\begin{cases} V_L = -V_o \\ I_C = I_L - V_o/R \end{cases} \tag{1.2}$$

Now, using the principle of inductor volt-second balance which states that over one switching period, the net change in inductor current is zero, and the principle of charge-second balance which states that the net change in capacitor current over one switching period is zero, one can derive the following equations for the *averaged* inductor voltage and capacitor current:

$$\begin{cases} < V_L >= DV_g - V_o \\ < I_C >= I_L - V_o/R \end{cases} \tag{1.3}$$

where $< V_L >$ is the averaged inductor voltage across one switching period and $< I_C >$ is the averaged capacitor current over one switching period.

Finally, the full dynamics of the converter can be represented in terms of inductor current and capacitor voltage as follows:

$$\begin{cases} \dot{x}_1 &= \frac{-x_2}{L} + \frac{DV_g}{L} \\ \dot{x}_2 &= \frac{x_1}{C} - \frac{x_2}{RC} \end{cases} \tag{1.4}$$

where x_1 and x_2 are the inductor current and output voltage, and L, C and the inductor and capacitor values of the converters, respectively, and R is the load resistance. Both converters have been designed to operate in the continuous conduction mode under all testing conditions specified in this thesis.

Using the procedure specified above, the following equations for the Boost converter can be derived as well:

$$\begin{cases} \dot{x}_1 &= \frac{-(1-D)x_2}{L} + \frac{V_g}{L} \\ \dot{x}_2 &= \frac{(1-D)x_1}{C} - \frac{x_2}{RC} \end{cases} \tag{1.5}$$

From the equations of these converters, one can further derive the relationship between the input (duty ratio D) and the output of the system (output voltage V_o). This can be done by equating Equations (1.4) and (1.5) to zero. The following expressions are obtained:

$$V_o = DV_g \tag{1.6}$$

$$V_o = \frac{V_g}{(1-D)} \tag{1.7}$$

The resulting relationship between output voltage and duty ratio is shown in Fig. 1.5. As can be seen from the figure, for the Buck converter the relationship is linear while for the Boost converter is nonlinear.

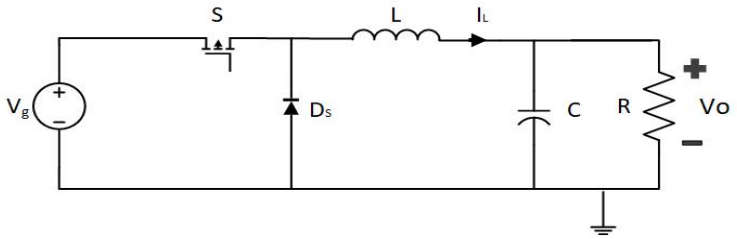

(a)

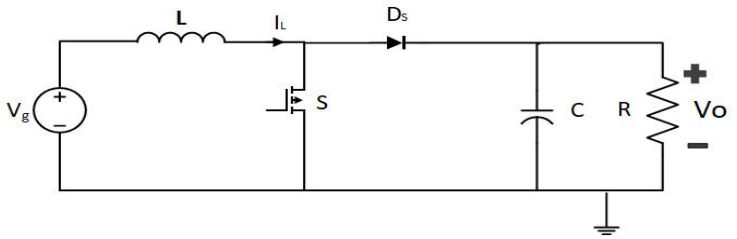

(b)

Fig. 1.4 (a) Buck Converter (b) Boost converter

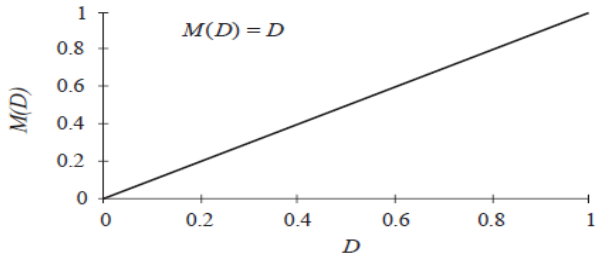

(a)

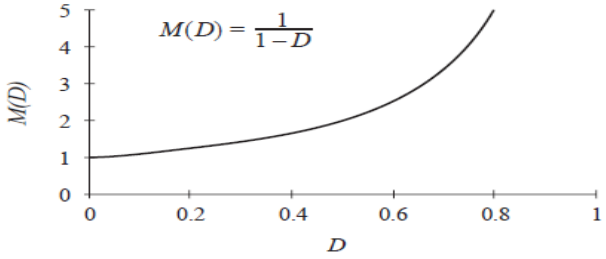

(b)

Fig. 1.5 Output voltage and Duty Ratio relationship for (a) Buck Converter (b) Boost converter

1.1.3 Role of Grid-following and Grid-forming Control for Microgrids

As the dependence on power electronics continues to grow, the need for advanced control strategies within electrical grids becomes more crucial. Two primary methodologies have emerged in shaping the dynamics of power systems: grid-forming and grid-following control strategies.

Grid-forming control represents a paradigm shift in power system operation, where the power electronic converters actively take on the responsibility of forming and maintaining the grid voltage and frequency. In this approach, the converters essentially emulate the behavior of traditional synchronous generators, providing stability and actively contributing to the grid operational characteristics.

On the other side, in grid-following control strategies the converters are integrated into an existing electrical grid, and tasked with aligning the active power delivery with the maximum available power from the primary energy source. While efficient in harnessing renewable energy, grid-following converters face challenges in grid stability, especially as the penetration of renewable energy system increases.

Understanding the principles of these control strategies is essential in dealing with the challenges of the evolving power grid. An overview of the control strategies along with their merits and demerits are presented below.

Grid-following control strategy for microgrids

A grid-following (GFL) converter functions similarly to a regulated current source. Typically, it incorporates a phase-locked loop to make sure that the converter's output is aligned with the grid phase angle. The phase angle, once determined, is pivotal for managing the current. The GFL converter's primary goal to inject required power to the grid is met by modulating the active and reactive currents. In scenarios of disturbances in the load, the GFL converter maintains a steady output current. Nonetheless, it lacks the capability to autonomously regulate the grid frequency and voltage, depending instead on an external voltage source or the grid itself for these reference values. Consequently, the GFL converter cannot function in isolated mode, nor can it address issues related to frequency fluctuations [3].

The GFL control scheme is quite popular for use in grid-tied converters. These converters serve as a bridge between the power grid and renewable energy sources, with GFL converters typically being outfitted with a PLL and a dual-loop control mechanism. The PLL is utilized to monitor the phase angle at the point of common coupling, while the vector control method is employed to fine-tune the active and reactive currents discharged into the grid. Under this control framework, the power grid is tasked with providing stable voltage and frequency support, with the converters themselves seldom engaging in voltage and frequency regulation [4].

Grid-forming control strategy for microgrids

In contrast to the GFL converter, the Grid-Forming (GFM) converter operates similarly to a controlled voltage source. Certain GFM control methods do not require the need for a phase-locked loop (PLL) to detect the grid voltage phase angle, achieving self-synchronization with the grid by emulating the synchronization characteristics of traditional synchronous generators. Unlike synchronous generators, which rely on kinetic energy stored in their rotors to stabilize frequency, GFM converters can respond more swiftly to frequency variations in the grid. The inherent ability of GFM converters to manage both frequency and voltage makes them well-suited for standalone, or islanded, operation modes.

Furthermore, it has been noted in some studies that employing a PLL in conjunction with current control might compromise the stability of power converters connected to a fragile grid. This is attributed to the GFL converter's reliance on tracking the voltage at the point of common coupling (PCC), which can be significantly influenced by its own output current in grids with low short-circuit ratios (SCR). On the other hand, GFM converters are capable of achieving self-synchronization by regulating their active power output, facilitating synchronization even with grids that have a low SCR. However, in robust grids with high SCR, minor shifts in phase between the converter-side and grid-side voltages can trigger substantial fluctuations in active power, potentially leading to overload conditions [5].

Different GFM control strategies have been proposed in the literature [6]. The main aim of these control strategies is to emulate the dynamics of synchronous machines especially from the point of view of the grid. This energy emulation is done through the use of storage devices and through controlling charging/discharging

of DC link capacitors. One way to classify these techniques is by the dynamics of the systems they try to replicate. Some of the major ones are as follows:

- Synchronous generator model-based
- Induction machine model-based
- Swing equation-based
- Frequency-power response-based

1.2 Introduction to Nonlinear Control Methodologies

Nonlinear control systems are systems that do not obey the superposition principle, meaning that the output of the system is not proportional to the input. Most systems in nature tend to be nonlinear. Thus, an accurate model of the complex intricacies of most systems requires the use of nonlinear modeling.

One of the advantages of nonlinear control systems lies in their ability to handle highly complex and diverse systems that linear methods may struggle to capture. Nonlinear control systems are particularly suitable for systems with strong nonlinearities or varying operating conditions. However, this flexibility comes at the cost of increased complexity in analysis and design.

Linear control has powerful methodologies that can be applied to systems that obey the superposition principle, such as the Laplace transform, Fourier transform, and root locus. However, linear control techniques may not be suitable for nonlinear systems, as they may not capture the true behavior of the system or may lead to inaccurate or unstable results.

Therefore, one way to deal with nonlinear systems is to linearize them, which means to approximate them by a linear system that behaves similarly in a certain region of interest. After linearizing a given nonlinear system it is possible to apply linear control techniques as long as the system operates near the point of linearization. Linearization is a useful technique, but it has some limitations, such as being valid only in a small region, being sensitive to uncertainties and disturbances, and losing some nonlinear features of the system.

Some advantages of nonlinear control systems over linear control systems are [7]:

- Nonlinear control systems can handle nonlinearities, such as saturation, hysteresis, backlash, friction, and dead zones, that may degrade the performance or stability of linear control systems.
- Nonlinear control systems can achieve better performance, such as faster speed, more accuracy, or reduced control energy, by exploiting the nonlinear characteristics of the system.
- Nonlinear control systems can deal with uncertainties, disturbances, and parameter variations that may affect the system, by using robust or adaptive control techniques.

However, just to be clear, compared to linear control systems, nonlinear control systems are more challenging to analyze and design, as they require more rigorous and less general mathematical tools, such as limit cycle theory, Poincaré maps, Lyapunov stability theory, and describing functions. Despite the increased complexity, the superior performance of these controllers and the ability to allow the system to be globally asymptotically stable makes the tradeoff worth it.

1.2.1 Introduction to Lyapunov-based Control Techniques

Lyapunov based control techniques are methods for designing nonlinear controllers for dynamical systems that ensure stability and performance. A dynamical system is a system whose state changes over time according to some rules or equations. Stability means that the system does not diverge or oscillate uncontrollably, but converges to a desired state or equilibrium. Performance means that the system achieves some objectives, such as minimizing energy consumption, maximizing throughput, or tracking a reference signal.

The main idea of Lyapunov based control techniques is to use a Lyapunov function, which is a scalar measure of the system state, to guide the control design. A Lyapunov function is usually chosen to be positive and decreasing along the system trajectories, meaning that it reflects the distance or error from the desired state or equilibrium. By controlling the system in such a way that the Lyapunov function

decreases over time, one can ensure that the system will eventually reach the desired state or equilibrium. This is called the Lyapunov stability criterion.

Building upon stability analysis, Lyapunov-based control techniques extend their reach to design controllers that ensure stability and convergence to desired states. By carefully selecting Lyapunov functions and utilizing their derivatives in the control design process, these techniques can guarantee global asymptotic stability even in the face of nonlinearities and uncertainties. Global asymptotic stability here refers to the behavior of the system which allows it to not only remain bounded but converge towards an equilibrium point as time goes to infinity, regardless of the initial conditions.

There are basically two types of Lyapunov-based control techniques:

- **Direct Method:**

  In this approach, the Lyapunov function is directly used in the design of the control law. The main advantage of this method is that it leads to simple design and analysis.

  For example: For a system with state input x and control input u, a direct Lyapunov control law might be designed as $u = -k\frac{dV}{dx}$ where V is the Lyapunov function and k is a pre-defined gain.

- **Indirect Method:**

  In this method, series of Lyapunov functions are constructed, each stabilizing a subsystem of the overall system. A very popular nonlinear control technique based on this approach is known as backstepping and it will be detailed below.

Popular nonlinear control techniques in the literature

Some types of nonlinear control methodologies are:

- **Feedback linearization**:

  This method transforms a nonlinear system into an equivalent linear system by applying a nonlinear feedback control law that cancels out the nonlinearities of the system. For example, consider the following nonlinear system:

$$\begin{cases} \dot{x}_1 = x_2 \\ \dot{x}_2 = -x_1 + x_1^3 + u \end{cases} \tag{1.8}$$

where x_1 and x_2 are the states and u is the control input. Applying the feedback control law $u = -x_1^3 + v$, where v is a new control input, the system becomes:

$$\begin{cases} \dot{x}_1 = x_2 \\ \dot{x}_2 = -x_1 + v \end{cases} \tag{1.9}$$

which is a linear system.

- **Sliding mode control**:

  This method forces the system to operate on a sliding surface, which is a subset of the state space where the system behaves as desired. For example, consider the following nonlinear system:

$$\begin{cases} \dot{x}_1 = x_2 \\ \dot{x}_2 = -x_1 + x_1^3 + u \end{cases} \tag{1.10}$$

  where x_1 and x_2 are the states and u is the control input. Choosing the sliding surface as $s = x_2 + x_1$, the control input is designed as:

$$u = -x_1^3 - k\text{sign}(s) \tag{1.11}$$

  where k is a positive constant. This control input ensures that the system reaches and stays on the sliding surface, where the system behaves as a linear system with the desired dynamics $\dot{s} = -k\text{sign}(s)$.

- **Backstepping**:

  This method designs a control input by recursively stabilizing the subsystems of a nonlinear system, starting from the last equation and moving backwards. For example, consider the following nonlinear system:

$$\begin{cases} \dot{x}_1 = x_2 \\ \dot{x}_2 = -x_1 + x_1^3 + u \end{cases} \tag{1.12}$$

where x_1 and x_2 are the states and u is the control input. Starting from the last equation, the control input is designed as:

$$u = -x_1^3 - k_1 x_2 + v \tag{1.13}$$

where k_1 is a positive constant and v is a new control input. This control input stabilizes the subsystem $\dot{x}_2 = -x_1 + x_1^3 + u$. Moving backwards to the first equation, the control input v is designed as:

$$v = -k_2 x_1 \tag{1.14}$$

where k_2 is a positive constant. This control input stabilizes the subsystem $\dot{x}_1 = x_2$. The final control input is:

$$u = -x_1^3 - k_1 x_2 - k_2 x_1 \tag{1.15}$$

which stabilizes the whole system.

- **Lyapunov Redesign**:

  Lyapunov redesign technique is a method for designing robust nonlinear controllers for uncertain dynamical systems by using the same Lyapunov function that guarantees the stability of the nominal system. The idea is to add a corrective control term that cancels out the effect of the uncertainty on the Lyapunov function, thus ensuring that the system converges to the desired equilibrium or trajectory. The corrective control term is usually chosen to be discontinuous and switching, depending on the sign of the uncertainty term.

  To illustrate the Lyapunov redesign technique, let us consider the following example:

  The system is given by

$$\begin{cases} \dot{x}_1 = x_2 + \delta_1(x_1, x_2) \\ \dot{x}_2 = -x_1 + u + \delta_2(x_1, x_2, u) \end{cases} \tag{1.16}$$

  where δ_1 and δ_2 are unknown bounded functions for some known positive constants ρ_1 and ρ_2.

The nominal system is obtained by setting $\delta_1 = \delta_2 = 0$, which is a linear system with the origin as an equilibrium point. A stabilizing control law for the nominal system is given by

$$u_0 = -kx_2 \tag{1.17}$$

where k is a positive constant. A Lyapunov function for the nominal system is given by

$$V_0(x_1, x_2) = \frac{1}{2}(x_1^2 + x_2^2) \tag{1.18}$$

which satisfies

$$\dot{V}_0 = -kx_2^2 \leq 0 \tag{1.19}$$

for the closed-loop nominal system.

The corrective control term is designed as

$$u^* = -\frac{1}{\rho_2}\text{sign}(\dot{V}_0 + kx_2^2) \tag{1.20}$$

where "sign" is the sign function. The augmented control law is given by

$$u = u_0 + u^* = -kx_2 - \frac{1}{\rho_2}\text{sign}(\dot{V}_0 + kx_2^2) \tag{1.21}$$

The time derivative of the Lyapunov function along the solutions of the full system is given by

$$\dot{V} = \dot{V}_0 + x_2\delta_1 + (-x_1 + u)\delta_2 \tag{1.22}$$

Using the bounds on δ_1 and δ_2, one obtains

$$\dot{V} \leq \dot{V}_0 + \rho_1(x_1^2 + x_2^2) + \rho_2(x_1^2 + x_2^2 + u^2)|\delta_2| \tag{1.23}$$

Using the augmented control law, one obtains

$$\dot{V} \leq \dot{V}_0 + \rho_1(x_1^2 + x_2^2) - \frac{1}{\rho_2}\text{sign}(\dot{V}_0 + kx_2^2)|\delta_2| \tag{1.24}$$

Since $\text{sign}(\dot{V}_0 + kx_2^2)|\delta_2| \geq |\dot{V}_0 + kx_2^2|$, one obtains

$$\dot{V} \leq -kx_2^2 + \rho_1(x_1^2 + x_2^2) \tag{1.25}$$

which is negative definite in x_2. Therefore, the system is globally asymptotically stable at the origin.

1.2.2 Torelli Control Box Methodology: Mathematical Formulation

Introduction to the Adaptive Torelli Control Box approach

As mentioned in the section above, the first step in the derivation of a control law for a nonlinear system through the use of the Lyapunov stability criterion is to use a scalar Lyapunov function. However, the main drawback of the Lyapunov theory is that it does not provide the tool set to derive this Lyapunov function for a general system. There is no straightforward way or an algorithm one can follow to derive these functions. Hence, for lossy or physical systems, sometimes the derivation of an appropriate Lyapunov function can become a challenge. In fact, the derivation of a procedure for building a suitable Lyapunov function has attracted considerable attention over the past three decades [8–11].

In the TCB approach, the idea is to take advantage of the direct Lyapunov approach the other way around. The TCB approach starts off by building a fictitious Ordinary Differential Equation (ODE) system starting from a Lyapunov function that is known to fulfill the stability criterion. This ensures that the chosen ODE converges to a stable equilibrium point. This allows the use of artificial ODE to control the system. The application of TCB approach basically gives a set of equations that can be used to directly derive the control for any general system, for which the system model is known, without having to go through the hit and trial process of finding a Lyapunov function and going through a tedious process of deriving the control law.

In this thesis a *modified model-reference adaptive* version of the TCB control law is formulated and applied. This approach is chosen because the adaptive control law can manage parametric uncertainties by estimating the uncertain plant parameters in real time and then use these estimates to derive an input control law. Among the

widely used Lyapunov-based nonlinear control techniques for deriving the control law are input-output feedback linearization and input-state feedback stabilization. These techniques reformulate the nonlinear system into a linear one using cancellation or state transformation mechanisms, respectively [12, 13]. However, these methods often cancel out beneficial nonlinearities in the converter system. In contrast, the backstepping technique avoids this issue by preserving useful nonlinear terms and even adding additional nonlinearities that can enhance the transient performance of the converter system. Adaptive backstepping allows for the recursive design of a controller by treating some state variables as "virtual control" and designing intermediate control laws for them [13]. A more advanced form of backstepping, known as the tuning function approach, achieves stabilization and tracking objectives while minimizing the set to which the parameters and states converge.

Another main approach for constructing an adaptive controller is the "model-reference adaptive control" methodology [14, 15]. In this approach, the aim is to make the adaptive controlled system track the reference trajectory of a model system.

In the modified model-reference adaptive control method, the adaptive mechanism is based on the TCB methodology. The TCB method has been conceived for solving nonlinear systems of equations and has been applied to different contexts. On the converter modeling side, the TCB approach has been used in [16] to transform the differential algebraic equations of non-isolated single-input multiple output DC-DC converters into a set of ordinary differential equations. The approach has been modified and adopted for control purposes of various converter topologies [17–20].

The algorithm for developing the modified reference adaptive TCB-based controller consists of three phases:

- Phase I requires the formulation of a reference model that generates the desired reference trajectory for the adaptive control to follow.
- Phase II evaluates the system's equilibrium point and derives reference trajectories for the state parameters and input, denoted as $\mathbf{x}^*$ and $\mathbf{u}^*$, respectively.
- Phase III requires the derivation the control law that directs the system trajectory to align with the reference trajectory of the model.

The algorithm for the derivation of the modified reference adaptive TCB-based controller can be broken down into three phases:

Mathematical formulation of the TCB control approach

Let's consider a nonlinear differential and algebraic equations system:

$$\dot{\mathbf{x}}(t) = \mathbf{f}(\mathbf{x}(t), \mathbf{u}(t)) \tag{1.26}$$

$$\mathbf{g}(\mathbf{x}(t)) - \mathbf{y}(t) = \mathbf{0} \tag{1.27}$$

where $\mathbf{x}(t)$, $\mathbf{u}(t)$ and $\mathbf{y}(t)$ are the vectors that contain the state variables, the control variables, and the algebraic variables, respectively, and t denotes time. For clarity, the explicit dependence on time of the variables will be omitted in subsequent equations. The objective is to minimize the error between the trajectory of the adaptive system and the reference trajectory of the model.

According to the TCB approach, the initial step is to formulate a reference model that provides desired trajectory for the output variable. This reference model can be designed in a way to fulfill the performance requirements such as rise time and settling time.

The coordinates of equilibrium point in the composite domain ($\mathbf{x}$, $\mathbf{u}$), denoted as ($\mathbf{x}$*, $\mathbf{u}$*), must satisfy the following equations:

$$\mathbf{f}(\mathbf{x}^*, \mathbf{u}^*) = \mathbf{0} \tag{1.28}$$

$$\mathbf{g}(\mathbf{x}^*) = \mathbf{y}_{r0} \tag{1.29}$$

The third step is the design of an adaptive control law that guarantees the asymptotic stability of equilibrium point. The adaptation mechanism is designed to allow minimization of following tracking errors with respect to the control signal $\mathbf{u}$:

$$\begin{aligned} \mathbf{e_x} &= \mathbf{W_x}(\mathbf{x} - \mathbf{x}^*) \\ \mathbf{e_u} &= \mathbf{W_u}(\mathbf{u} - \mathbf{u}^*) \\ \mathbf{e_f} &= \mathbf{f}(\mathbf{x}, \mathbf{u}) - \mathbf{f}(\mathbf{x}^*, \mathbf{u}^*) \end{aligned} \tag{1.30}$$

where $\mathbf{W_x}$ and $\mathbf{W_u}$ are diagonal matrices that contain the (positive) weights associated to each error referring to the state variables $\mathbf{x}$ and control variables $\mathbf{u}$, respectively. The term $\mathbf{f}(\mathbf{x}^*,\mathbf{u}^*)$ is null as it is estimated in an equilibrium point of the system.

Assuming $\mathbf{e} = [\mathbf{e}_\mathbf{x}^\mathrm{T}, \mathbf{e}_\mathbf{u}^\mathrm{T}, \mathbf{e}_\mathbf{f}^\mathrm{T}]^\mathrm{T}$, since the state vector $\mathbf{x}$ is $\mathbf{u}$-dependent, the controller design problem can be recast as follows:

$$\dot{\mathbf{x}}(\mathbf{u}) = \mathbf{f}(\mathbf{x}(\mathbf{u}), \mathbf{u}) \tag{1.31}$$

$$\mathbf{e}(\mathbf{x}(\mathbf{u}), \mathbf{u}) = \mathbf{0} \tag{1.32}$$

Therefore, the problem consists of evaluating the input vector $\mathbf{u}(t)$ such that each component of the error vector $\mathbf{e}$ is reduced to zero while simultaneously fulfilling the dynamic constraint given by (1.31).

A possible way to achieve this goal is based on the definition of the following Lyapunov function:

$$V = \frac{1}{2}\mathbf{e}^\mathrm{T}\mathbf{e} \tag{1.33}$$

which can be noticed to be a scalar positive semi-definite function. Now it should be noted that if the time derivative of the function V is proven to be negative definite (or negative semi-definite), then according to the Lyapunov theorem, the entries of the vector $\mathbf{e}(t)$ will asymptotically approach zero.

From (1.33) the time derivative of V can be evaluated as follows:

$$\dot{V} = \mathbf{e}^\mathrm{T}\dot{\mathbf{e}} \tag{1.34}$$

and because

$$\dot{\mathbf{e}} = \frac{\partial \mathbf{e}}{\partial \mathbf{u}}\dot{\mathbf{u}} \tag{1.35}$$

it results

$$\dot{V} = \mathbf{e}^\mathrm{T}\frac{\partial \mathbf{e}}{\partial \mathbf{u}}\dot{\mathbf{u}} \tag{1.36}$$

Now, enforcing the condition that $\dot{\mathbf{u}}$ changes according to the gradient of V:

$$\dot{\mathbf{u}}(t) = -K\left(\frac{\partial V}{\partial \mathbf{u}}\right)^\mathrm{T} = -K\left(\frac{\partial \mathbf{e}}{\partial \mathbf{u}}\right)^\mathrm{T}\mathbf{e} \tag{1.37}$$

where K is a positive constant, it follows:

$$\dot{V}(t) = -K\mathbf{e}^{\mathrm{T}}\left(\frac{\partial \mathbf{e}}{\partial \mathbf{u}}\right)\left(\frac{\partial \mathbf{e}}{\partial \mathbf{u}}\right)^{\mathrm{T}}\mathbf{e} \tag{1.38}$$

The expression (1.38) is a quadratic form that is surely negative semi-definite. This proves that to guarantee the asymptotic stability of the equilibrium point $\mathbf{x}^*$, the control signal $\mathbf{u}(t)$ must be generated according to (1.37). This in fact guarantees, with the asymptotic stability of V, the minimum of the error $\mathbf{e}$.

Discussion on the effects of gain parameters

The chosen value of gain parameter K, introduced in equation (1.37) affects the rate of convergence of the designed algorithm. Through simulations and different applications of the TCB approach, it has been observed that an increase in the value of gain K increases the rate of convergence to a certain extent. However, increasing the value of gain beyond a certain threshold introduces oscillations in the control system. Specific cases will be discussed in the next chapters.

Similarly, the value of weights $\mathbf{W_x}$ and $\mathbf{W_u}$ are varied to control the trade-off between low overshoot and fast tracking.

1.3 Primary Contribution of the Thesis

In this thesis, the potential of a novel Torelli Control Box approach for its applications to different aspects of the use of power converters for energy system applications has been explored. These applications can be summarized as follows:

- Use of TCB approach for converting dynamics constrained by Differential Algebraic Equations into Ordinary Differential equations. This is verified by the application on Non-Isolated Single Input Multiple Output converter topologies such as Zeta-BuckBoost converter and Ćuk Boost combination converter. The content of this research has been published in [16].
- The regulation of Buck and Boost DC-DC converter topologies for both ideal and non-ideal cases. The simulations compared with other Lyapunov based

methodologies and verified through practical hardware implementation of the converters. This part of the research has been published in [17, 20].

- Implementation of a novel maximum power point tracking (MPPT) algorithm based on TCB approach that shows effective performance under conditions of temperature and irradiance variations. The results have been published in [19].
- Allowing the regulation of a single-phase inverter for bidirectional power flow in a Vehicle to Grid (V2G) application. The results have been published in [18].
- Regulation of a three-phase inverter for its application as uninterruptible power supply (UPS) and for its application as a Grid-forming Inverter. The application and performance of controller further verified by implementation of a hardware prototype setup in laboratory. The relevant papers for this part of research have been written and submitted for publication.

1.4 Thesis Outline

The next chapters of the thesis are organized as follows:

- Chapter 2 shows the application of the TCB approach for the modelling of Non-Isolated Single Input Multiple Output DC-DC converters.
- Chapter 3 addresses the application of TCB approach, which is verified first on an ideal case of Buck and Boost converters in Section 3.1, followed by its application for MPPT using Noninverting Buckboost converter in Section 3.2, followed by a practical demonstration of its application on Non-ideal Buck and Boost converter taking into account parametric nonidealities in Section 3.3. The final section of the chapter shows how the TCB approach can be applied to a V2G system.
- Chapter 4 shows the formulation of the TCB approach for a UPS application.
- Chapter 5 shows the application of the TCB approach for the control of a grid-forming three-phase inverter.

- Chapter 6 illustrates the experimental verification of the controller design by building a three-phase inverter prototype in the laboratory.
- Chapter 7 contains the conclusions of the thesis.

Chapter 2

Modeling of Non-isolated Single-Input Multiple-Output DC-DC Converters with Artificial Dynamics

Switching DC-DC converters are inherently nonlinear circuits. These circuits can be modeled using state-space representations, which are derived from differential equations and incorporate discrete variables to indicate the on/off positions of the switches. To simplify this complex mathematical representation, state-space averaged modeling was introduced by [21]. This technique replaces the discrete state-space representation of the circuit with an average representation over the switching period, effectively substituting the switch position variable with the duty cycle of the switching period [22]. Consequently, a single equation with continuous variables can describe the averaged state-space model.

State-space averaged modeling preserves the nonlinear nature of the circuit and allows for the representation of low-frequency dynamics without requiring assumptions about small-signal analysis [23]. However, this method cannot address instability near the switching frequency or chaotic behavior [24]. An alternative approach, discrete-time modeling [25], considers a sequence of time intervals corresponding to switching cycles, which can address sub-harmonic instability but not chaos, which requires methods like iterated non-linear mapping [26].

Single-input multiple-output (SIMO) DC-DC converters, composed of interconnected DC-DC converters of various types, are favored in numerous applications due

to their modularity, flexibility, and ability to provide multiple outputs from different structures [27]. Non-isolated SIMO converters, which do not use transformers for electrical isolation, benefit from a reduced component count and a more compact circuit design [28]. However, modeling these converters is challenging due to state jumps, governed by Differential Algebraic Equations (DAE) rather than ordinary differential equations, due to algebraic links among the states.

The resolution of algebraic equations can be complex, but converting them into an Ordinary Differential Equation (ODE) system can simplify the process. A significant hurdle lies in developing averaged ODE models for switched systems controlled by a Differential Algebraic Equation (DAE) system. Researchers have proposed various approaches to tackle this issue.

Some studies have explored modeling switched capacitors by taking into account the energy losses that occur when capacitors are connected in parallel [29]. Other research has utilized an incremental graph method to determine steady-state voltage gains [30]. Additionally, a discrete-time framework has also been introduced for analyzing switched capacitors [31].

For systems with state jumps, a switched dynamic averaged modeling approach has been employed. This technique incorporates the use of quasi-Weierstrass transformation and the development of consistency projection operators to establish an equivalent model of the converter [32]. This approach has been applied to a specific type of non-isolated Single-Input Multiple-Output (SIMO) converter, where researchers constructed an averaged model using quasi-Weierstrass transformation in conjunction with consistency projection operators.

This chapter presents a novel approach to averaged modeling of non-isolated Single-Input Multiple-Output (SIMO) converters. The method transforms a Differential Algebraic Equation (DAE) system into an Ordinary Differential Equation (ODE) system by incorporating artificial dynamics through the TCB approach. This marks the first application of TCB-based methodology to the complex task of modeling non-isolated SIMO DC-DC converters.

In the TCB approach, algebraic variables within the DAE are treated as control variables in a system designed to minimize algebraic equations. This is achieved through the convergence of an artificial dynamic system at each analytical time step. The method also allows for the inclusion of sensitivity functions. The minimization process employs a standard ODE solver, with convergence assured by meeting

the criteria for asymptotic convergence to the solution point, in accordance with Lyapunov theory.

A key advantage of this contribution is the ease with which the TCB method can be integrated into widely-used solvers like Simulink. The chapter demonstrates the application of this technique to two specific non-isolated SIMO DC-DC converters, showcasing the formation and resolution of their averaged models.

The chapter's structure is as follows: The subsequent section 2.1 revisits the fundamentals of the TCB method and outlines the formulation of the ODE system. Following this, case studies are presented in section 2.2, applying the TCB method to a Zeta Buck-Boost converter and a Ćuk Boost Combination converter. The chapter concludes with a summary of key findings and implications.

2.1 Mathematical Formulation of the ODE with Artificial Dynamics

Let us consider the DAE system with differential equations:

$$\dot{\mathbf{x}} = \mathbf{f}(\mathbf{x}, \mathbf{y}, t) \tag{2.1}$$

and algebraic equations:

$$\mathbf{g}(\mathbf{x}, \mathbf{y}, t) = \mathbf{0} \tag{2.2}$$

where t denotes the artificial time considered for this problem, while $\mathbf{x}$ and $\mathbf{y}$ are the vectors that contain the state variables and the algebraic variables, respectively. Let us transform the algebraic constraint (2.2) into the determination of the algebraic variables $\mathbf{y}$ that minimize the following quadratic function (the superscript T indicates transposition) at each time t:

$$W(\mathbf{y}) = \frac{1}{2}\mathbf{g}^{\mathrm{T}}\mathbf{g} \tag{2.3}$$

The time derivative of the function $W(\mathbf{y})$ is:

$$\dot{W} = \mathbf{g}^{\mathrm{T}}\dot{\mathbf{g}} = \mathbf{g}^{\mathrm{T}}\frac{\partial \mathbf{g}}{\partial \mathbf{y}}\dot{\mathbf{y}} \tag{2.4}$$

It is now assumed that $\dot{\mathbf{y}}(t)$ changes in the direction of the gradient of $W(\mathbf{y})$ [33]:

$$\dot{\mathbf{y}}(t) = -K \cdot \left(\frac{\partial W}{\partial \mathbf{y}}\right)^{\mathrm{T}} = -K \cdot \left(\frac{\partial \mathbf{g}}{\partial \mathbf{y}}\right)^{\mathrm{T}} \mathbf{g} \tag{2.5}$$

where K is a positive constant, so that the following quadratic form is obtained:

$$\dot{W}(t) = -K \cdot \mathbf{g}^{\mathrm{T}} \left(\frac{\partial \mathbf{g}}{\partial \mathbf{y}}\right) \left(\frac{\partial \mathbf{g}}{\partial \mathbf{y}}\right)^{\mathrm{T}} \mathbf{g} \tag{2.6}$$

The time derivative of $W(\mathbf{y})$ is a quadratic form and is certainly negative semi-definite, while $W(\mathbf{y})$ is positive semidefinite and is equal to zero in the equilibrium point. The Lyapunov conditions are then satisfied, and the trajectory of $\mathbf{y}(t)$ converges asymptotically to a stable equilibrium point. Furthermore, it is possible to write the sensitivity function by deriving (2.1) with respect to the algebraic variables $\mathbf{y}(t)$:

$$\frac{d\dot{\mathbf{x}}}{d\mathbf{y}} = \left(\frac{\partial \mathbf{f}}{\partial \mathbf{x}}\right) \left(\frac{\partial \mathbf{x}}{\partial \mathbf{y}}\right) + \frac{\partial \mathbf{f}}{\partial \mathbf{y}} \tag{2.7}$$

In summary, the DAE system equations (2.1) and (1.29) can be solved by solving the following ODE system:

$$\begin{cases} \dot{\mathbf{x}} = \mathbf{f}(\mathbf{x}, \mathbf{y}, t) \; \dot{\mathbf{y}} = -K \cdot \left(\frac{\partial \mathbf{g}}{\partial \mathbf{x}} \cdot \frac{\partial \mathbf{x}}{\partial \mathbf{y}} + \frac{\partial \mathbf{g}}{\partial \mathbf{y}}\right)^{\mathrm{T}} \mathbf{g} \\ \frac{d\dot{\mathbf{x}}}{d\mathbf{y}} = \frac{\partial \mathbf{f}}{\partial \mathbf{x}} \cdot \frac{\partial \mathbf{x}}{\partial \mathbf{y}} + \frac{\partial \mathbf{f}}{\partial \mathbf{y}} \end{cases} \tag{2.8}$$

2.2 Applications to Non-isolated SIMO Converters

2.2.1 Dynamic Behavior of SIMO Zeta Buck-Boost and Ćuk Boost Combination Converters

In this section we explore the application of the TCB methodology to two specific SIMO converter designs: the Zeta Buck-Boost (ZBB) and the Ćuk Boost Combination (CBC) [34]. SIMO converters, which can generate multiple output voltages, are increasingly important in fields such as renewable energy systems, microelectronics, lighting, and electric vehicles [35, 36]. The ZBB converter integrates the Zeta and Buck-Boost topologies in a way that they share a switch and an inductor at the input and can provide bipolar output voltage and Buck-Boost functionality with a single

switch. This design simplifies the controller and enhances cost-effectiveness and efficiency due to fewer components [35]. Similarly, the CBC converter combines boost and Ćuk topologies to provide two output voltages with the same polarity. A challenge in modeling ZBB and CBC converters is that their dynamics are described by differential-algebraic equations (DAE) rather than ordinary differential equations (ODE), which prevents the use of traditional averaging methods to derive their steady-state models.

Fig. 2.1 displays the Zeta Buck-Boost converter. The small signal model for this converter has previously been derived using quasi-Weierstrass transformation and consistency projectors, as shown in [36, 28]. In this study, the TCB method is utilized to simulate the averaged model of both the ZBB and CBC converters.

2.2.2 Steady State Modeling of the ZBB Converter

The steady state parameters for the ZBB converter shown in Figure 2.1 are defined as follows:

$$\mathbf{x}^{\mathrm{T}} = \begin{bmatrix} x_1 \; x_2 \; x_3 \; x_4 \; x_5 \end{bmatrix}^{\mathrm{T}} = \begin{bmatrix} i_1 \; i_2 \; v_{C1} \; v_{C2} \; v_C \end{bmatrix}^{\mathrm{T}} \tag{2.9}$$

The converter has two modes of operation. In the first Mode, the diode are reverse biased and the switch is closed. If we define the total switching period as T_s and the duty cycle, i.e. the ratio of the duration for which the switch is on, to be D then the total ON period for Model 1 can be defined as $0 \leq t < DT_s$. By using Kirchhoff's voltage and current laws, we can derive the following equations for Mode 1:

$$\begin{cases} \dot{x}_1 &= \frac{V_g}{L_1} \\ \dot{x}_2 &= \frac{V_g - x_3 - x_4}{L_2} \\ \dot{x}_3 &= \frac{x_2}{C_1} \\ \dot{x}_4 &= \frac{x_2}{C_2} - \frac{x_4}{R_1 C_2} \\ \dot{x}_5 &= \frac{-x_5}{R_2 C} \end{cases} \tag{2.10}$$

For Mode 2, the diodes D_1 and D_2 are forward biased and the switch S is open and the interval can be mathematically defined as $DTs \leq t < T_s$, Again, using the Kirchhoff's voltage and current laws we get the following equations:

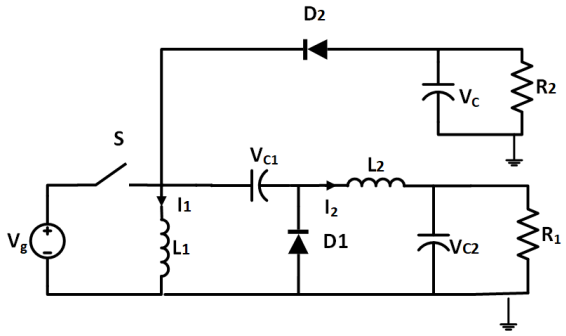

Fig. 2.1 Zeta Buck-Boost Converter

$$\begin{cases} \dot{x}_1 &= \frac{x_3}{L_1} \\ \dot{x}_2 &= \frac{-x_4}{L_2} \\ \dot{x}_3 &= \frac{-x_1}{C_1+C} - \frac{x_3}{R_2(C_1+C)} \\ \dot{x}_4 &= \frac{x_2}{C_2} - \frac{x_4}{R_1C_2} \\ x_5 &= x_3 \end{cases} \tag{2.11}$$

2.2.3 Application of the Torelli Control Box Approach

The converter's equation in Mode 2 reveals that its dynamics are governed by a Differential Algebraic Equation (DAE), which presents a challenge for deriving the averaged model using conventional volt-second or charge-second balance techniques. To address this issue, one potential strategy involves transforming the system equations in Mode 2 into a straightforward ODE format. This transformation is achieved through the application of the TCB methodology, which allows for the derivation of system equations both with and without the inclusion of sensitivity parameters.

TCB with Sensitivity Parameters

Using the procedure described in Section 2.1 the algebraic constraint is $g(x) : x_5 - x_3 = 0$, and the algebraic variable is $\mathbf{y} = [x_5]$. The sensitivity parameters are defined as follows: $w_1 = \frac{dx_1}{dx_5}$; $w_2 = \frac{dx_2}{dx_5}$; $w_3 = \frac{dx_3}{dx_5}$; $w_4 = \frac{dx_4}{dx_5}$.

The equations for Mode 2 are:

$$\begin{cases} \dot{x}_1 &= \frac{x_3}{L_1} \\ \dot{x}_2 &= \frac{-x_4}{L_2} \\ \dot{x}_3 &= \frac{-x_1}{C_1+C} - \frac{x_3}{R_2(C_1+C)} \\ \dot{x}_4 &= \frac{x_2}{C_2} - \frac{x_4}{R_1C_2} \\ \dot{x}_5 &= -K(1-w_3)(x_5-x_3) \end{cases} \tag{2.12}$$

The sensitivity parameter equations can be derived as:

$$\begin{cases} \dot{w}_1 &= \frac{w_3}{L_1} \\ \dot{w}_2 &= \frac{-w_4}{L_2} \\ \dot{w}_3 &= \frac{-w_1}{C_1+C} - \frac{w_3}{R_2(C_1+C)} \\ \dot{w}_4 &= \frac{w_2}{C_2} - \frac{w_4}{R_1C_2} \end{cases} \tag{2.13}$$

The sensitivity parameters $\dot{w}_2$ and $\dot{w}_4$ are not used in the modeling of the system. In Mode 2 the converter dynamics are no longer constrained by DAE. Hence, volt-second and charge-second balances are applied to derive the averaged model of the converter:

$$\begin{cases} <\dot{x}_1> &= \frac{DV_g}{L_1} + \frac{(1-D)x_3}{L_1} \\ <\dot{x}_2> &= \frac{D(V_g-x_3)}{L_2} - \frac{x_4}{L_2} \\ <\dot{x}_3> &= \frac{x_2D}{C_1} - \frac{x_1(1-D)}{C_1+C} - \frac{x_3(1-D)}{(C_1+C)R_2} \\ <\dot{x}_4> &= \frac{x_2}{C_2} - \frac{x_4}{R_1C_2} \\ <\dot{x}_5> &= \frac{-x_5D}{R_2C} - K(1-D)(1-w_3)(x_5-x_3) \end{cases} \tag{2.14}$$

TCB without Sensitivity Parameters

The averaged equations for the parameters of the converter are:

$$\begin{cases} <\dot{x}_1> &= \frac{DV_g}{L_1} + \frac{(1-D)x_3}{L_1} \\ <\dot{x}_2> &= \frac{D(V_g-x_3)}{L_2} - \frac{x_4}{L_2} \\ <\dot{x}_3> &= \frac{x_2D}{C_1} - \frac{x_1(1-D)}{C_1+C} - \frac{x_3(1-D)}{(C_1+C)R_2} \\ <\dot{x}_4> &= \frac{x_2}{C_2} - \frac{x_4}{R_1C_2} \\ <\dot{x}_5> &= \frac{-x_5D}{R_2C} - K(1-D)(x_5-x_3) \end{cases} \tag{2.15}$$

Table 2.1 Specifications of Zeta Buck-Boost Converter

Description of Parameters	Nominal Value
Capacitor, C_1	0.2280 mF
Capacitor, C_2	2.5024 µF
Capacitor, C	0.2280 mF
Inductor, L_1	4.1 mH
Inductor, L_2	4.1 mH
Resistance, R_1	24 Ω
Resistance, R_2	24 Ω
Switching frequency, f_s	50 kHz
TCB gain, K	10^6

The steady state values of the converter are given by the following equations:

$$\begin{cases} x_1 = \frac{D(1+D)V_g}{(1-D)^2R} \\ x_2 = \frac{DV_g}{(1-D)R1} \\ x_3 = \frac{-DVg}{(1-D)} \\ x_4 = \frac{DV_g}{1-D} \\ x_5 = \frac{-DVg}{(1-D)} \end{cases} \tag{2.16}$$

2.2.4 Simulation Results

The ZBB converter model underwent simulation in Simulink, utilizing the ODE 15s solver with a time step of 0.001 s. Table 2.1 presents the converter's specifications. Simulation outcomes for four parameters are illustrated in Fig. 2.2, while Fig. 2.3 displays results for the fifth parameter. To validate the derived model, a duty cycle step-up from D = 0.5 to 0.6 was introduced at time t = 4 s, followed by a step-down from D = 0.6 to 0.5 at t = 6 s. The converter model's output was then successfully compared against the theoretical values obtained from the previously derived steady-state equations, confirming the model's accuracy.

Fig. 2.3 includes a magnified view that further validates the TCB approach's capability to accurately reproduce rapid fluctuations. This precision is attributed to the selection of a sufficiently high TCB gain K (for instance, $K = 10^6$). These findings corroborate the exceptional effectiveness of the TCB methodology in analyzing dynamic systems, aligning with the conclusions drawn in [37].

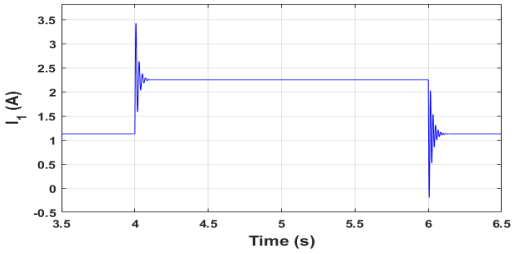

(a) Current I_1

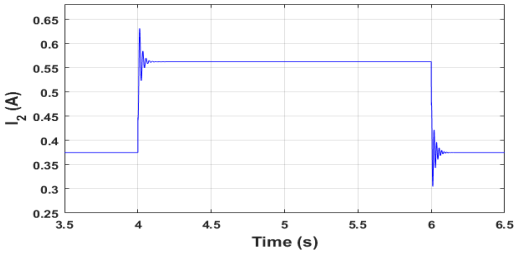

(b) Current I_2

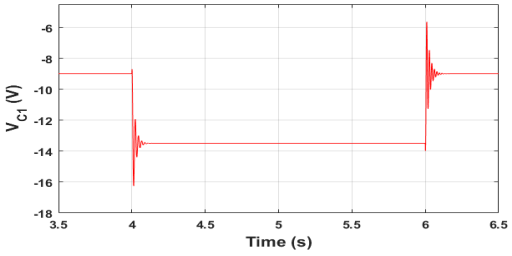

(c) Voltage V_{C1}

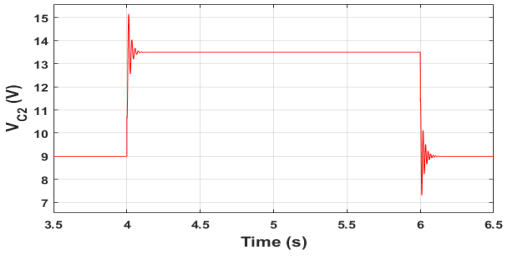

(d) Voltage V_{C2}

Fig. 2.2 Voltage and Current response of ZBB converter parameters in face of step change in duty cycle from 0.5 to 0.6.

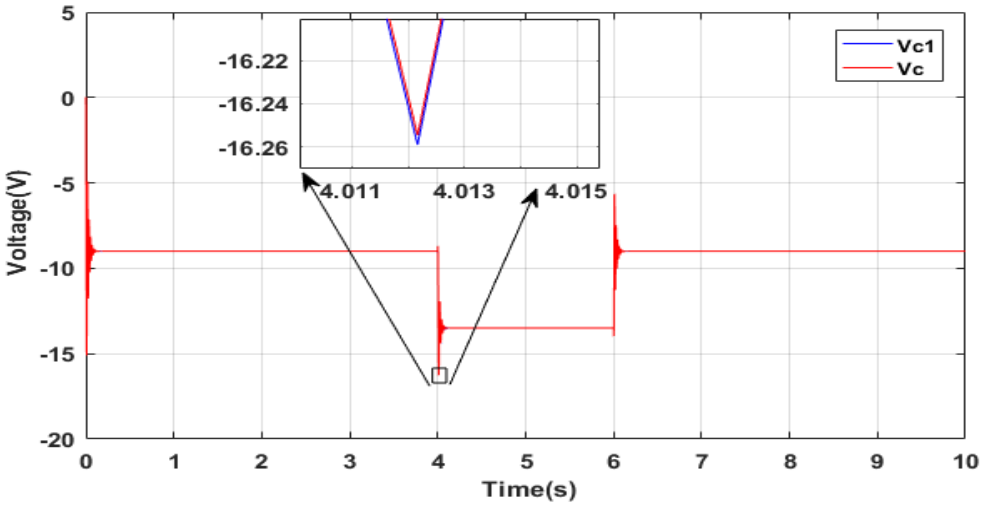

Fig. 2.3 Response of V_c with $K = 10^6$

2.2.5 Steady State modeling of a SIMO Ćuk Boost Combination Converter

The Ćuk Boost Combination converter is shown in Fig. 2.4. The steady state parameters are defined as follows:

$$\mathbf{x}^{\mathrm{T}} = \begin{bmatrix} x_1 \; x_2 \; x_3 \; x_4 \; x_5 \end{bmatrix}^{\mathrm{T}} = \begin{bmatrix} i_1 \; i_2 \; v_C \; v_1 \; v_2 \end{bmatrix}^{\mathrm{T}} \tag{2.17}$$

Following the same procedure as in Section 2.2.2, the steady state parameters in Mode 1 and Mode 2 are derived. In Mode 1, the switch S is closed and the diodes D1 and D2 are reverse biased. By applying Kirchhoff's voltage and current laws, the following equations are obtained:

$$\begin{cases} \dot{x}_1 &= \frac{V_g}{L_1} \\ \dot{x}_2 &= \frac{x_4 - x_3}{L_2} \\ \dot{x}_3 &= \frac{x_2}{C} \\ \dot{x}_4 &= \frac{-x_2}{C_1} - \frac{x_4}{R_1 C_1} \\ \dot{x}_5 &= \frac{-x_5}{R_2 C_2} \end{cases} \tag{2.18}$$

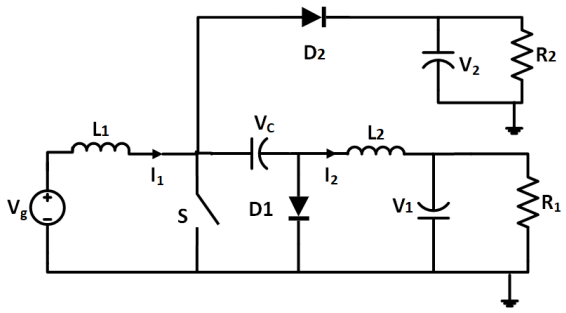

Fig. 2.4 Ćuk Boost Combination Converter

In Mode 2, switch S is open and diodes D_1 and D_2 are forward biased. Again using Kirchhoff's voltage and current laws the following equations are obtained:

$$\begin{cases} \dot{x}_1 &= \frac{V_g - x_3}{L_1} \\ \dot{x}_2 &= \frac{x_4}{L_2} \\ \dot{x}_3 &= \frac{x_1}{C+C_2} - \frac{x_5}{R_2(C+C_2)} \\ \dot{x}_4 &= \frac{-x_2}{C_1} - \frac{x_4}{R_1 C_1} \\ x_5 &= x_3 \end{cases} \tag{2.19}$$

2.2.6 Application of the Torelli Control Box Approach

To apply volt-second and charge-second balance, the DAE equation in Mode 2 is transformed into standard ODE form.

TCB with sensitivity parameters

Using the procedure described in Section 2.1, the algebraic constraint is $g(x)$: $x_5 - x_3 = 0$. The sensitivity parameters are defined as follows:

$$\begin{cases} w_1 = \frac{dx_1}{dx_5} & w_2 = \frac{dx_2}{dx_5} \\ w_3 = \frac{dx_3}{dx_5} & w_4 = \frac{dx_4}{dx_5} \end{cases} \tag{2.20}$$

Using the TCB approach, the equations for Mode 2 are:

$$\begin{cases} \dot{x}_1 &= \frac{V_g - x_3}{L_1} \\ \dot{x}_2 &= \frac{x_4}{L_2} \\ \dot{x}_3 &= \frac{x_1}{C+C_2} - \frac{x_5}{R_2(C+C_2)} \\ \dot{x}_4 &= \frac{-x_2}{C_1} - \frac{x_4}{R_1 C_1} \\ \dot{x}_5 &= -K(x_5 - x_3)(1 - w_3) \end{cases} \tag{2.21}$$

The sensitivity parameter equations can be derived as:

$$\begin{cases} \dot{w}_1 &= \frac{-w_3}{L_1} \\ \dot{w}_2 &= \frac{w_4}{L_2} \\ \dot{w}_3 &= \frac{w_1}{C_2+C} - \frac{1}{R_2(C_2+C)} \\ \dot{w}_4 &= \frac{w_2}{C_1} - \frac{w_4}{R_2 C_2} \end{cases} \tag{2.22}$$

In this case, the sensitivity parameters $\dot{w}_2$ and $\dot{w}_4$ are not used in the system modeling. Volt-second and charge-second balances are applied since the dynamics in Mode 2 are no longer constrained by a DAE, obtaining the averaged model:

$$\begin{cases} < \dot{x}_1 > &= \frac{V_g}{L_1} - \frac{(1-D)x_3}{L_1} \\ < \dot{x}_2 > &= \frac{x_4}{L_2} - \frac{D x_3}{L_2} \\ < \dot{x}_3 > &= \frac{x_2 D}{C} - \frac{x_5(1-D)}{(C_2+C)R_2} + \frac{x_1(1-D)}{(C_2+C)} \\ < \dot{x}_4 > &= \frac{-x_2}{C_1} - \frac{x_4}{R_1 C_1} \\ < \dot{x}_5 > &= \frac{-x_5 D}{R_2 C_2} - K(1-D)(1-w_3)(x_5 - x_3) \end{cases} \tag{2.23}$$

TCB without sensitivity parameters

The averaged equations for the parameters of the converter as follows:

$$\begin{cases} <\dot{x}_1> &= \frac{V_g}{L_1} - \frac{(1-D)x_3}{L_1} \\ <\dot{x}_2> &= \frac{x_4}{L_2} - \frac{Dx_3}{L_2} \\ <\dot{x}_3> &= \frac{x_2 D}{C} - \frac{x_5(1-D)}{(C_2+C)R_2} + \frac{x_1(1-D)}{(C_2+C)} \\ <\dot{x}_4> &= \frac{-x_2}{C_1} - \frac{x_4}{R_1 C_1} \\ <\dot{x}_5> &= \frac{-x_5 D}{R_2 C_2} - K(1-D)(x_5 - x_3) \end{cases} \tag{2.24}$$

The steady state values of the parameters can be derived from the volt-second and charge-second balance equations as:

$$\begin{cases} x_1 &= \frac{V_g}{(1-D)R_2} + \frac{2D^2 V_g}{(1-D)^2 R_1} \\ x_2 &= \frac{-DV_g}{(1-D)R_1} \\ x_3 &= \frac{V_g}{(1-D)} \\ x_4 &= \frac{DV_g}{1-D} \\ x_5 &= \frac{V_g}{(1-D)} \end{cases} \tag{2.25}$$

2.2.7 Simulation Results

Simulink was used for the simulation using the ODE 15s solver with a 0.001 s time step. Table 2.2 outlines the converter's specifications. The model's validation involved implementing a duty cycle D step change from 0.5 to 0.6 at time t = 0.4 s, followed by another step change from 0.6 to 0.5 at t = 0.6 s. Fig. 2.5 presents the CBC converter simulation results for four parameters, while Fig. 2.6 illustrates the outcomes for the fifth parameter. The parameter output values align with the converter's theoretical steady-state values, confirming the model's accuracy.

A magnified view in Fig. 2.6 further validates the TCB approach's ability to accurately reproduce rapid fluctuations. This precision stems from selecting a sufficiently high TCB gain K (for example, $K = 10^6$). These results reaffirm the TCB methodology's exceptional effectiveness in analyzing dynamic systems, extending its proven performance to the CBC converter as well.

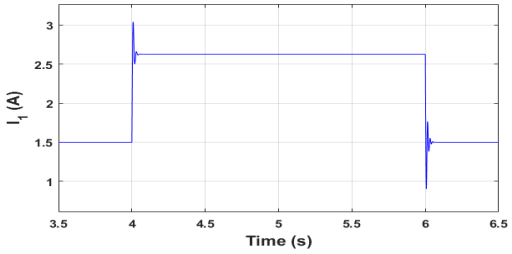

(a) Current I_1

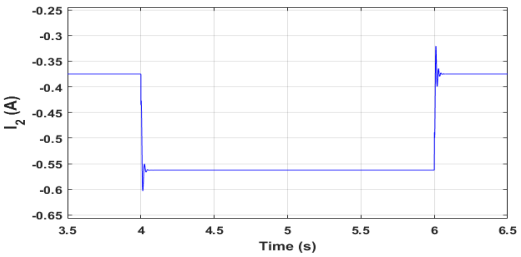

(b) Current I_2

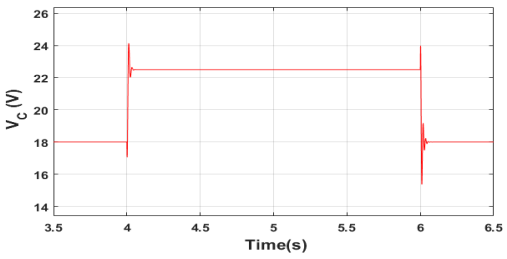

(c) Voltage V_C

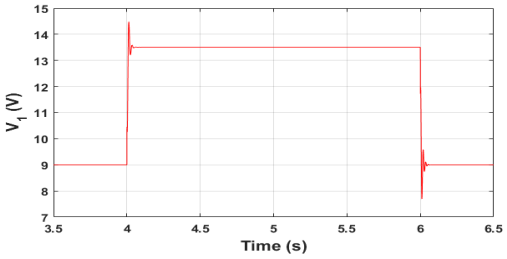

(d) Voltage V_1

Fig. 2.5 Voltage and current response of CBC converter parameters in face of step change in duty cycle from 0.5 to 0.6

Table 2.2 Specifications of Ćuk Boost Combination Converter

Parameters	Nominal Value
Capacitor, C	0.11 mF
Capacitor, C_1	2.10 µF
Capacitor, C_2	0.11 mF
Inductor, L_1	8.1 mH
Inductor, L_1	8.1 mH
Resistance, R_1	24 Ω
Resistance, R_2	24 Ω
Switching frequency, f_s	50 kHz
TCB gain, K	10^6

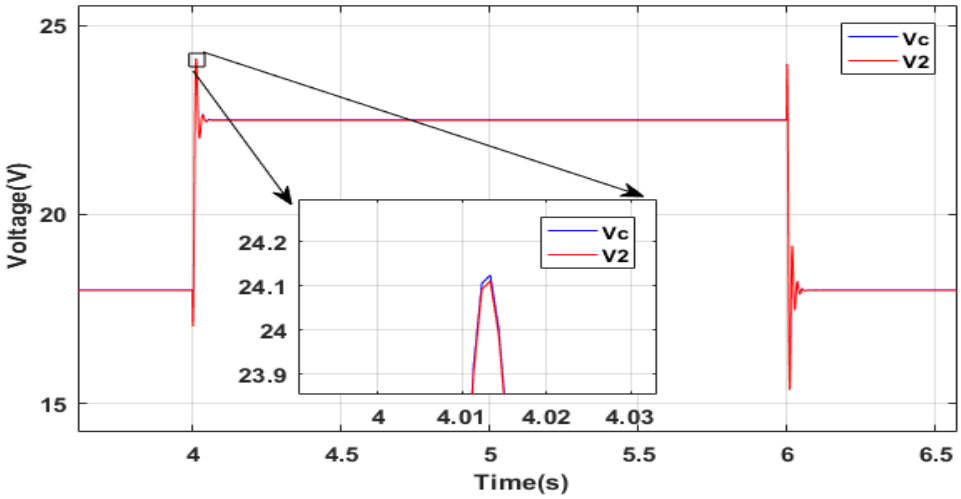

Fig. 2.6 Response of V_2 with $K = 10^6$

2.3 Concluding Remarks

The TCB methodology, applied in this chapter to derive an averaged dynamic model solvable with ODE equations, demonstrates robust and rigorously proven convergence, while offering straightforward implementation in established solvers like Simulink. This approach enables the development of averaged models for non-isolated SIMO converters using conventional volt and charge second balance techniques, even when algebraic equations are present. The artificial dynamic model constructed through the TCB method exhibits asymptotic stability and remarkable resilience to parametric variations. These findings, pioneering in this application domain, pave the way for widespread adoption of the TCB-based approach in analyzing switching dynamics across various converter topologies.

Chapter 3

Model Reference Adaptive Control for Power Converter Applications

This chapter demonstrates the viability and effectiveness of the TCB based Model Reference Adaptive Control (MRAC) approach for the regulation of power electronic converters. The control approach has been verified by its application on different power converter topologies of various complexities for different applications.

Power electronics heavily rely on DC-DC converters, which are integral components in diverse applications, including communication systems, industrial electronics, and large-scale renewable energy systems for grid formation. Ensuring these converters function according to their design specifications requires effective control mechanisms.

The control of these systems presents significant challenges due to their classification as variable-structure nonlinear systems. This classification stems from the presence of switching devices within the converters, which causes their dynamics to vary based on the switch state at any given moment. In the past, linear controllers such as Proportional-Integral-Derivative (PID) controllers were commonly used to manage these converters. This approach necessitated the linearization of the nonlinear system around its equilibrium point. However, this method had limitations, as the resulting linear controller typically only performed effectively within a narrow operational range near the equilibrium point, and its stability could not be guaranteed over a broader operational spectrum.

As a result, recent research has pivoted towards the development of nonlinear controllers for these power converters, utilizing the Lyapunov methodology. These nonlinear control strategies take into account the inherent nonlinearities of the model, thereby offering a wider range of stability. This shift in approach reflects the ongoing efforts to improve the performance and reliability of DC-DC converters across their full operational range [38].

This chapter addresses the application of the TCB technique for the regulation of various DC-DC and DC-AC topologies. The detailed mathematical modeling procedure of the power converters and the theory behind the derivation of the TCB control law are not repeated as they have already been presented in the previous chapter. Comparison of the TCB control approach with other nonlinear control techniques are provided to highlight the advantage of the proposed approach. Hardware implementation of the DC-DC power converter has also been provided to verify the performance of the controller in real time.

3.1 Application of the TCB approach to Ideal DC-DC Buck and Boost Converter Topologies

The ideal Buck and Boost converter models are shown in Fig. 1.3. The averaged mathematical model of the Buck and Boost converters, as mentioned in the previous chapter, can be derived using volt-second and charge-second balance as follows:

$$\begin{cases} \dot{x}_1 &= \frac{-x_2}{L} + \frac{DV_g}{L} \\ \dot{x}_2 &= \frac{x_1}{C} - \frac{x_2}{RC} \end{cases} \tag{3.1}$$

$$\begin{cases} \dot{x}_1 &= \frac{-(1-D)x_2}{L} + \frac{V_g}{L} \\ \dot{x}_2 &= \frac{(1-D)x_1}{C} - \frac{x_2}{RC} \end{cases} \tag{3.2}$$

where x_1 and x_2 are the inductor current and output voltage, and L, C and R are the inductor, capacitor and load resistance values of the converters, respectively.

3.1.1 Application of the TCB Control Approach to a Buck Converter

This subsection explores the implementation of the TCB approach through simulation on a Buck converter topology. Buck converters are employed to step down the input voltage of the converter. The controller's primary objective is to maintain the converter's reference voltage, denoted as V_o, despite fluctuations in input voltage or load resistance.

In applying the TCB control methodology to the Buck converter, we establish the reference model with $y_{r0} = V_0$. To determine the steady-state values of the desired variables, we set the left side of the equation (3.1) to zero. This process allows us to derive the necessary expressions for these steady-state values.

$$\begin{cases} x_1^* = \frac{y_{r0}}{R} \\ x_2^* = y_{r0} \\ u^* = \frac{y_{r0}}{V_g} \end{cases} \tag{3.3}$$

The next step is to set the problem of adaptive tracking control which consists of minimizing the following error functions:

$$\begin{cases} e_1 = x_1 - x_1^* \\ e_2 = x_2 - x_2^* \\ e_3 = u - u^* \end{cases} \tag{3.4}$$

From Equation (1.37), the expression for the input control of the converter can be derived as follows:

$$\dot{u} = -K[\frac{dx_1}{du}(x_1 - x_1^*) + \frac{dx_2}{du}(x_2 - x_2^*) + (1)(u - u^*)] \tag{3.5}$$

In this particular case, the gain variables have been set equal to unity. Considering the sensitivity parameters $w_1 = \frac{dx_1}{du}$ and $w_2 = \frac{dx_2}{du}$, the equations for deriving the

Table 3.1 Specifications of Buck Converter and Controller Gains

Description of Parameters	Nominal Value
Input Voltage, V_g	40 V
Reference Output Voltage, V_o	24 V
Capacitor, C	5 uF
Inductor, L	50 uH
Resistance, R	12 Ω
Switching frequency, f_s	100 kHz
TCB gain, K	10^4

sensitivity parameters of the Buck converter are:

$$\begin{cases} \dot{w}_1 & = -\frac{w_2}{L} + \frac{V_g}{L} \\ \dot{w}_2 & = -\frac{w_1}{C} - \frac{w_2}{RC} \end{cases} \tag{3.6}$$

3.1.2 Simulation Results for the Buck Converter

The Buck converter model depicted in Fig. 1.3(a) was simulated in the Simulink environment. Table 3.1 presents the converter specifications and controller gain value. To validate the converter control effectiveness, the system was subjected to step variations in both load resistance and input voltage.

Load resistance variations

The system operates with a nominal load of 12 Ω. At time t = 0.2 s, a step change alters the load from 12 Ω to 17 Ω, followed by a return to 12 Ω. Fig. 3.1 illustrates the resulting fluctuations in the Buck converter's average output voltage V_o and inductor current I_L.

The zoom shown in Fig. 3.1(b) demonstrates the absence of steady-state error in both the reference signal and output voltage. Notably, despite the abrupt load resistance change, the maximum output voltage overshoot remains below 24.072 V, constituting merely 0.30% of the steady-state value.

Input voltage variations

The Buck converter operates with a nominal input voltage of 40 V. At t = 0.2 s, a step change reduces the input voltage to 30 V, followed by a restoration to 40 V at t

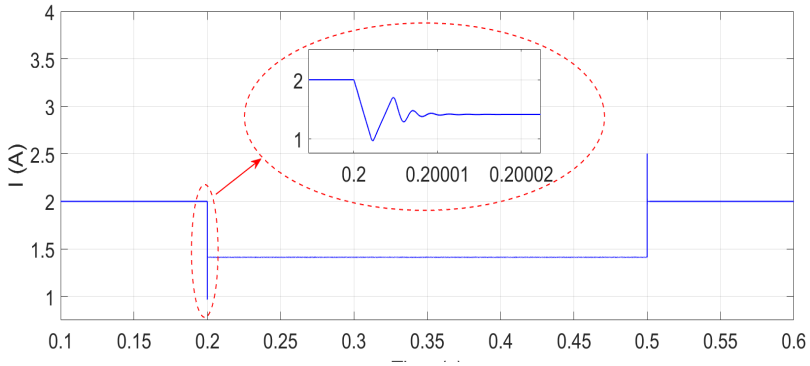

(a) Inductor current I_L

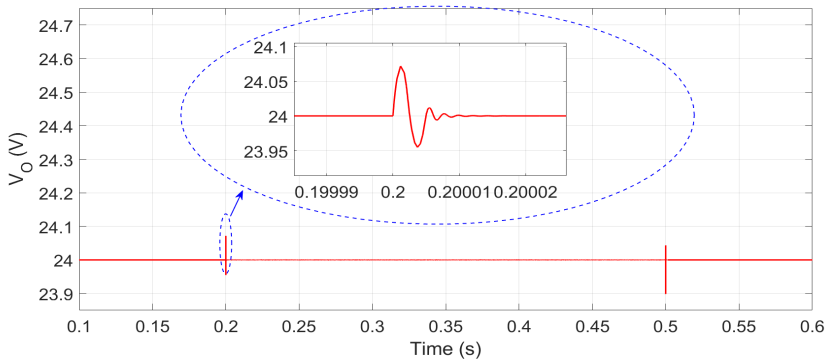

(b) Output voltage V_o

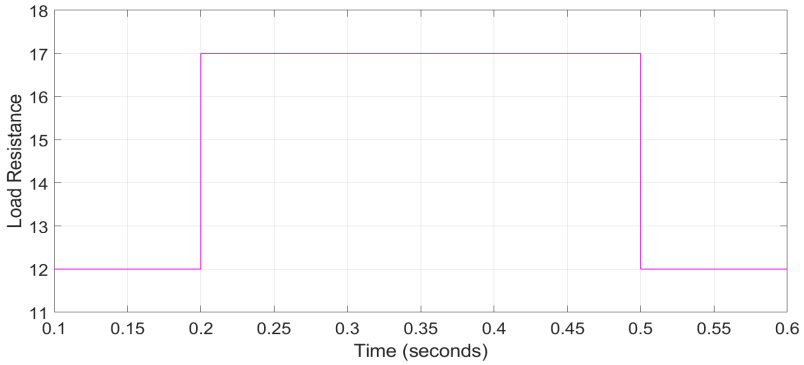

(c) Load resistance R

Fig. 3.1 (a) Inductor current and (b) Output voltage response of the Buck converter in face of (c) Load resistance variation from 12 Ω to 17 Ω

= 0.5 s. Fig. 3.2 displays the resulting alterations in the average output voltage and duty ratio.

Fig. 3.2(a) demonstrates the absence of steady-state error in reference voltage tracking. Notably, despite input voltage fluctuations, the Buck converter's output voltage variations remain in the mV range, barely perceptible in simulations without significant magnification. Fig. 3.2(b) further illustrates the converter's near-perfect tracking of the reference duty cycle, as evidenced by the Duty Ratio output.

3.1.3 Application of the TCB Control Approach to the Boost Converter

The development of the adaptive TCB control law for the boost converter follows a similar approach to that used for the Buck converter.

The reference model for the Boost converter is represented by the equation (3.2). In a manner similar to the Buck converter analysis, the next step involves developing expressions for the converter's reference state parameters and input. To calculate the steady-state values of these reference parameters, given a desired output (y_{r0}), we set the (3.2) equation to zero. This mathematical operation results in a set of expressions that define these steady-state reference values.

$$\begin{cases} x_1^* = \frac{y_{r0}^2}{RV_g} \\ x_2^* = y_{r0} \\ u^* = 1 - \frac{V_g}{y_{r0}} \end{cases} \tag{3.7}$$

Now we can define the following errors that can be minimized using the control law:

$$\begin{cases} e_1 = x_1 - x_1^* \\ e_2 = x_2 - x_2^* \\ e_3 = u - u^* \end{cases} \tag{3.8}$$

The final control law for the Boost converter equation can be represented as:

$$\dot{u} = -K[\frac{dx_1}{du}(x_1 - x_1^*) + \frac{dx_2}{du}(x_2 - x_2^*) + (1)(u - u^*)] \tag{3.9}$$

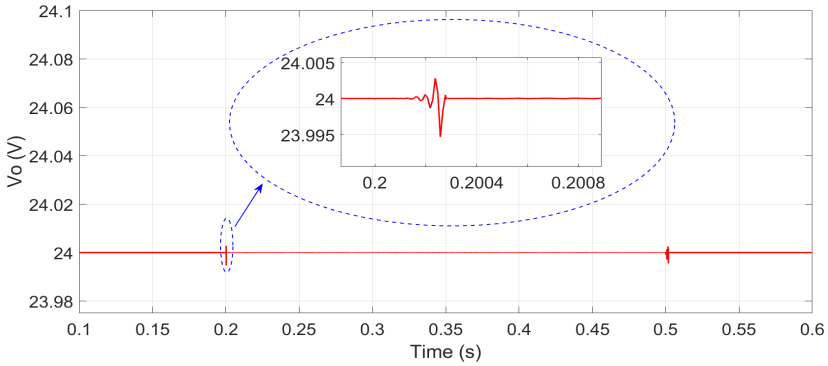

(a) Output voltage V_o

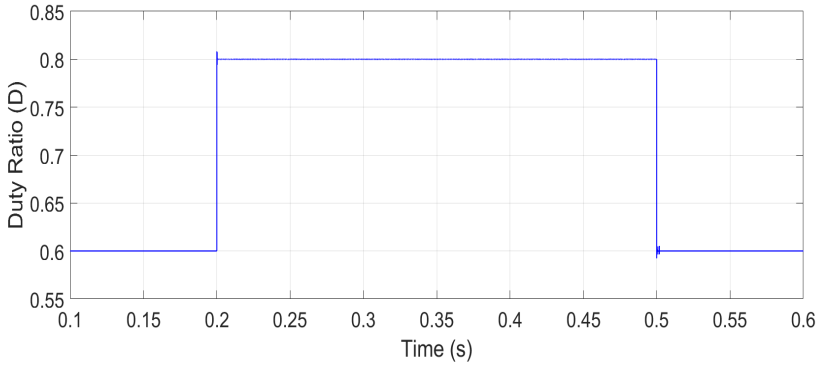

(b) Duty ratio D

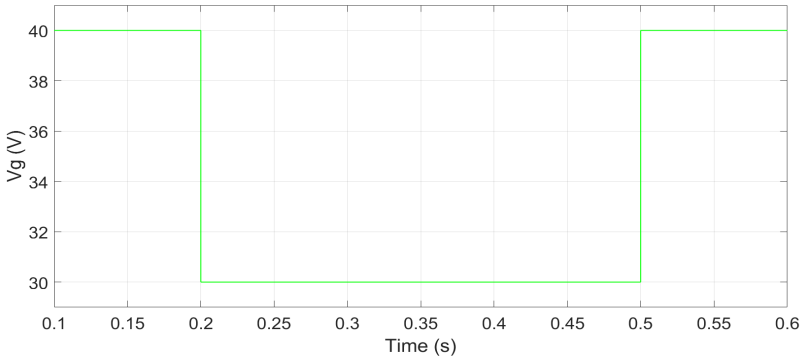

(c) Input voltage V_g

Fig. 3.2 (a) Voltage and (b) Duty ratio response of the Buck converter in face of (c) Input voltage variation from 40 V to 30 V

Table 3.2 Specifications of Boost Converter and Controller Gain

Description of Parameters	Nominal Value
Input Voltage, V_g	12 V
Reference Output Voltage, V_{ro}	24 V
Capacitor, C	32 uF
Inductor, L	94 uH
Resistance, R	12 Ω
Switching frequency, f_s	100 kHz
TCB gain, K	50000

Considering the sensitivity parameters $w_1 = \frac{dx_1}{du}$ and $w_2 = \frac{dx_2}{du}$, the equations for deriving the sensitivity parameters are:

$$\begin{cases} \dot{w}_1 = -\frac{w_2}{L} + \frac{Dw_2}{L} + \frac{x_2}{L} \\ \dot{w}_2 = -\frac{w_1}{C} - \frac{w_2}{RC} - \frac{Dw_1}{C} - \frac{x_1}{C} \end{cases} \tag{3.10}$$

It is important to note that gains here are equal to unity.

3.1.4 Simulation Results for the Boost Converter

The converter and the controller have been simulated in the Simulink environment. Table 3.2 shows the specifications for the converter parameters and controller gain.

The controller for the Boost converter has been designed to maintain stable output voltage and inductor current despite fluctuations in load resistance or input voltage. The following section evaluates the controller performance under these test conditions.

Load resistance variations

To assess the controller, a step change in load resistance from its nominal 12 Ω to 18 Ω was implemented at $t = 0.15$ s, reverting to 12 Ω at $t = 0.3$ s. Fig. 3.3 illustrates the resulting fluctuations in average output capacitor voltage V_o and inductor current I_L. The magnified view in Fig. 3.3(b) reveals that the overshoot peak remains below 25 V (precisely 24.71 V), constituting only 2.95% of the steady-state value at the step change moment. Moreover, this voltage variation exhibits a remarkably brief settling time (2%) of just 245 μs. Fig. 3.3(a) demonstrates that the inductor current is tracked without any noticeable overshoot or time delay.

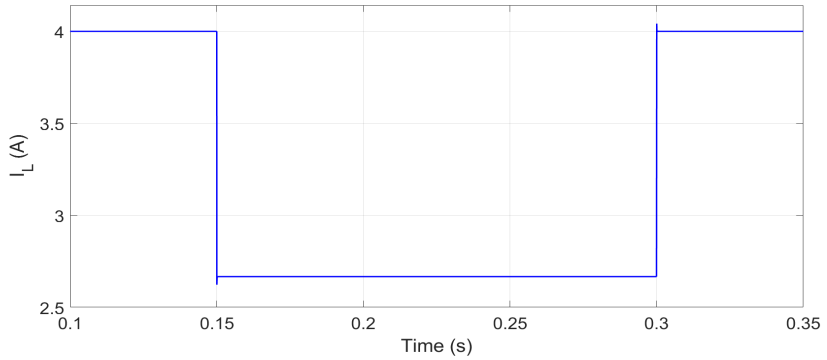

(a) Inductor current I_L

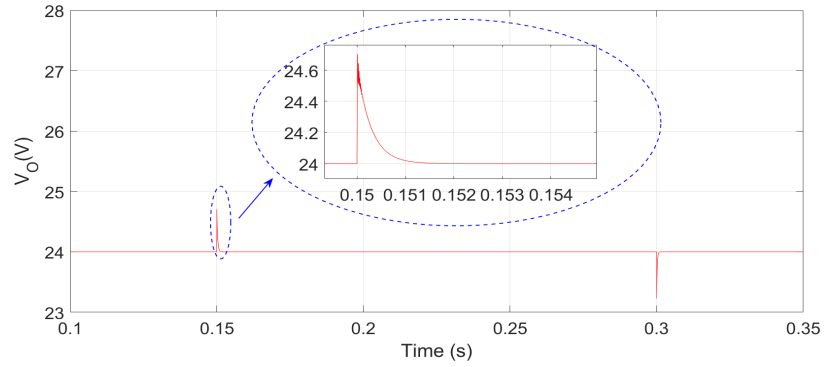

(b) Output voltage V_o

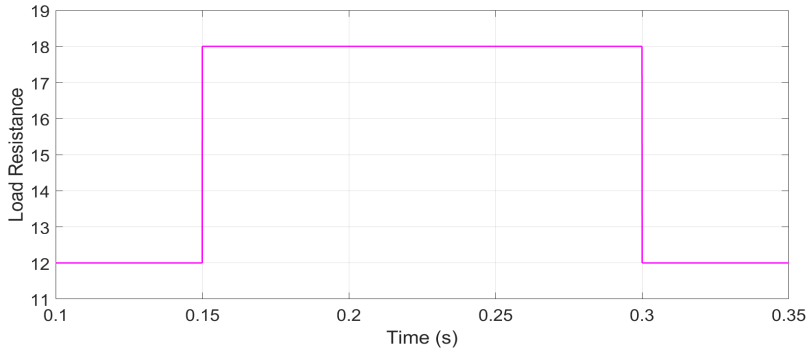

(c) Load resistance R

Fig. 3.3 (a) Inductor current and (b) Output voltage of the Boost converter in face of (c) Load resistance variation from 12 Ω to 18 Ω

Input voltage variations

The converter input voltage was subject to a step increase from $V_g = 12$ V to $V_g = 17$ V at $t = 0.15$ s, returning to its nominal value at $t = 0.3$ s. Fig. 3.4 displays the resulting changes in average inductor current and output capacitor voltage.

The magnified view in Fig. 3.4(b) reveals a voltage peak overshoot of 24.6925 V, with a settling time (2%) of 218 μs. Once again, the inductor current exhibits near-perfect tracking, demonstrating no discernible overshoot or time delays.

3.1.5 Comparison of TCB and Backstepping-based Controllers for Buck and Boost Converters

To underscore the efficacy of our findings, we implemented a backstepping controller for both Buck and Boost converters. This approach has been previously applied to power converters, with its advantages over basic passivity-based controllers noted in [39].

Both controller types were subject to identical test conditions involving load and input voltage variations. The backstepping controller was meticulously tuned for optimal performance.

Fig. 3.6 illustrates the Buck converter's output voltage response to load resistance variations. The TCB-based controller exhibits superior performance with less overshoot (0.30% versus 0.5%) and faster settling time compared to the backstepping controller.

For the Boost converter, simulations were conducted under both load variations (12 Ω to 18 Ω) and input voltage fluctuations (12 V to 17 V). Results are presented in Fig. 3.7. Under variable load conditions, the backstepping controller yields a settling time (2%) of 446 μs versus TCB's 245 μs, and a peak overshoot of 24.95 V (3.96%) compared to TCB's 24.71%.

Similar trends emerge under variable input voltage conditions. The backstepping controller produces an overshoot of 25.08 V (4.5%) with a 399 μs settling time. In contrast, the TCB controller demonstrates superior performance with a 2.88% peak overshoot and 218 μs settling time.

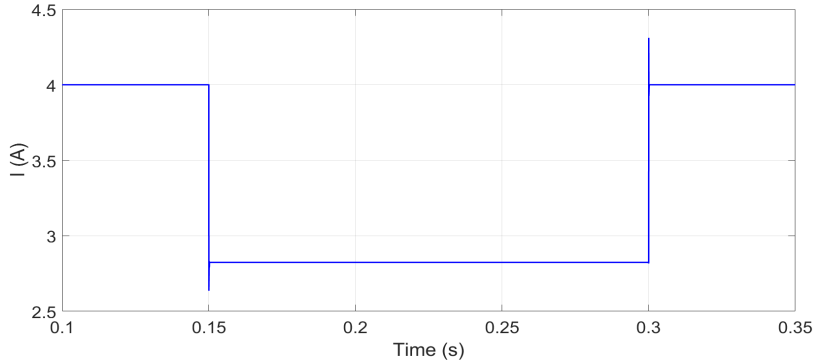

(a) Current I_L

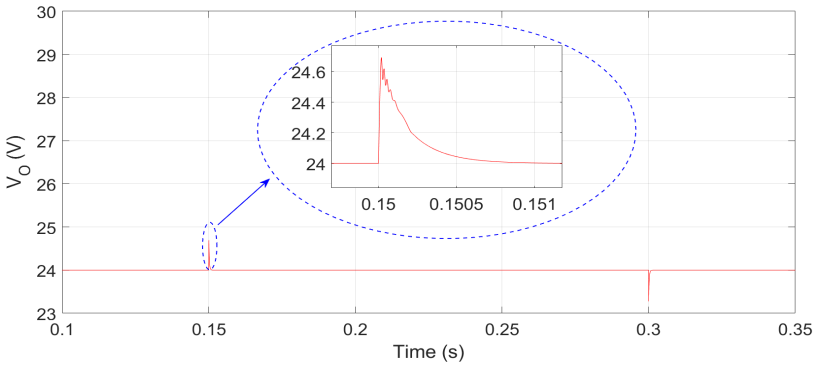

(b) Output voltage V_o

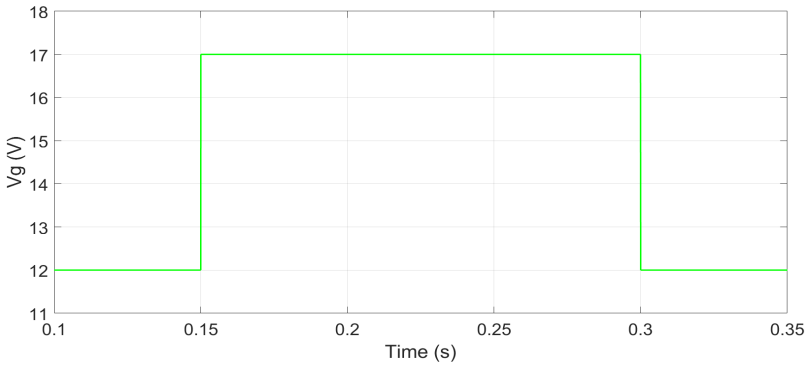

(c) Input voltage variation V_g

Fig. 3.4 (a) Inductor current and (b) Output voltage of the Boost converter in face of (c) Input Voltage Variation from 12 V to 17 V

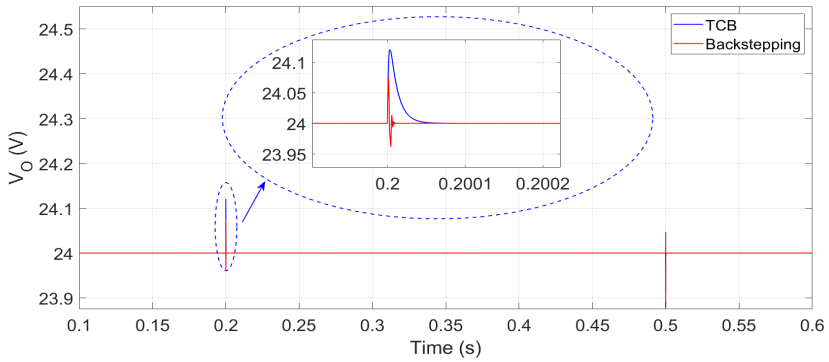

Fig. 3.5 Performance comparison of TCB and backstepping controllers for the Buck converter under step change in load resistance from 12 Ω to 17 Ω

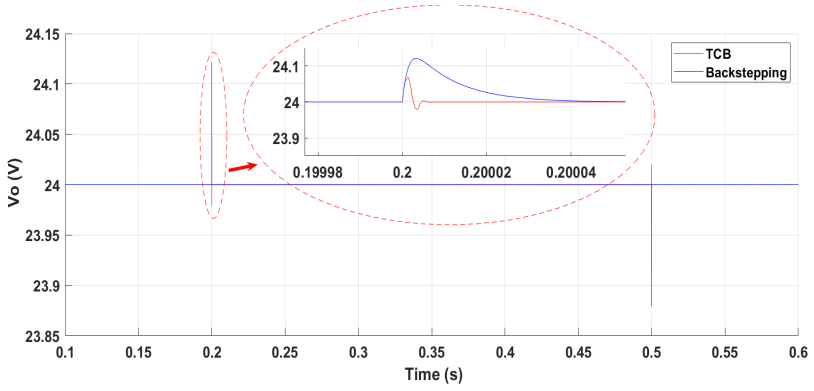

Fig. 3.6 Comparison of TCB and backstepping controllers for Buck converter due to step change in load resistance from 12 Ω to 18 Ω

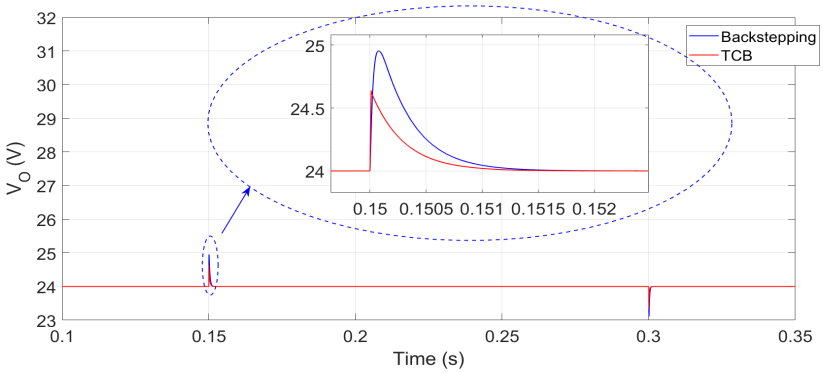

(a) Output voltage V_o under variable load conditions

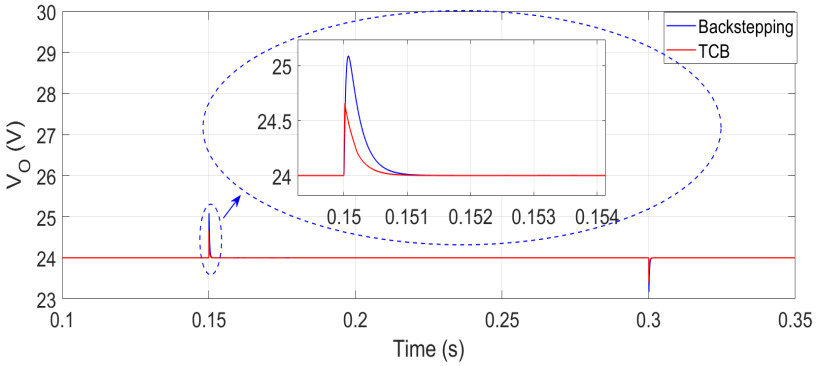

(b) Output voltage V_o under variable input voltage

Fig. 3.7 Comparison of TCB and backstepping controllers for output voltage regulation of the Boost converter under step changes in (a) Load variations and (b) Input voltage variations

3.1.6 Concluding Remarks

This section has introduced an application of model reference adaptive TCB methodology to ideal Buck and Boost converter topologies. The controller's adaptive mechanism integrates the novel TCB approach, ensuring asymptotic convergence of the converter responses to steady-state values despite variations and uncertainties.

Performance evaluation of the controller was conducted under diverse load and input voltage scenarios for both Buck and Boost converters. The controller exhibited exceptional performance across all test conditions for both converter types.

Furthermore, a comparative analysis with a backstepping-based controller was performed, demonstrating the superior efficacy of the TCB controller for both converter topologies. To further validate the proposed approach, in the coming section, we will verify the proposed approach building hardware prototype in the laboratory.

3.2 Application of TCB approach for Maximum Power Point Tracking in PV Array Application

Renewable energy plays a vital role in sustainable technological advancement. Among renewable energy sources, PV systems stand out as one of the most sustainable and rapidly evolving solutions. PV systems are applied in many stand-alone and grid-connected electrical networks, including residential, commercial, industrial, and rural supply applications [40–42].

Additionally, PV generation is utilized in powering infrastructure for Electric Vehicle (EV) charging stations [43, 44]. Furthermore, grid-connected PV plants incorporating batteries for energy storage are employed to stabilize and provide backup power in modern electric networks [45].

Fig. 3.8 illustrates a typical PV system structure, comprising a PV array, DC-DC converter, and controller. To maximize power extraction from the PV array under fluctuating temperature and irradiance conditions, the array must operate at its Maximum Power Point (MPP). The Maximum Power Point Tracking (MPPT) controller's role is to ensure the PV array operates at the MPP by regulating the chopper's duty cycle. This process of maintaining the MPP is known as Maximum

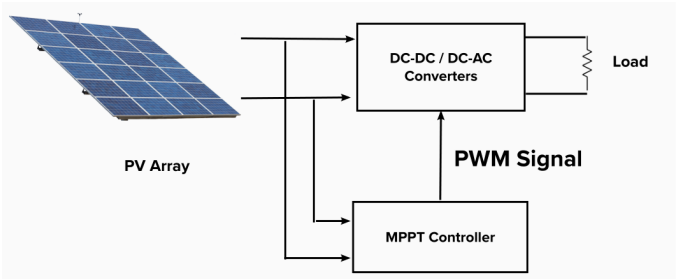

Fig. 3.8 PV system with MPPT control

Power Point Tracking [46]. MPPT for photovoltaic systems is a common application in power electronics. The MPPT controller is crucial to the PV system overall efficiency, as the controller performance directly impacts the entire system efficiency under varying external conditions.

Two different aspects are responsible for the efficiency improvemet of a PV system:

- The layout arrangement and the structure of the PV cells [47].
- The MPPT algorithm used to maximize the energy extracted from the PV source [48].

In literature, different MPPT techniques have been proposed. [49, 50] have presented a comprehensive overview of the MPPT techniques used in literature. The commonly proposed techniques in the literature can be broadly categorized as follows:

- Hill-climbing techniques
- Optimization based algorithms
- Artificial intelligence-based techniques
- Linear and nonlinear techniques

Hill-climbing (HC) methods, including *Perturb and Observe* (P&O) and *Incremental Inductance*, have been well-established in the field for many years. These HC approaches are widely adopted due to their relatively accurate results, straightforward implementation, and minimal sensor requirements.

The P&O method involves calculating the converter's input power, then slightly adjusting the voltage level (ΔV) in one direction by modifying the duty cycle. If this change results in a positive power change (ΔP), the perturbation continues in the same direction; otherwise, it reverses. This process eventually leads to the Maximum Power Point (MPP). However, P&O faces two main challenges that can reduce its efficiency. Firstly, power measurements can only be taken after transients have settled, which slows down convergence. Secondly, while larger perturbations can speed up convergence, they also increase oscillations around the MPP, leading to higher power losses. To address these issues, researchers have developed modified P&O strategies [51]. These new approaches incorporate novel methods to adjust the perturbation value, enhancing convergence speed. For partial shading conditions, various modifications to the conventional P&O algorithm have been proposed. One approach involves an initial duty-cycle tuning across the full feasible range to identify all peaks [52]. Another method divides the exploration range into progressively smaller rectangular areas, selecting the area most likely to contain the Global MPP (GMPP) [53]. While these modifications can improve performance, they often increase convergence time, and in some cases may still miss the GMPP.

Recent research has also explored combining the conventional P&O algorithm with metaheuristic techniques such as particle swarm optimization [54] and ant colony optimization [55]. These hybrid approaches have shown improved results and significantly reduced power oscillations.

Incremental Conductance (IC) is another traditional method discussed in academic literature. It operates by making sure that summing instantaneous conductance (I_{pv}/V_{pv}) and incremental conductance ($\Delta I_{pv}/\Delta V_{pv}$) is equal to zero [56]. Its operation is similar to the Perturb and Observe (P&O) method, where the duty cycle is adjusted to find the Maximum Power Point (MPP). IC performs better than P&O in rapidly changing environmental conditions due to its more accurate tracking and adaptability. However, like P&O, it struggles with balancing perturbation amplitude and power loss from oscillations. IC has comparable efficiency to P&O but demands more complex control systems, leading to higher costs [49]. To enhance IC algorithm performance under partial shading, a modified version in [57] uses a simple linear equation to track the Global Maximum Power Point (GMPP). This modification, however, requires extra measurement circuits, increasing overall costs.

Recently, Artificial Intelligence (AI) has been increasingly used to improve MPPT algorithms and the efficiency of PV systems [58]. Bio-inspired AI optimization techniques, also known as meta-heuristics, have become popular as alternatives to hill-climbing algorithms [59, 60]. These AI-based methods often perform better under partial shading conditions [61]. When a PV array is evenly irradiated, the power-voltage curve shows a single peak that the MPPT controller tracks. Under partial shading, however, the power-voltage curve has multiple peaks, with the highest one being the GMPP and others being Local Maximum Power Points (LMPPs). The controller's challenge is to find the GMPP rather than getting stuck on an LMPP. Hill-climbing techniques, designed to search for peaks without considering the global response, often converge on an LMPP instead of the GMPP [59].

The structure of meta-heuristic algorithms generally follows a similar pattern. Initially, unique particles or individuals are randomly generated within the solution space to form a population. Each particle's position is evaluated against an objective function. Particles then interact to create new offspring, and if an offspring's position is better than its parent's, it is updated. This cycle continues until the process converges to the target point. These algorithms perform better under rapidly changing environmental conditions, offering faster response times and reduced overshoot and fluctuations. They are particularly effective in finding the Global Maximum Power Point (GMPP) under partial shading conditions [60].

However, meta-heuristic algorithms have their drawbacks. Their performance heavily depends on initial conditions and selected parameters. For instance, choosing the right initial population size is crucial for balancing exploration (global search capability) and exploitation (local maxima convergence). A larger population size enhances exploration but hampers exploitation, and vice versa [62]. The optimal population size is specific to the PV characteristic curves, meaning a size that works for one PV system may not be suitable for another.

Some techniques enhance the exploration phase by randomizing or using nonlinearly decreasing initial weight parameters before optimizing exploitation in steady-state conditions [63]. However, this increases computational burden and costs. Parameter selection also significantly impacts the performance of these algorithms.

Other AI-based methods like Fuzzy Logic (FL) and Neural Networks (NN) handle system nonlinearities better than traditional methods. These techniques do not require knowledge of the system's mathematical model. An FL controller has

three components: (i) fuzzification, (ii) decision-making, and (iii) de-fuzzification. Fuzzification uses a membership function to convert numerical input variables into linguistic variables, typically error (e) and change in error (Δe). Decision-making relies on a rule base set by the system designer. De-fuzzification converts linguistic variables back to numerical output, usually the duty cycle of the dc-dc converter. FL-based MPPTs do not need an accurate PV system model, can handle nonlinearities, and work with imprecise inputs [64]. Their main drawbacks are the need to set up fuzzy controller parameters and the complexity of computations.

NN-based controllers, like FL controllers, do not require information about the PV system. Input parameters can include voltages, currents, or environmental factors, with the output typically being the duty cycle. To track the MPP accurately, the NN must establish a precise relationship between inputs and outputs, achieved through extensive training with appropriate datasets [50]. Since each PV array has unique characteristics, NNs must be trained individually for each array and retrained periodically as characteristics change over time. While FL and NN controllers provide accurate, fast responses even in harsh conditions, they are costly, complex to implement, and time-consuming to train [65].

Due to these challenges, linear controllers like Proportional-Integral-Derivative (PID) controllers have been proposed for MPPT. Linear techniques optimize control gains to extract maximum power from PV systems [66]. However, since PV arrays and DC-DC converters are inherently nonlinear, linear controllers require small-signal approximated models to linearize the system around the equilibrium point.

Nonlinear controllers, on the other hand, ensure robustness and stability under various operational conditions [38]. Recent research has focused on nonlinear controllers for PV systems, including back-stepping and sliding mode control (SMC) techniques [67–69, 61]. These controllers are easier to implement digitally and techniques like SMC perform well against system parameter variations or load voltage fluctuations.

Even with nonlinear control approach, there are specific challenges that need to be tackled. One well-known issue is the “chattering” phenomenon, which increases power losses when implementing Sliding Mode Control (SMC) in practical applications. Another challenge for power converters is maintaining a high switching frequency for ideal SMC implementation. However, in practical scenarios, the frequency must be kept constant due to the additional costs of components and filter

design issues. This problem is addressed by using the Pulse Width Modulation (PWM) technique to implement the equivalent control of SMC, which keeps the operating frequency constant. However, operating at a fixed finite frequency results in higher steady-state errors. This issue was first addressed in [70] by introducing an "integral of error" term as a control variable, known as Integral Sliding Mode Control (ISMC), which reduces steady-state errors. Since then, SMC with additional integral action has been used for regulating Čuk and Quasi-Z-source converters [71, 38].

The strategy of using higher order terms has not remain limited to sliding-mode only. [68] uses higher order integral terms to better the results of a backstepping controller implemented in [67] by reducing the steady-state error. The overall issue with this strategy is that it not only requires time derivatives of the variables but also increases the computational burden on the system.

Following the way to implement efficient nonlinear controllers, this part of the research proposes the model-reference adaptive control approach for MPP tracking in a PV system. The reason being that the adaptive control technique can be quite useful for systems that have parameters that can undergo fluctuations. Rationale for the choice is that the adaptive control technique can be quite useful for systems that have parameters that can undergo fluctuations. In the literature, adaptive control techniques have been applied to different engineering fields, such as robotics [72], flight control [73, 74], power system control [75] etc. The control mechanism of the proposed approach is based on the TCB methodology, in which the convergence of the error vectors to the equilibrium point is ensured through the fulfillment of the Lyapunov stability criteria. The TCB methodology has been conceptualized to be used for different mathematical programming problems [76], and has been applied to various problems in the power systems area, to solve the power flow [77], the optimal power flow [78], and the formulation of differential algebraic equations in the analysis of distribution networks [79] or switched capacitor converters [16].

The novel application to the MPPT controller with the proposed TCB-based control approach has been developed for a non-inverted Buck-Boost converter-based system for interfacing a PV source with a DC system.

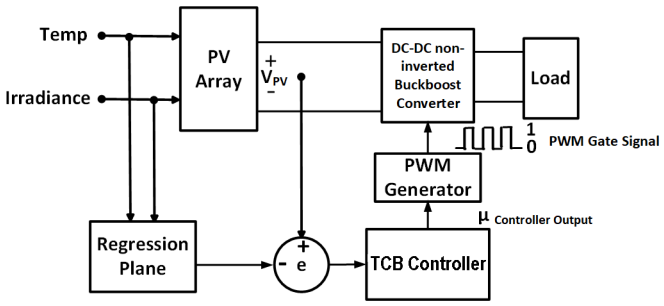

Fig. 3.9 Block diagram of the PV system

3.2.1 Application of the MRAC-TCB Approach for MPPT of PV Arrays

This section explores the MRAC-TCB control approach, which is applied to develop a novel Maximum Power Point Tracking method in a PV system. This system incorporates a Buck-Boost converter to mediate between the PV source and the load. Fig. 3.9 depicts the suggested independent PV system, which includes essential elements such as:

- PV module
- Regression Plane
- Inverted Buck-Boost converter
- MRAC-TCB control unit

Within the PV system, sensors relay the irradiance and temperature data of the PV module to the analytical surface, which then calculates the Maximum Power Point voltage, denoted as V_{MPP}, through a defined mathematical formula. The PV system's error is identified as the variance between the PV module's output voltage and the set reference voltage. This discrepancy serves as the input for the MRAC-TCB control unit, which then produces the control signal u. This signal adjusts the duty cycle of the Buck-Boost converter via a PWM generator. Subsequent subsections will provide additional information on the analytical surface, the mathematical model of the converter, and the formulation of the control unit.

3.2.2 Generation of the Reference Voltage by the Regression Plane

The determination of the Maximum Power Point voltage (V_{MPP}) for any given set of irradiance and temperature conditions in a PV array is facilitated by a regression plane. This process involves formulating a linear mathematical relationship that correlates the irradiance and temperature values with the V_{MPP} computation. The technique for formulating this relationship is outlined in [80, 67]. Initially, a series of MPP curves are produced by altering the temperature from 30°C to 60°C while maintaining a steady irradiance of 1000 W/m^2, and the corresponding data points are documented. Subsequently, the irradiance is varied from 1000 W/m^2 to 600 W/m^2 while keeping the temperature fixed at 25°C, resulting in an additional collection of data points. These data points undergo linear regression analysis to construct a three-dimensional regression plane. This plane enables the extraction of the V_{MPP} value for any irradiance and temperature pairing. Table 3.3 details the specifications of the PV array utilized for data acquisition. The established mathematical relation between the VMPP, irradiance G, and temperature T is presented below:

$$V_{MPP} = c_0 - c_T * T - c_G * G \tag{3.11}$$

where c_0, c_T and c_G are coefficients whose values are determined for each PV array individually.

3.2.3 Mathematical Modeling of the Non-inverted Buck-Boost Converter

Incorporating a DC-DC converter within a PV system is essential, as it forms the connection between the PV panel and the load, facilitating the alignment of the PV panel's operational point with its Maximum Power Point. The selection of a non-inverted Buck-Boost converter is advantageous for MPPT purposes due to its efficiency and suitability among various converter options [81]. The schematic of the converter is represented in Fig. 3.10. This chapter focuses exclusively on the converter's operation in the continuous conduction mode.

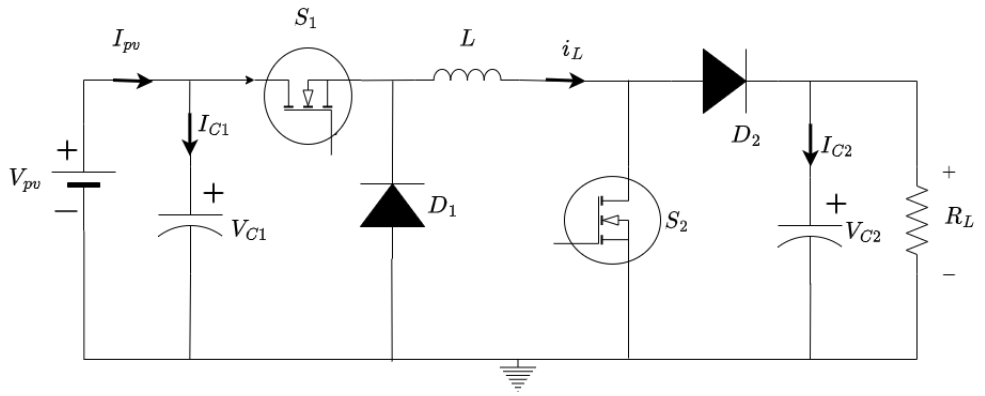

Fig. 3.10 Non-inverted Buck-Boost converter.

Let x_1, x_2 and x_3 be the average values of v_{C1}, i_L and v_{C2}, respectively then using Kirchhoff's voltage and current laws, we can derive the following equations:

$$\begin{cases} x_1 = v_{C1} \\ x_2 = i_L \\ x_3 = v_{C2} \end{cases} \tag{3.12}$$

$$\begin{cases} \dot{x}_1 = \dfrac{i_{PV}}{C_1} - \dfrac{x_2}{C_1}u \\ \dot{x}_2 = \dfrac{x_1}{L}u - \dfrac{x_3}{L}(1-u) \\ \dot{x}_3 = \dfrac{x_2}{C_2}(1-u) - \dfrac{x_3}{RC_2} \end{cases} \tag{3.13}$$

The above state space model is used to track the reference V_{MPP}.

3.2.4 Mathematical Derivation of the MRAC-TCB Approach for the Non-inverted Buck-Boost Converter

The process for implementing the MRAC-TCB controller is similar to the methods described in previous sections. The first step involves deriving a reference signal for the desired trajectory, which is generated using a regression plane. In this specific application, the variable of interest, y_{r0}, is defined as v_{C1}.

The second step is the derivation of the steady-state expressions for all the states of the system. These expressions are found by setting the contents of Equation (3.13) to zero.

$$\begin{cases} x_1^* = y_{r0} \\ u^* = \frac{2a-\sqrt{4a^2-4a(a-y_{r0})}}{2(a-y_{r0})} \\ x_2^* = \frac{y_{r0}u^*}{R(1-u^*)^2} \\ x_3^* = \frac{y_{r0}u^*}{1-u^*} \end{cases} \tag{3.14}$$

where $a = I_{pv}R_1$.

The next step is to define the tracking errors that can be minimized through the adaptation mechanism to accurately track the reference signal, as:

$$\begin{cases} e_{x_1} = \alpha_1(x_1 - x_1^*) \\ e_{x_2} = \alpha_2(x_2 - x_2^*) \\ e_{x_3} = \alpha_3(x_3 - x_3^*) \\ e_u = \beta(u - u^*) \end{cases} \tag{3.15}$$

Here, the weight vector $\mathbf{A} = [\alpha_1,\ \alpha_2,\ \alpha_3,]^T$ and the weight constant β are empirically determined to specify the speed of the control algorithm. Again, using the expression defined in Equation (1.37) and the error vector mentioned above, the control equation becomes:

$$\dot{u} = -K\left[\alpha_1 \frac{dx_1}{du} e_{x_1} + \alpha_2 \frac{dx_2}{du} e_{x_2} + \alpha_3 \frac{dx_3}{du} e_{x_3} + \beta e_u\right] \tag{3.16}$$

where K is the gain factor with a constant value given in Table 3.4. The parameters sensitivity parameters $s_1 = \frac{dx_1}{du}$, $s_2 = \frac{dx_2}{du}$ and $s_3 = \frac{dx_3}{du}$ are calculated based on the original Buck-Boost converter model given in Equation (3.13).

$$\begin{cases} \dot{s_1} = -\frac{1}{C_1}(-x_2 - s_2 u) \\ \dot{s_2} = -\frac{1}{L}(s_1 u + x_3 - s_3(1-u) + x_1) \\ \dot{s_3} = \frac{1}{C_2}\left(s_2(1-u) - x_2 - \frac{s_3}{R}\right) \end{cases} \tag{3.17}$$

Table 3.3 Specifications of PV Array

Description of Parameters	Nominal Value
PV modules per string	10
Parallel strings	1
Maximum Power	213.15 W
Cells per module	72
Voltage at open circuit	363 V
Current at short circuit	7.84 A
Voltage at Maximum Power	290 V
Current at Maximum Power	7.35 A

Table 3.4 Specifications of Buck-Boost Converter and Controller Gains

Description of Parameters	Nominal Value
Capacitance, C_1	67 μF
Capacitance, C_2	480 μF
Inductance, L	11 mH
Resistance, R	20 Ω
Switching frequency, f_s	100 kHz
TCB gain, K	10^4

3.2.5 Simulation Results for the Buck-Boost Converter

To evaluate the performance of the MRAC-TCB controller, both fluctuating and step-wise changes in the irradiance levels of the environment were applied, and simulations were done in Matlab/Simulink. The irradiance can be collected at high speeds, such as every second or even faster [82]. Hence, the testing involved step irradiance changes with very large magnitudes as a cautious scenario. Specifically, the irradiance values were maintained in a realistic range, but the controller was exposed to large changes in very short time intervals, to create more challenging conditions for the control system than the actual ones where the related quantities would vary more gradually. The next subsection shows the results. Regarding temperature changes, these changes happen at a lower speed [83], so the sub-second time span of observation did not include any testing for temperature changes.

In the specifications for the PV array and Buck-Boost converter mentioned in Table 3.3 and Table 3.4, respectively, the empirically determined values of weight vector is $\mathbf{A}$ is [3,1,1] and the weight β is equal to 5.

The numerical values of the coefficients of the regression plane for this PV array system are c_0 = 322, c_T = 1.34, and c_G = 0.00964.

Test under conditions of variable irradiance

The controller was evaluated under varying irradiance conditions. Initially, the irradiance fluctuated while maintaining a constant temperature of 25°C, as depicted in Fig. 3.11. These fluctuations were centered around 1000 W/m², ranging from 900 to 1140 W/m². In a subsequent test, shown in Fig. 3.12, the range of irradiance variation was significantly increased to assess the controller's stability and sensitivity to large changes. Additionally, the irradiance was altered in a step-wise manner to apply maximum stress to the controller. Starting at 1000 W/m², the irradiance was reduced to 800 W/m² at 0.05 seconds and further decreased to 600 W/m² at 0.15 seconds.

Figures 3.13 and 3.14 respectively illustrate the tracking of reference voltage under fluctuating and step-wise variable irradiance conditions respectively. The key observation is that the controller is able to track the reference value generated by the regression plane, ensuring no steady-state error. It is also successful in responding to sudden changes in reference voltage due to fluctuations in Fig. 3.13 and handles big step-wise irradiance changes at 0.05 seconds and 1 second with minimal rise and settling times. Fig. 3.15 demonstrates both the maximum power point tracking and the output power generated by the proposed MRAC-TCB controller under step change variable irradiance conditions. The PV array's power output is delivered to the load with an MPPT efficiency exceeding 95%.

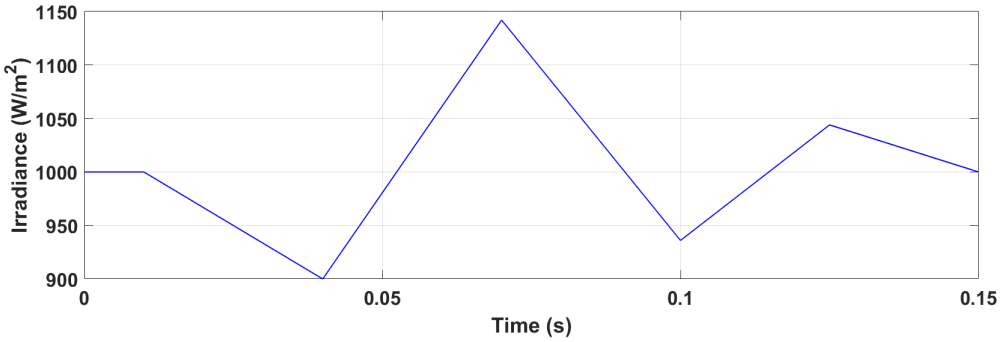

Fig. 3.11 Test with fluctuating irradiance in time.

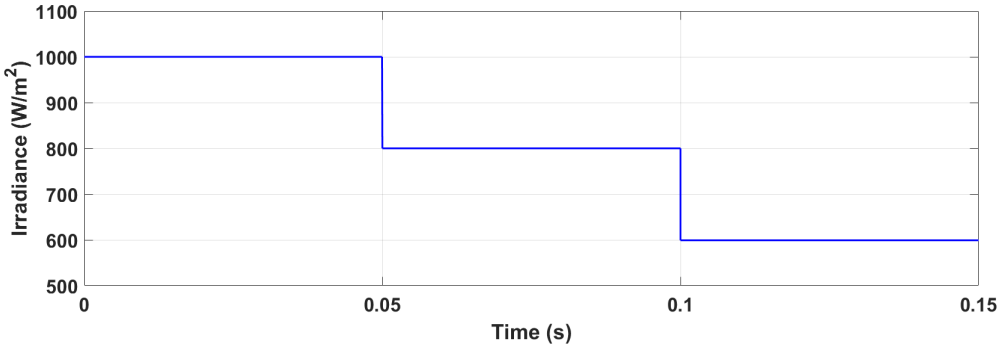

Fig. 3.12 Test with step-wise variable irradiance in time.

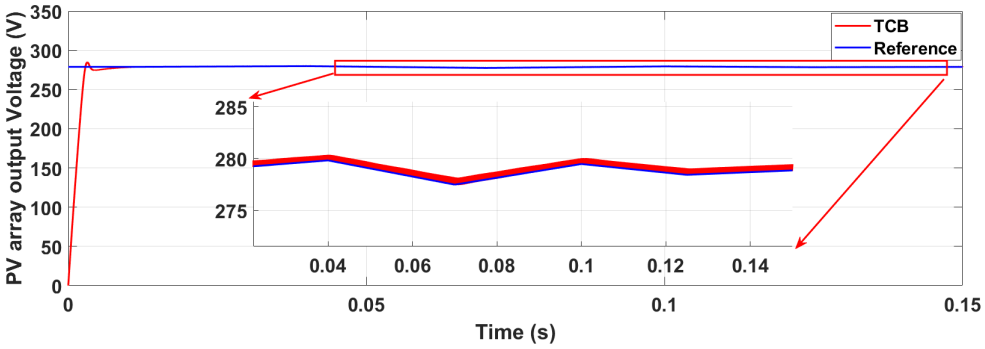

Fig. 3.13 Tracking the MPP voltage under fluctuating irradiance.

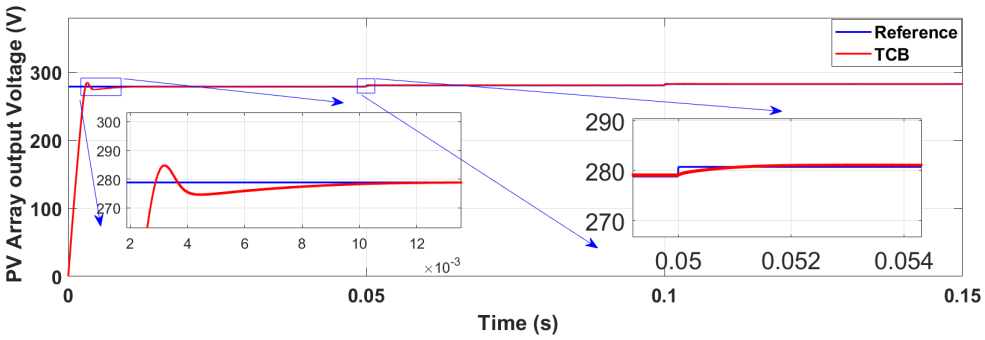

Fig. 3.14 Tracking the MPP voltage under step-wise variable irradiance.

3.2.6 Comparison with Perturb and Observe and Integral Backstepping Controllers

In nonlinear controller literature, one of the most effective outcomes was reported by [68] for an MPPT mechanism utilizing a Non-inverted Buck-Boost system. Con-

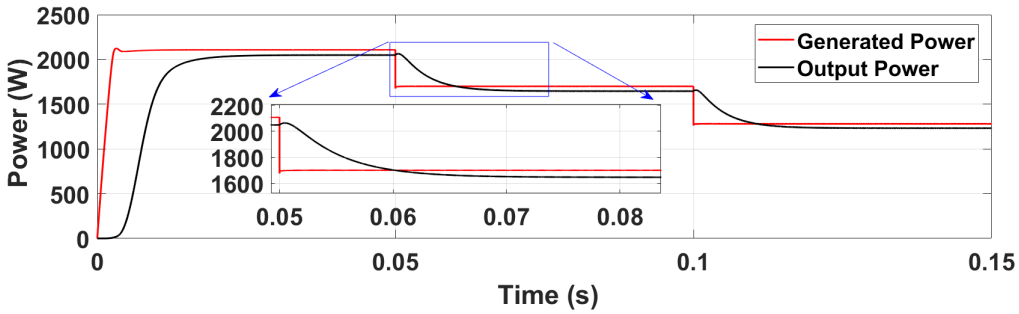

Fig. 3.15 Power output of the PV Array under step-wise variable irradiance.

sequently, for the sake of comparison, the Integral Back-Stepping (IBS) controller suggested in [68] was reproduced, and its performance was juxtaposed with that of the proposed controller. Additionally, a rudimentary P&O controller was meticulously adjusted for the PV system under scrutiny. Fig. 3.16 displays the voltage reference tracking of the trio of controllers under step-wise altering irradiance conditions. The illustration reveals that both the MRAC-TCB and IBS controllers exhibit no steady-state discrepancies, although the IBS controller demonstrates a minor voltage surge.

Table 3.5 offers a comparative analysis of these controllers' reactions. The IBS controller manifests a modest voltage excess of approximately 13 V and a settling duration (2%) of 2.7 ms, whereas the MRAC-TCB controller can be calibrated to virtually eliminate voltage overshoot and achieve a settling period (2%) of 3.1 ms. Post-disturbances, as depicted in Fig. 3.16, the TCB controller's response stabilizes considerably faster than the IBS controller's. Moreover, after the disturbances, the MRAC-TCB controller also boasts a rise time of merely 54.75 µs, in contrast to the IBS controller's 2.17 ms. It is noteworthy that the performance of both Lyapunov-based controllers is commendable, yet the MRAC-TCB controller accomplishes this without the necessity for additional knowledge of the variables' time derivatives.

In a similar vein, Fig. 3.17 demonstrates that after numerous calibration efforts, the P&O controller is capable of aligning with the MPPT point, albeit it experiences multiple oscillations prior to attaining a steady state. It is important to recognize that while the P&O controller is the most straightforward to implement, due to its independence of the regression plane and hence the extra sensors, the overall superiority in the performance of the Lyapunov based controllers is evident. Notably,

the settling time (2%) of P&O cannot be determined because the output voltage value does not reach 2% of the steady-state value.

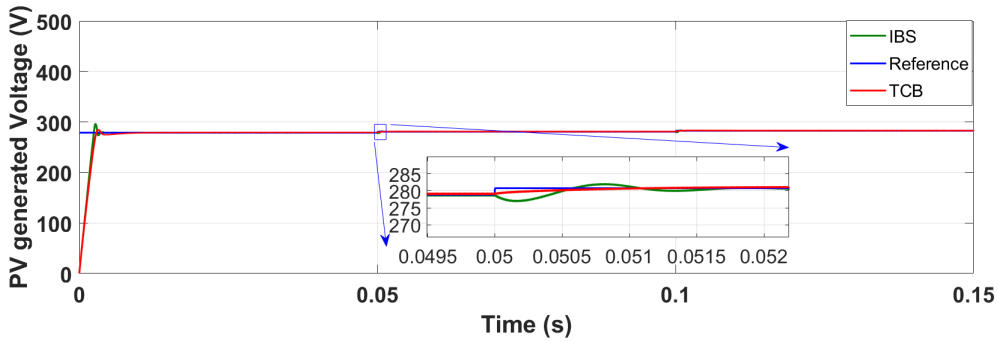

Fig. 3.16 PV array MPP voltage tracking comparison with the IBS controller under variable irradiance.

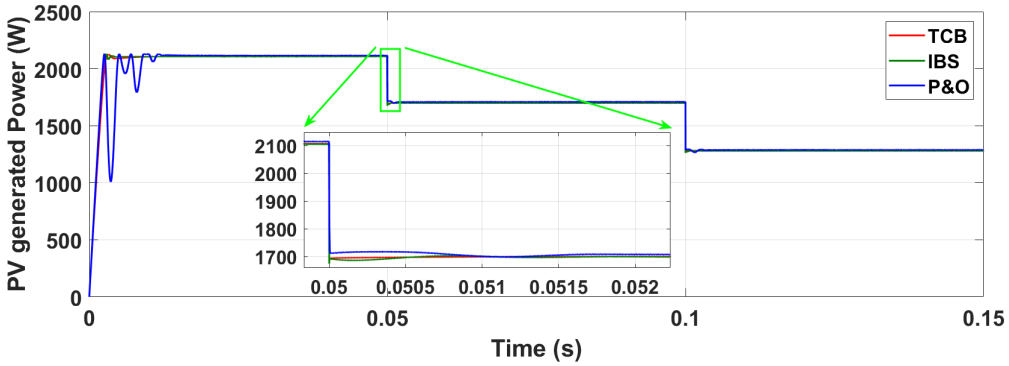

Fig. 3.17 PV array MPPT comparison with the IBS and P&O controllers under variable irradiance.

3.2.7 Concluding Remarks

This section introduced a model reference adaptive controller utilizing the TCB approach to manage an inverted Buck-Boost converter. Implementing this controller facilitates optimal power point tracking for photovoltaic systems. This study marks the first application of the MRAC-TCB controller to an inverted Buck-Boost converter, demonstrating its considerable robustness across various test conditions and establishing global asymptotic stability as per Lyapunov's stability theorem.

Simulations of the photovoltaic system were executed on the Matlab/Simulink environment. A regression plane was utilized to ascertain the maximum power

Table 3.5 Comparison between controllers

Method	RT (ms)	ST 5% (ms)	ST 2% (ms)	Overshoot (V)	MPPT efficiency
P&O	2.3	58.2	NA	86.0	94.8
IBS	2.1	2.8	2.7	13.3	97.4
MRAC-TCB	2.3	2.5	3.0	6.3	96.8

voltage, serving as the benchmark for the MRAC-TCB controller. The tests involved variable irradiance with large and abrupt shifts at high rates, surpassing the severity of changes typically encountered in empirical settings. Notwithstanding these rigorous simulation scenarios, the MRAC-TCB controller maintained an exceptionally robust performance. Additionally, the trials that considered the oscillating irradiance over time showed the controller's suitability in regulating the output voltage in response to fluctuating environmental conditions.

Further comparative analyses with the Lyapunov-based Integral Back-stepping controller and the Perturb and Observe controller, focusing on metrics such as settling time, voltage overshoot, and MPPT efficiency, reveal that the MRAC-TCB controller outperforms the P&O and is on par with the Integral Back-stepping controller, particularly in achieving a markedly reduced voltage overshoot.

3.3 Application of the TCB Control Law on Practical Non-Ideal Buck and Boost Converter Circuits

Following the implementation of the TCB control law for ideal Buck and Boost converters, the next goal was to verify our controller results through hardware testing. To achieve this, we decided to apply the TCB control law to non-ideal Buck and Boost converters. In this context, non-ideal modeling involves considering inductor, capacitor, and switching losses to develop a more accurate mathematical model of the system.

In existing literature, various controllers have been designed for regulating DC-DC converter topologies. However, most of these designs do not account for the parasitic resistances of inductors, capacitors, or switches. Although the values of these parasitic elements are relatively small, they are crucial for the regulation of

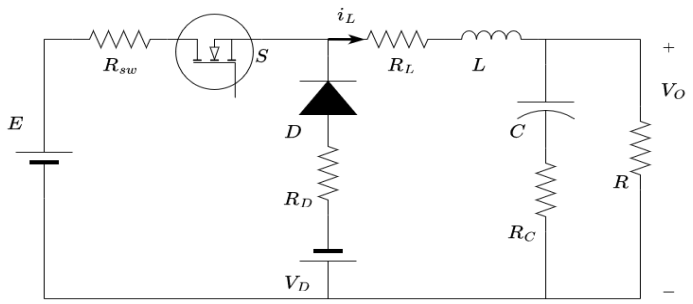

(a) Buck converter

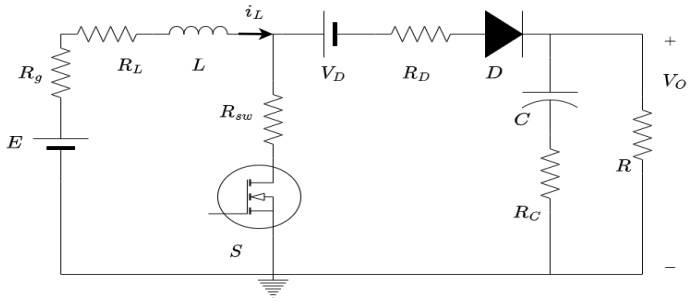

(b) Boost converter

Fig. 3.18 DC-DC converter models with parasitic parameters: (a) Buck converter; (b) Boost converter

practical converters, as ignoring them can lead to model uncertainties [84]. Therefore, incorporating the parasitic elements of the converters into the controller design is a significant contribution of this research.

3.3.1 Steady State Modelling of Buck and Boost Converters with Parasitic Parameters

Fig. 3.18 shows the Buck and Boost circuits with parasitic elements. The large-signal dynamic model for the Buck and Boost converters, taking inductor, capacitor and switching nonlinearities into account, can be derived using the volt-second and charge-second balance.

In the notation used, E, x_1, x_2 and u represent the input voltage, inductor current, capacitor voltage and duty ratio, respectively. The non-ideal parameters R_{sw}, R_L, R_D, R_C and V_D are the switch resistance, inductor resistance, diode resistance, capacitor resistance and diode forward voltage drop, respectively.

The Buck converter model is formulated as:

$$\begin{cases} \dot{x}_1 = \dfrac{-1}{L}\Big[((R_{sw}-R_D)u+R_D+R_L)x_1+x_2-u(E+V_D)+V_D\Big] \\ \dot{x}_2 = \dfrac{x_1}{C}-\dfrac{x_2}{RC} \end{cases} \tag{3.18}$$

The Boost converter model is formulated as:

$$\begin{cases} \dot{x}_1 = \dfrac{1}{L}\Big[-x_1(R_g+R_L)-x_1(1-u)\Big(R_D+\dfrac{RR_C}{R+R_C}\Big)+E \\ \qquad -x_2(1-u)\dfrac{R}{R+R_C}-x_1R_{sw}u-V_D(1-u)\Big] \\ \dot{x}_2 = (1-u)\dfrac{x_1}{C}-\dfrac{x_2}{RC} \end{cases} \tag{3.19}$$

3.3.2 Application of the MRAC-TCB Control Approach to the Buck Converter

Again as mentioned before, TCB approach consists of three steps. In the first step, we need to generate our desired signal that can be used for the regulation of the converter. We can generate this graphically in Matlab and give it as an input directly to the system. The system output y_{r0} is defined as the output voltage V_o. The vector of the state variable is $\mathbf{x} = \{ x_1, x_2\}$, the control variable vector is $\mathbf{u} = \{\mathrm{u}\}$, and the algebraic variable is $\mathbf{y} = \{y_{r0}\}$.

The second step is the derivation of the equilibrium point in the composite domain ($\mathbf{x}$, $\mathbf{u}$), denoted as ($\mathbf{x}$*, $\mathbf{u}$*). For this purpose, the equilibrium point for the steady state values is derived by setting the contents of Equation (3.18) to zero, obtaining:

$$\begin{cases} x_1^* = \frac{y_{r0}}{R} \\ x_2^* = y_{r0} \\ u^* = \frac{RV_D+y_{r0}(R+R_L+R_D)}{RV_D+y_{r0}(R_D-R_{sw})+RE} \end{cases} \tag{3.20}$$

The final step is the derivation of an adaptation mechanism that is capable of minimizing the following tracking errors:

$$\begin{cases} e_{x_1} = w_{x_1}(x_1 - x_1^*) \\ e_{x_2} = w_{x_2}(x_2 - x_2^*) \\ e_u = w_u(u - u^*) \end{cases} \tag{3.21}$$

Based on Equation (1.37) and the error vectors defined above, the expression for the control equation becomes:

$$\dot{u} = -K\left[\frac{dx_1}{du} w_{x_1}^2 (x_1 - x_1^*) + \frac{dx_2}{du} w_{x_2}^2 (x_2 - x_2^*) + w_u^2 (u - u^*)\right] \tag{3.22}$$

where K is the gain factor, with constant value, and w_{x_1}, w_{x_2} and w_u are weights defined on the variations of the state and control variables, respectively, with respect to the equilibrium point.

The sensitivity parameters $s_1 = \frac{dx_1}{du}$ and $s_2 = \frac{dx_2}{du}$ are calculated based on the Buck converter model given in Equation (3.18):

$$\begin{cases} \dot{s}_1 = -\dfrac{1}{L}\Big[(s_1(uR_{sw} - uR_D + R_D + R_L) + s_2 + x_1(R_{sw} - R_D) - E - V_D\Big] \\ \dot{s}_2 = \dfrac{1}{C}\Big(s_1 - \dfrac{s_2}{R}\Big) \end{cases} \tag{3.23}$$

3.3.3 Simulation Results for the Buck Converter

The simulation of the proposed controller has been done in the Matlab/Simulink environment. The parameters of the converter are specified in Table 3.6 along with the used control parameters. The validity of the proposed control has been tested by considering three tests, with:

(i) Tracking of reference voltage,

(ii) Regulation of output voltage under varying load, and

(iii) Output voltage regulation under input voltage variations.

The weights of the error terms in Equation (3.21) are set as $w_{x_1} = 1$, $w_{x_2} = 2$, and $w_u = 3.0$. The results corresponding to the three tests are shown below.

Table 3.6 Specifications of Buck Converter Parameters and Controller Gain

Description of parameters	Nominal value
Input voltage, E	12 V
Reference output voltage, V_o	5 V
Capacitance, C	10 uF
Inductance, L	1 mH
Load resistance, R	47 Ω
Switching frequency, f_s	62 kHz
Inductor resistance, R_L	0.15 Ω
Diode resistance, R_D	0.001 Ω
Switch resistance, R_{sw}	0.1 Ω
Diode forward voltage drop, V_D	0.4 V
TCB gain, K	10^4

Reference voltage tracking

As previously stated, the MRAC-TCB controller's primary objective is to directly track the reference voltage. The first objective of the controller is to follow the reference trajectory for the Buck converter's output voltage. The reference is designed in Matlab using a signal builder. The outcomes are displayed in Fig. 3.19. The generated reference signal makes sure that the nominal voltage is reached within one millisecond, with an overshoot of only 5.3 V (less than 6% of the nominal value). At t = 0.3 s, the reference voltage rises to 7 V, showing a settling time of (2%) of 65.5 ms and a rise time of 20ms. As shown in the zoomed in view of Fig. 3.19(a) around t = 0.3 s, the controller is able to track the reference with zero steady-state error. Following this, reference signal is returned to 5 V output voltage with minimal overshoot and settling time. Here once again, the output voltage is able to track the reference. The changes in inductor current can be seen in Fig. Fig. 3.19(b).

Load resistance variations

The controller's second evaluation involves regulating its output voltage when faced with a sudden change in the specified load. For this test, the reference output voltage is set at 5 V. As indicated in Table 1, the Buck converter's nominal load resistance is 47 Ω. However, at t = 0.3 s, the load resistance increases to 65 Ω, and at t = 0.6 s, it reverts to its initial value. Fig. 3.20 demonstrates the impact of these load resistance fluctuations on the inductor current and output voltage. The figure reveals insignificant steady-state error in both the inductor current and output voltage. Additionally, the maximum voltage overshoot is less than 2.67%, with a settling time (2%) of merely 470 μs.

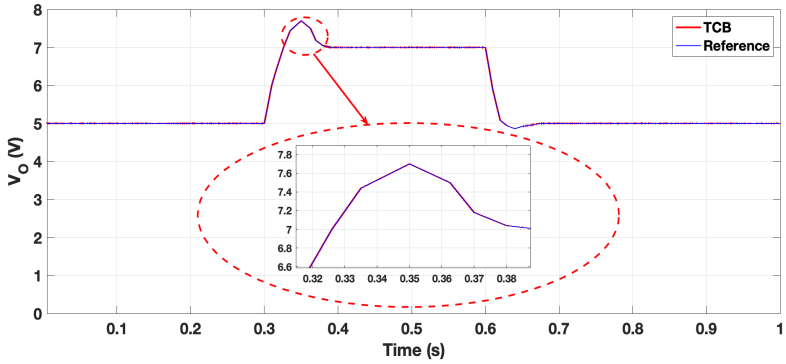

(a) Output voltage

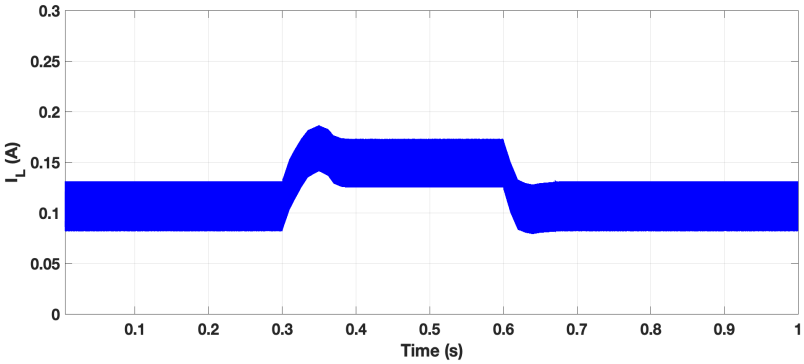

(b) Inductor current

Fig. 3.19 Output voltage and inductor current responses to the reference voltage tracking test for the Buck converter.

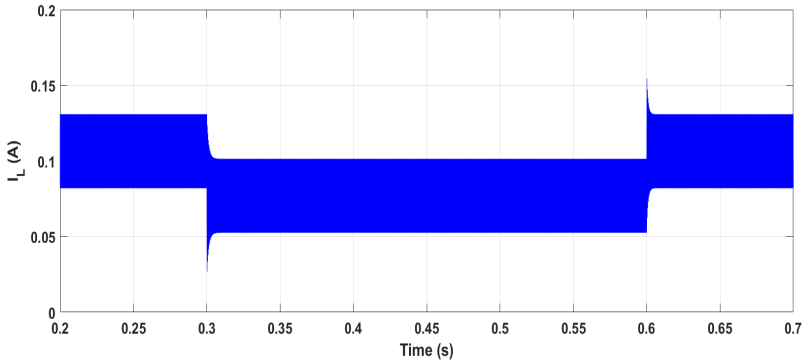

(a) Inductor current I_L

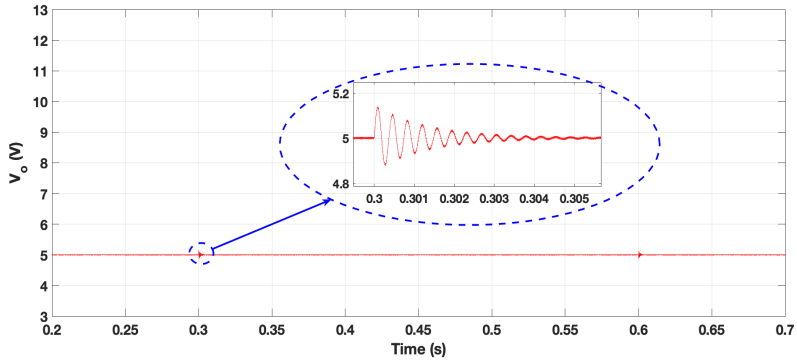

(b) Output voltage V_o

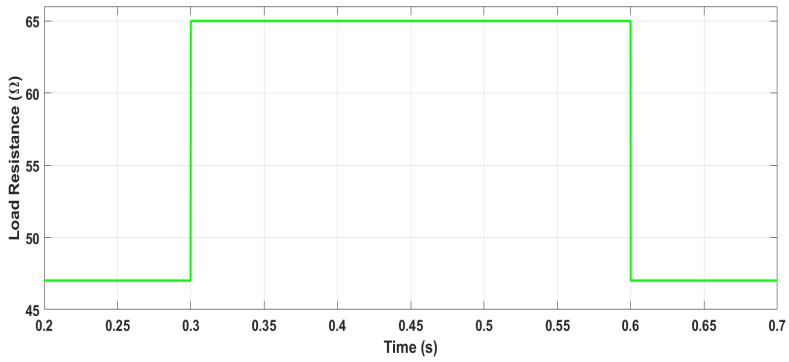

(c) Load resistance R

Fig. 3.20 Inductor current and output voltage responses to a load resistance variation from 47 Ω to 65 Ω in a given time interval for a Buck converter.

Input voltage variations

The designed controller's third test examines its response to input voltage fluctuations. The input voltage is increased from its nominal value of 12 V to 14 V. The consequent changes in output voltage and duty ratio are illustrated in Fig. 3.21 (a) and (b), respectively. In this assessment, the voltage overshoot and settling time are notably minimal, almost to the point of being negligible.

3.3.4 Application of the TCB Control Approach to the Boost Converter

The process for developing the MRAC-TCB control equations for the Boost converter mirrors the approach used for the Buck converter in the preceding section. Equation (3.19) presents the dynamic non-ideal model of the Boost converter. A reference signal is defined and directly input into the simulation. The output voltage V_o is designated as the desired output y_{r0}. To determine the reference values at steady state, Equation (3.19) is set to zero. The reference values used are identical to those utilized in [85]:

$$\begin{cases} x_1^* = \frac{y_{r0}}{R(1-u^*)} \\ x_2^* = y_{r0} \\ u^* = \frac{E}{Vo}\dfrac{1+\frac{y_{r0}}{E}\left(\frac{Rsw-R_D-R||R_C}{R}\right)+\sqrt{\left(1+\frac{y_{r0}}{E}\left(\frac{Rsw-R_D-R||R_C}{R}\right)\right)^2-4\left(\frac{y_{r0}}{E}\right)^2\left(\frac{R}{R+R_C}+\frac{V_D}{y_{r0}}\right)\left(\frac{R_g+R_L+R_{sw}}{R}\right)}}{2\left(\frac{R}{R+R_C}+\frac{V_D}{y_{r0}}\right)} \end{cases} \tag{3.24}$$

The errors to be minimized using the adaptation mechanism are defined as:

$$\begin{cases} e_{x_1} = w_{x_1}(x_1 - x_1^*) \\ e_{x_2} = w_{x_2}(x_2 - x_2^*) \\ e_u = w_u(u - u^*) \end{cases} \tag{3.25}$$

The control equation for the Boost converter is also the same as the one used for the Buck converter, based on Equation (1.37):

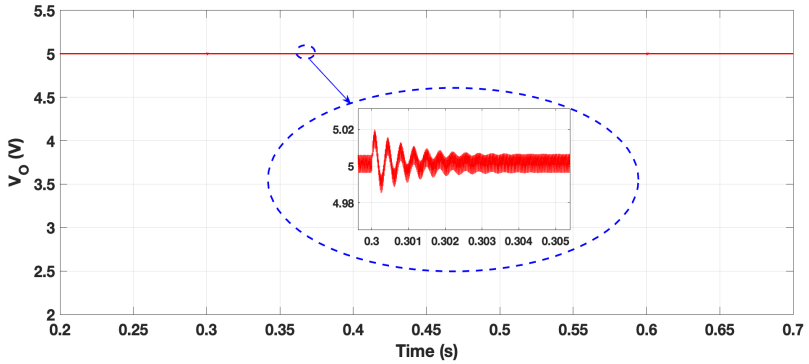

(a) Output voltage V_o

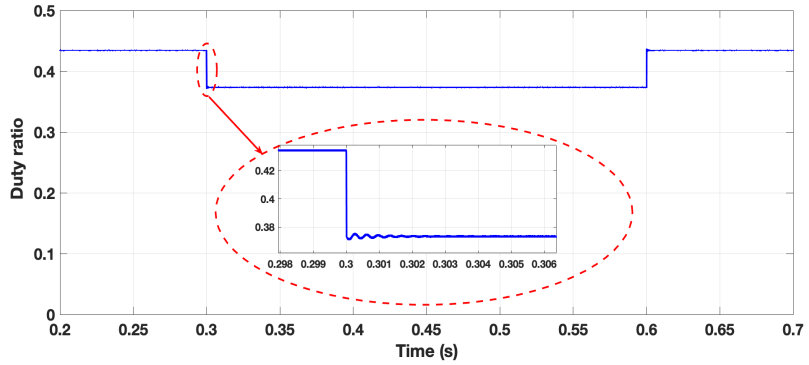

(b) Duty ratio u (control variable)

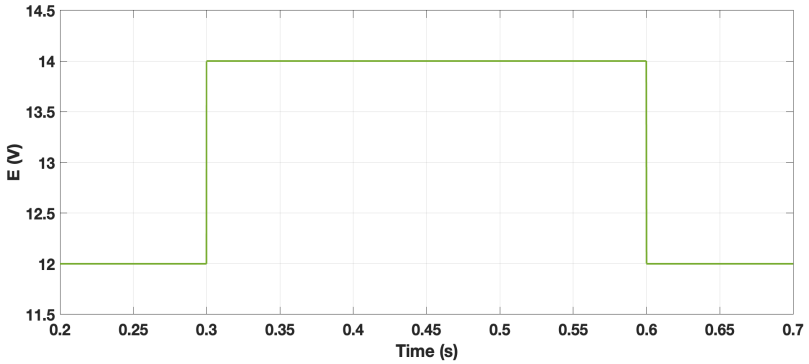

(c) Input Voltage Variation E

Fig. 3.21 Output voltage and duty ratio responses to an input voltage variation from 12 V to 14 V in a given time interval for a Buck converter.

$$\dot{u} = -K\left[\frac{dx_1}{du}w_{x_1}^2(x_1 - x_1^*) + \frac{dx_2}{du}w_{x_2}^2(x_2 - x_2^*) + w_u^2(u - u^*)\right] \tag{3.26}$$

where K is a constant positive gain factor and the weights are calculated empirically.

The sensitivity parameters $s_1 = \frac{dx_1}{du}$ and $s_2 = \frac{dx_2}{du}$ are calculated based on the original Boost converter model given in equation (3.19). The equations for deriving the sensitivity parameters are:

$$\begin{cases} \dot{s}_1 = -\dfrac{s_1}{L}(R_g + R_L + uR_{sw} + a(1-u)) - \dfrac{s_2}{L}((1-u)\dfrac{R}{R+R_C}) - \dfrac{x_1}{L}(-a + R_{sw}) \\ \qquad + \dfrac{V_D}{L} + \dfrac{Rx_2}{L(R+R_C)} \\ \dot{s}_2 = -\frac{s_1}{C} - \frac{s_2}{RC} \end{cases} \tag{3.27}$$

where $a = \frac{RR_C}{R+R_C} + R_D$.

3.3.5 Simulation Results for the Boost Converter

The simulations for the Boost converter were coded and executed in Matlab/Simulink. The specifications for the Boost converter and the controller gains K are indicated in Table 3.7. The weights used for the error terms in Equation (3.25) are empirically set to $w_{x_1} = 1$, $w_{x_2} = 1$, and $w_u = 3.5$, to compensate for the differences in the corresponding quantities.

The performance of the proposed controller has been tested by considering three tests, with:

(i) reference voltage tracking,

(ii) output voltage regulation under varying load, and

(iii) output voltage regulation under input voltage variations.

The results corresponding to the three tests are shown below.

Table 3.7 Specifications of Boost Converter Parameters and Controller Gain

Description of Parameters	Nominal Value
Input voltage, E	12 V
Reference output voltage, V_o	16 V
Capacitance, C	470 μF
Inductance, L	270 μH
Load resistance, R	65 Ω
Switching frequency, f_s	62 kHz
Inductor resistance, R_L	0.125 Ω
Switch resistance, R_{sw}	0.08 Ω
Input resistance, R_g	0.2 Ω
Diode forward voltage drop, V_D	0.3 V
TCB gain, K	10^3

Reference voltage tracking

The Boost converter employs a reference similar to that of the Buck converter. For reference tracking, the Boost converter's nominal voltage is set at 16 V. At $t = 3$ s, this voltage increases to 19 V, then returns to 16 V at $t = 0.6$ s. The reference is designed to achieve steady state within an initial timeframe of 1.875 ms. When t reaches 3 s, the voltage rises to 19 V. Fig. 3.22(a) demonstrates that the reference is tracked with minimal steady state error, achieving a settling time (2%) of 12 ms and a maximum overshoot of 20.04 V. The changes in inductor current are depicted in Fig. 3.22(b).

Load resistance variations

The second test's objective is to sustain a steady output voltage while subjecting the Boost converter to load resistance variations. As indicated in Table 3.7, the nominal load value is 65 Ω. This load value is altered to 80 Ω at $t = 0.3$ s and reverts to its original value at $t = 0.6$ s. The outcomes of this test are illustrated in Fig. 3.23.

Fig. 3.23 shows that the steady state error is insignificant both before and after the load resistance increase. Voltage fluctuations are minimal. Fig. 3.23(a) allows for the calculation of the current's rise time and settling time (2%), which are 3305 μs and 298 μs, respectively.

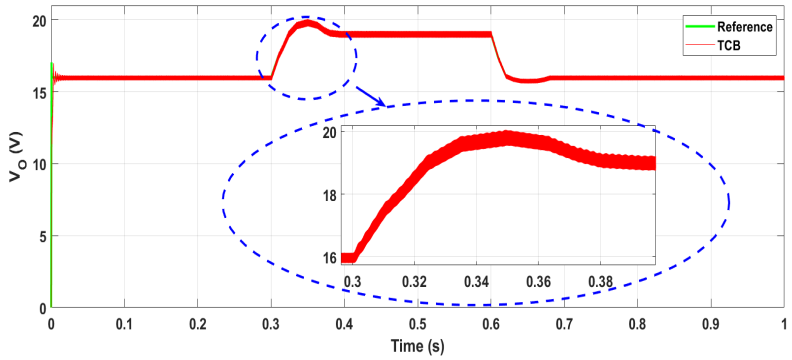

(a) Output voltage

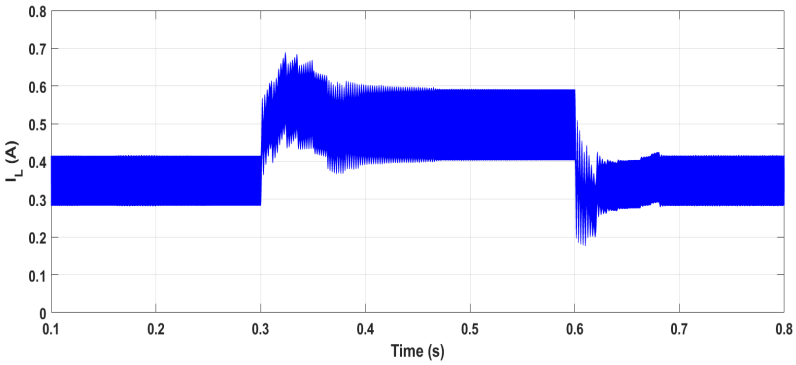

(b) Inductor current

Fig. 3.22 Output voltage tracking for the Boost converter.

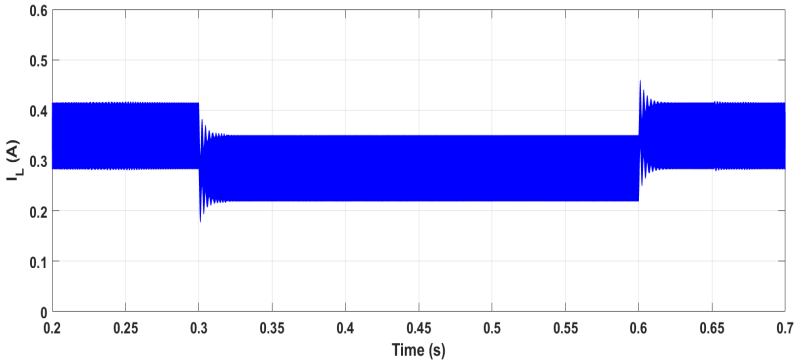

(a) Inductor current I_L

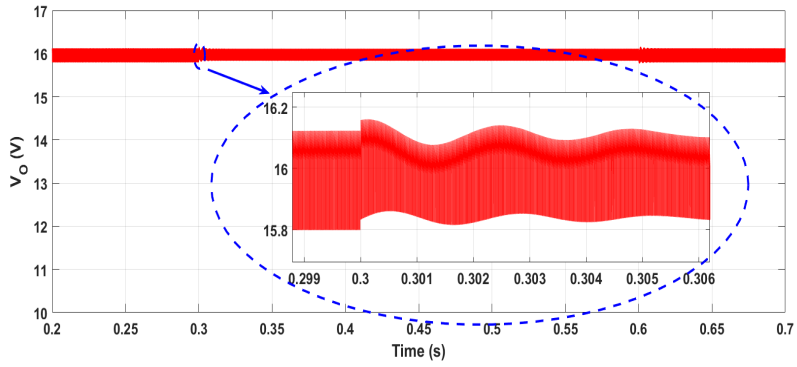

(b) Output voltage V_o

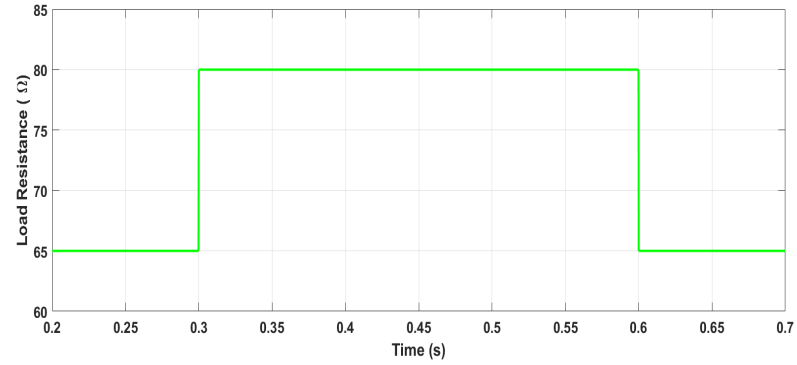

(c) Load resistance R

Fig. 3.23 Inductor current (a) and output voltage response (b) corresponding to the load resistance variation (c) from 65 Ω to 80 Ω in a given time interval for the Boost converter.

Input voltage variations

This test aims to maintain a constant output voltage from the Boost converter while introducing variations in the input voltage. The input voltage, nominally 12 V, is increased to 14 V at $t = 0.3$ s, then returns to its original value at $t = 0.6$ s. Fig. 3.24 displays the results of this test.

An examination of Fig. 3.24 reveals no steady state error either before or after the input voltage increase. The significant voltage fluctuations observed are attributable to the inclusion of non-idealities in the Boost converter model. Fig. 3.24(a) allows for the calculation of the current's rise time and settling time (2%), which are determined to be 754 ms and 816 ms, respectively.

3.3.6 Comparison with Other Controllers

The proposed controller is evaluated against other controllers from the existing literature for non-ideal Buck and Boost converters. The controllers from the literature are implemented as described in their respective papers. To ensure comparable results, the parameters of the proposed converter and controller are adjusted accordingly.

We evaluate the MRAC-TCB control against another nonlinear control technique from [86] for the Buck converter. The controllers are tested for voltage reference tracking and load resistance variations. The results are presented in Fig. 3.25. Under the conditions of the proposed test, both MRAC-TCB controller and the Extended Feedback (FB) stabilization based controller exhibit good performance.

Both the MRAC-TCB controller and the Extended Feedback (FB) stabilization-based controller exhibit good performance under the tested conditions. Fig. 3.25(a) shows both controllers tracking the desired output voltage without overshoot or steady state errors. Fig. 3.25(b) illustrates the results when load resistance changes from 10 Ω to 15 Ω and back. The nominal output voltage is 12 V, as specified in Table I of [86].

For the Boost converter, we compare the MRAC-TCB with the Passivity-Based (PB) controller from [87]. The first test involves changing the load resistance from 30 Ω to 35 Ω at $t = 3$ s, then back to 30 Ω at $t = 5$ s. Fig. 3.26 displays the resulting changes in inductor current and output voltage.

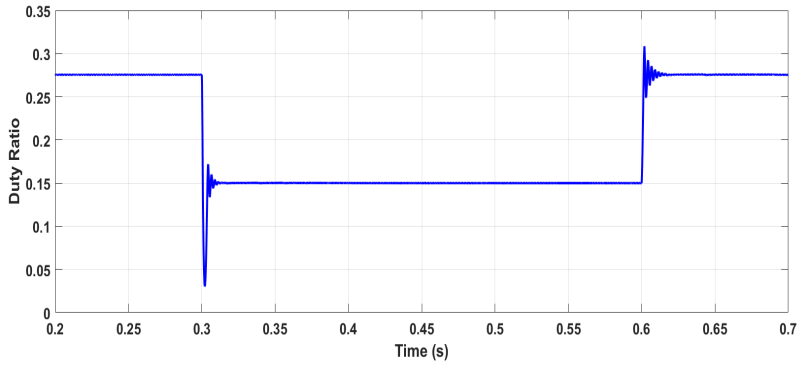

(a) Duty ratio u (control variable)

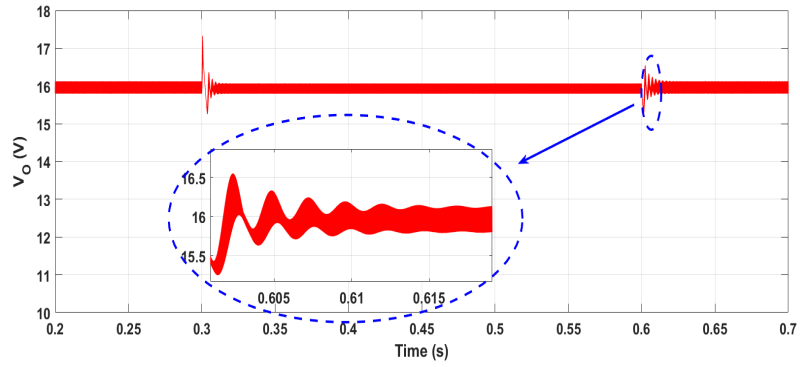

(b) Output voltage V_o

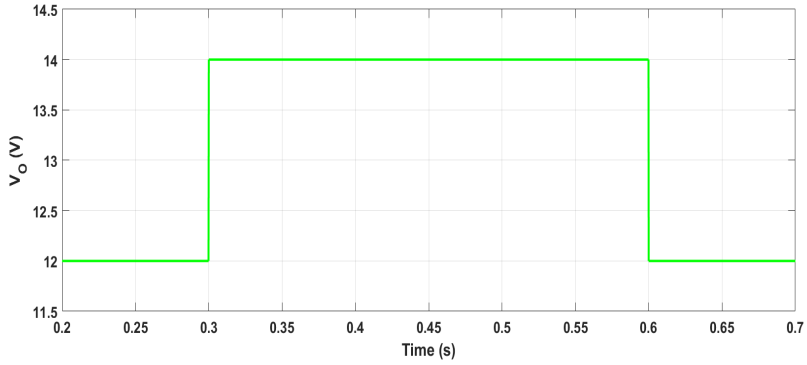

(c) Input voltage variation E

Fig. 3.24 Duty ratio and output voltage response to the input voltage variation from 5 V to 7 V in a given time interval for the Boost converter.

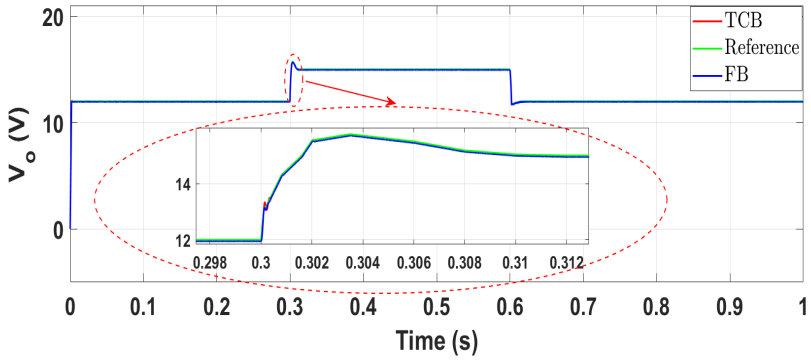

(a) Output voltage reference tracking

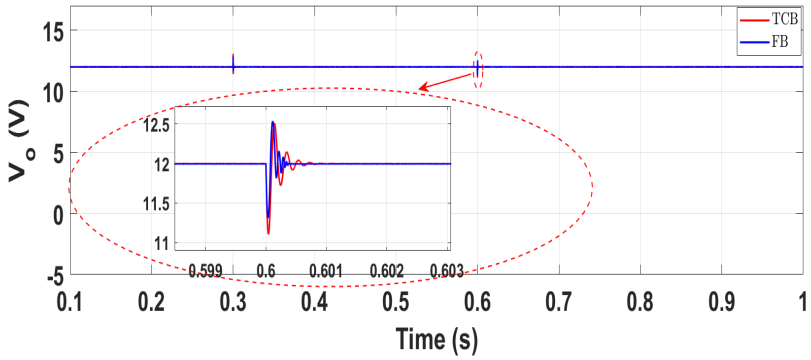

(b) Output voltage regulation under load variation

Fig. 3.25 Comparison between the MRAC-TCB and the feedback stabilization controls of a Buck converter under different conditions.

The second test examines input voltage variation using a fluctuating input voltage, as shown in Fig. 3.27(a). The output voltage response is presented in Fig. 3.27(b). The figure demonstrates that both controllers can track the reference voltage with minimal settling time and no steady state errors, despite significant and frequent input voltage fluctuations.

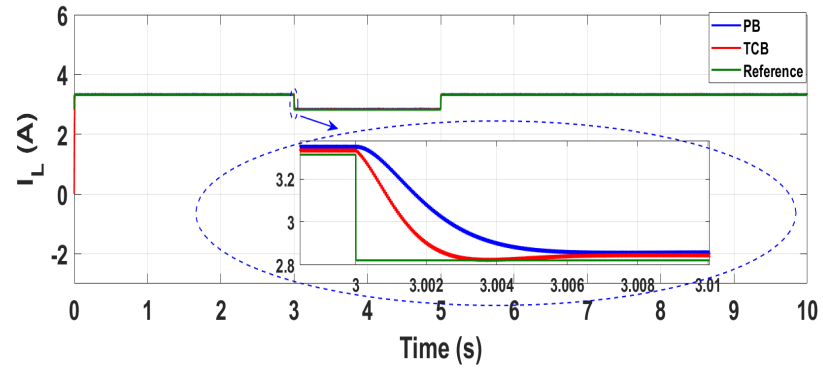

(a) Inductor current

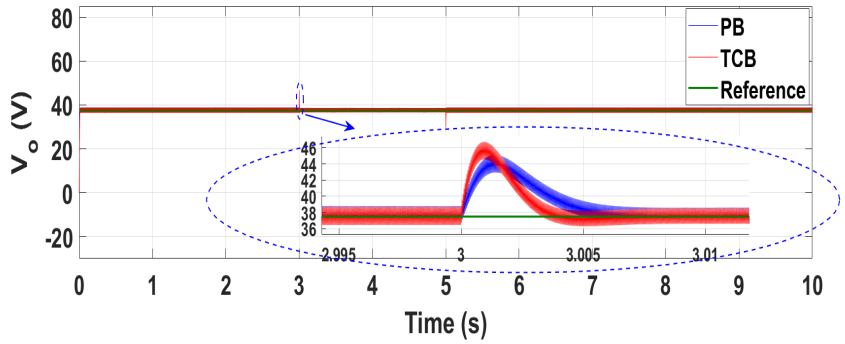

(b) Output Voltage

Fig. 3.26 Inductor current and Output voltage response comparisons due to load variations for the Boost converter.

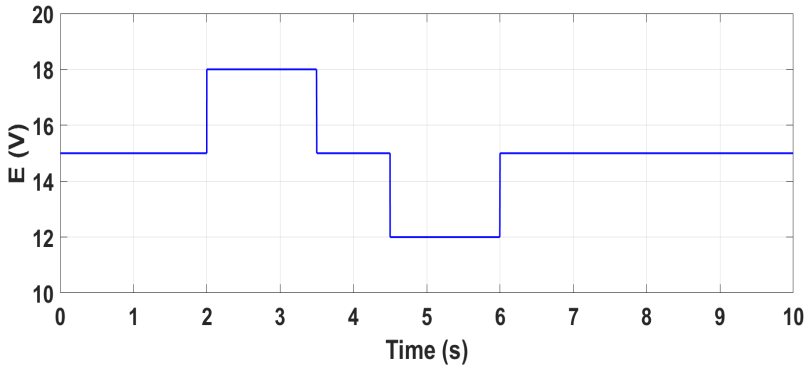

(a) Input Voltage

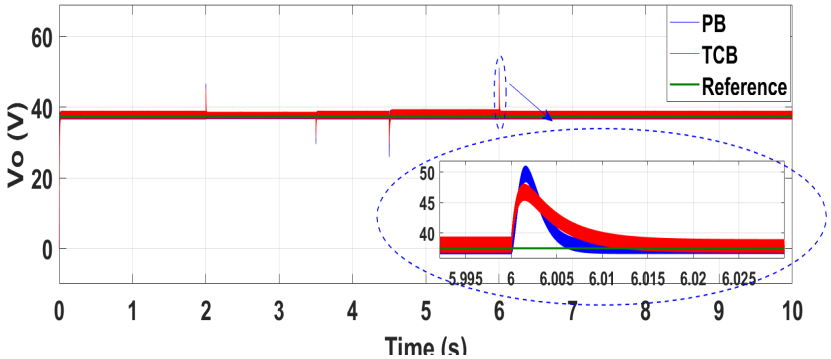

(b) Output Voltage

Fig. 3.27 Output voltage response comparisons due to fluctuations in the input voltage for the Boost converter.

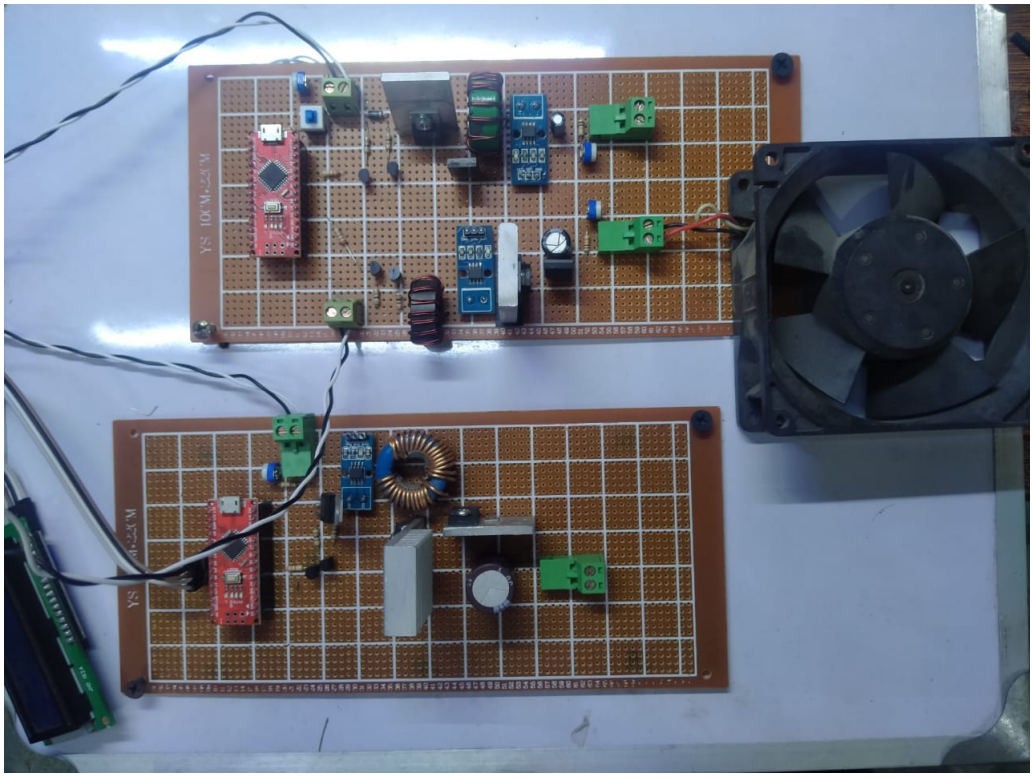

Fig. 3.28 Hardware Prototype of Buck and Boost converter built for experiment

3.3.7 Experimental Results

Test bench was created to validate the performance of the proposed controller through hardware experimentation. The parameters of the converters are those mentioned in the simulations. The converters were built on vero boards and microcontroller was used to implement the controller in hardware. Picture of the dedicated circuits of both buck and boost converter is shown in Fig 3.28.

Measurements were taken using a Teledyne LeCroy wavesurfer 3024z digital oscilloscope, featuring a 200 MHz bandwidth and 4 GS/s sampling rate.

The following subsections present the experimental test results.

Buck converter

Fig. 3.29 illustrates the experimental setup for controlling a MOSFET-based Buck converter. This setup consists of an Arduino microcontroller board and physical components of a Buck converter. The electronic load used has an equivalent resistance

of 47 Ω. Fig. 3.29 indicates the locations of voltage and current measurement points with corresponding probes.

Fig. 3.30 shows the inductor current over several switching periods. The switching frequency is 62.5 kHz. Fig. 3.31 presents the experimental waveforms of input and output voltages for successive input voltage changes. Note that the vertical scale for the output voltage is amplified tenfold compared to the input voltage scale. Even with this amplification, output voltage changes following input voltage variations are minimal. This demonstrates that the output voltage quickly adapts to the reference trajectory, confirming the excellent performance of the proposed MRAC-TCB controller.

Fig. 3.32 presents the waveforms of key experimental quantities as observed on the Matlab/Simulink control interface. Fig. 3.32(a) displays the sequential changes in input voltage. Correspondingly, Fig. 3.32(b) shows the output voltage's rapid variation and return to the reference value, demonstrating the swift adaptation of the proposed MRAC-TCB control. It's noteworthy that when starting from a point near the reference, the output voltage quickly aligns with the reference trajectory and maintains close proximity thereafter. Fig. 3.32(c) illustrates the duty ratio observed during the experimental test, highlighting how the adaptability of the duty ratio contributes to maintaining the output voltage close to the reference value.

Boost converter

The experimental setup of the Boost converter, shown in Fig. 3.29, is similar to the one done for Buck converter. Essentially, the buck converter board is replaced with the boost converter board.

Fig. 3.34 shows the input and output voltages of our experiment in which the input voltage undergoes successive changes. As shown in figure, the output voltage is able to track the reference trajectory after each variation of the input voltage with small variations. Furthermore, it can be seen that the output voltage adapts to the reference trajectory very quickly, hence highlighting the excellent robustness properties of our proposed MRAC-TCB controller.

Fig. 3.34 shows the waveforms of the relevant quantities seen on the Matlab-Simulink side. The successive changes in the input voltage are shown in Fig. 3.34(a), while the output voltage (Fig. 3.34(b)) remains close to the reference trajectory. Fig.

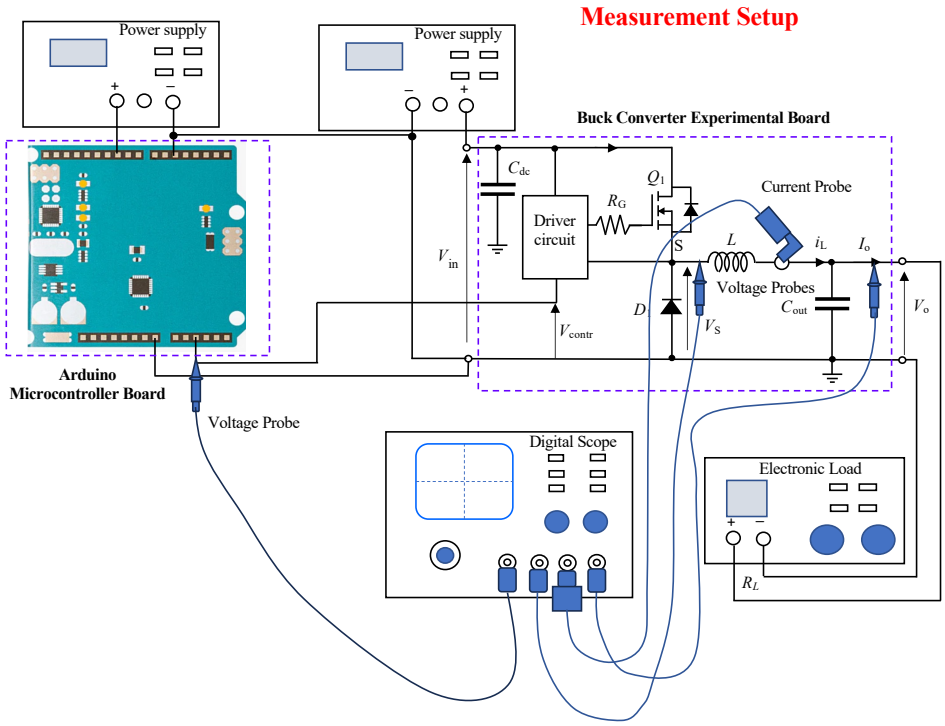

Fig. 3.29 Experimental setup of the circuits for controlling the Buck converter.

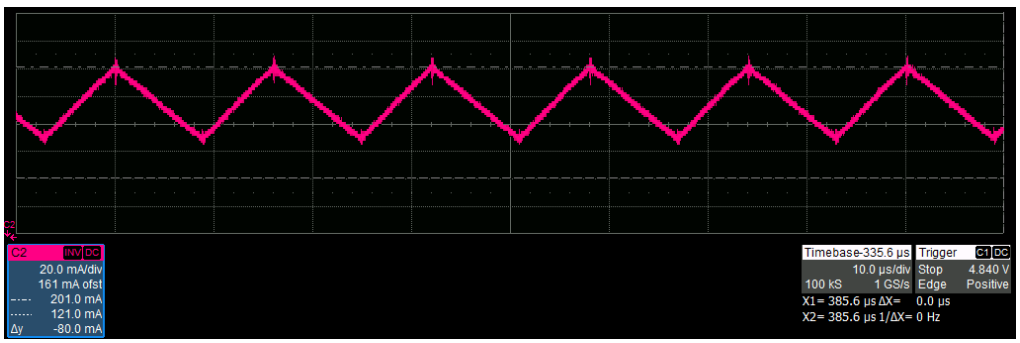

Fig. 3.30 Experimental waveform of the inductor current at steady state in the Buck converter operated under MRAC-TCB control.

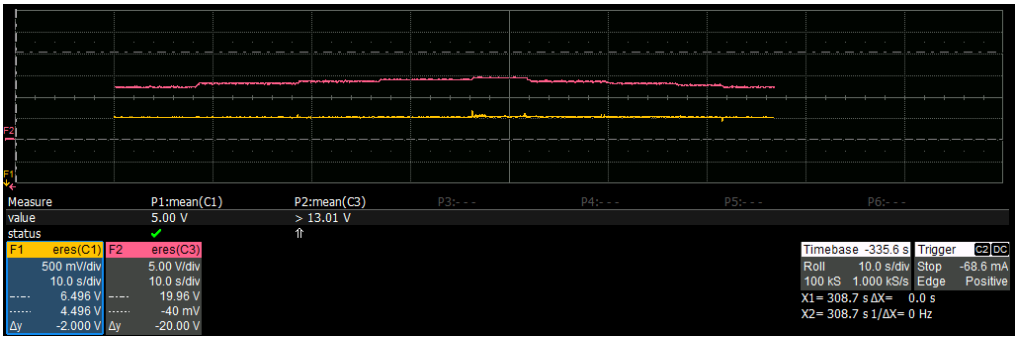

Fig. 3.31 Experimental waveforms for the input and output voltages in the Buck converter operated under MRAC-TCB control. The upper line is the input voltage, with vertical scale 5 V/division. The lower line is the output voltage, with vertical scale expanded to 0.5 V/division.

3.34(c) shows that the duty ratio resulting during the experimental test corresponds to the calculated values.

3.3.8 Concluding Remarks

This section has introduced an innovative control strategy for regulating and adaptively tracking reference signals in DC/DC power electronic converters. The controller integrates a model reference adaptive control approach with the Torelli Control Box technique as its control mechanism. The Lyapunov stability criterion is used to ensure the controller asymptotic stability. This control method is applied for the first time to non-ideal Buck and Boost converter configurations, incorporating model nonlinearities. While including these nonlinearities increases the control system's complexity, it is crucial for achieving precise converter regulation.

The effectiveness of the proposed controller for Buck and Boost converters has also been experimentally validated, demonstrating the exceptional performance of this control approach. To assess the proposed controller's performance, simulations have been conducted comparing it with other controllers from the existing literature. The results indicate that the proposed controller achieves comparable or superior outcomes under identical testing conditions.

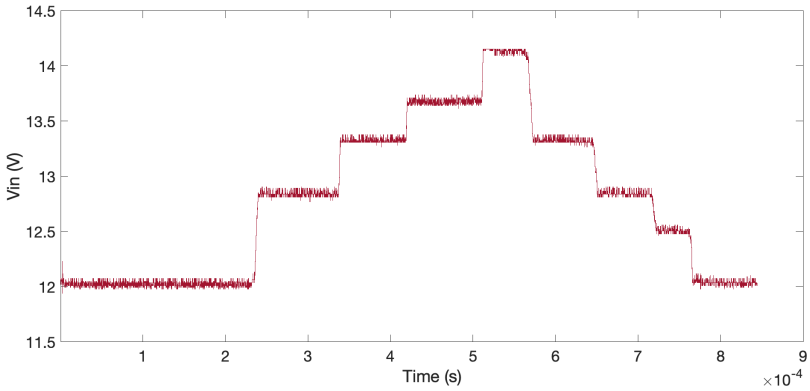

(a) Input voltage

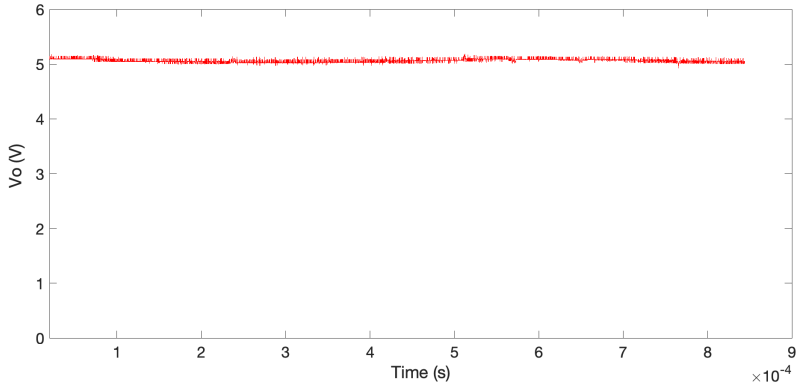

(b) Output voltage

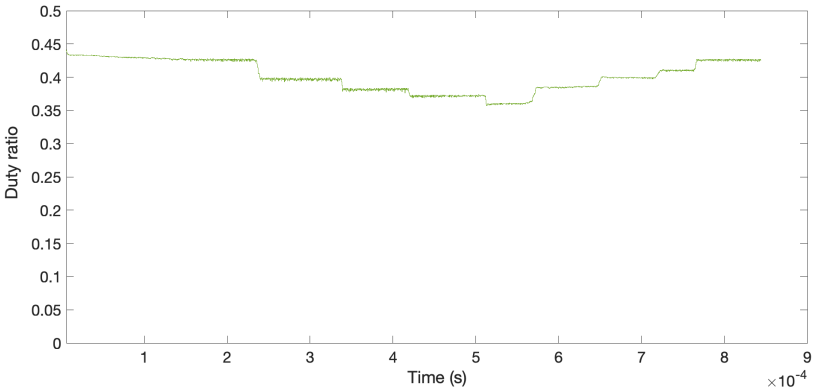

(c) Duty ratio

Fig. 3.32 Waveforms taken from the Matlab-Simulink side during the experimental test on the Buck converter.

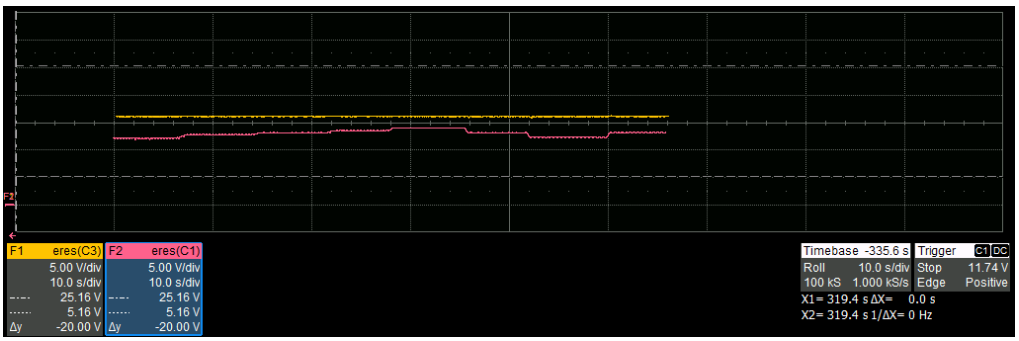

Fig. 3.33 Experimental waveforms for the input and output voltages in the Boost converter operated under MRAC-TCB control. The upper line is the output voltage. The lower line is the input voltage.

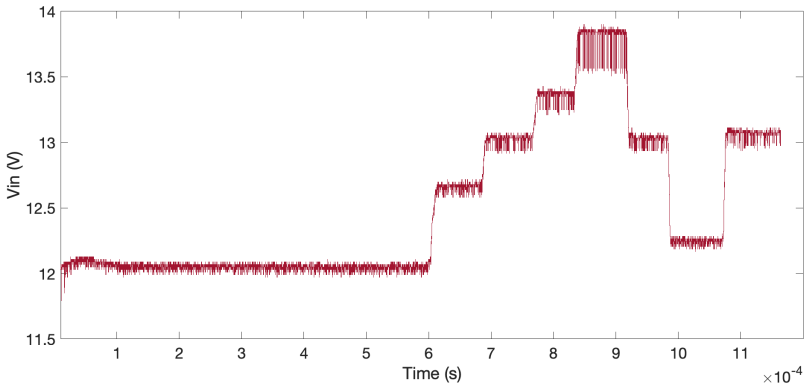

(a) Input voltage

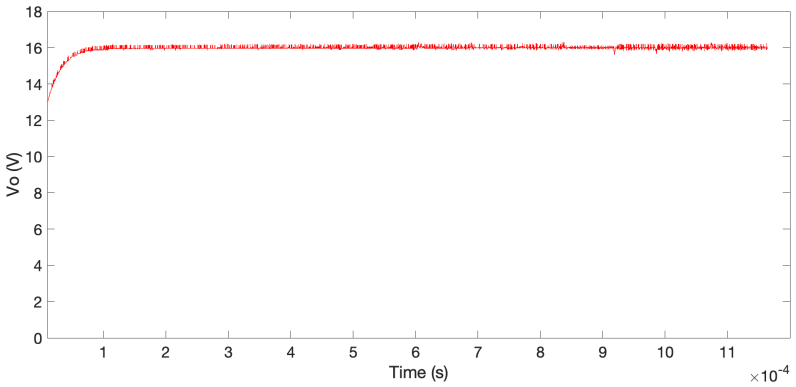

(b) Output voltage

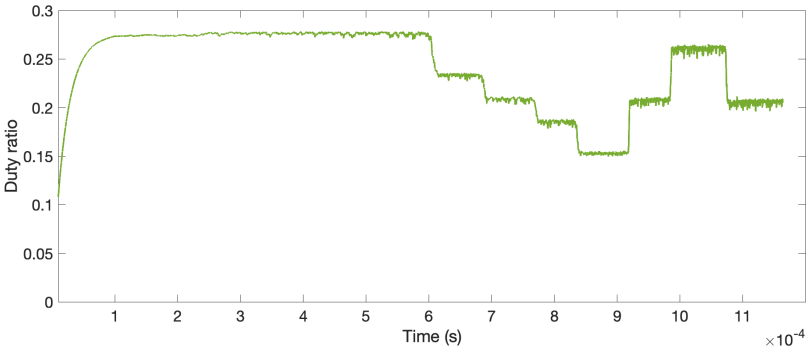

(c) Duty ratio (output)

Fig. 3.34 Waveforms taken from the Matlab-Simulink side during the experimental test on the Boost converter.

3.4 Application of the Adaptive Control Approach to Bidirectional Inverters for Vehicle to Grid

In this section, we present the use of TCB controller on a bidirectional inverter for Vehicle to Grid (V2G) applications. V2G allows bidirectional power transfer between EVs and the grid. It enables EVs to function as distributed energy resources that can either provide or consume power from the grid based on the grid status and user preferences. V2G has various advantages, such as frequency regulation, renewable energy integration, voltage support and peak shaving [88].

However, V2G also faces some technical difficulties that have been the focus of researchers. One key difficulty is to deal with the issue of a decline in power quality due to the nonlinear behavior of EV chargers. This is because these converters tend to draw nonsinusoidal currents from the grid, which can affect the grid voltage and lower the power factor. This low power factor results in higher losses, higher currents, and lower voltage levels in the grid [89].

A typical V2G system is shown in Fig. 3.35. It comprises typically of a bidirectional AC-DC power converter and a DC-DC power converter. The EV chargers consist of AC-DC converters, that in addition to converting AC power into DC, are also responsible for power factor correction. A commonly used single-phase AC-DC power converter used in EV chargers is shown in Fig. 3.36. The EV charger operates as a boost rectifier during the charging mode, keeping the output voltage at the reference value. Meanwhile, the DC-DC converter connected to it works in buck mode. In the discharging mode, we operate in the opposite direction. The output voltage of the battery is increased by the DC-DC converter while the AC-DC converter acts as an inverter and controls the active and reactive power delivered to the grid.

The controller has an important role in enhancing the power quality and the efficiency of the V2G system. In this section, we illustrate the application of the TCB-based adaptive controller for single-phase V2G technology that uses an active power factor correction circuit to improve the power quality and efficiency of EV chargers. We show the proposed controllers capability to ensure stability and robustness of the V2G system under different operating conditions and disturbances.

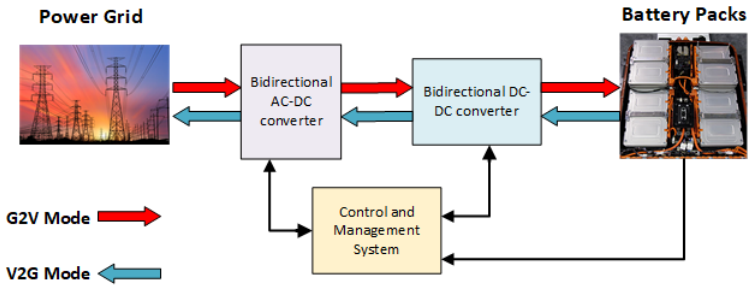

Fig. 3.35 Block diagram of Vehicle to Grid in EV

3.4.1 Derivation of the AC-DC Converter Model

The full-bridge bidirectional AC-DC power converter works by using four switches to control the flow of current between the input source and the output. The converter shown in Fig. 3.36 acts as a boost rectifier, which means that it increases the output voltage (V_{dc}) to be higher than the input source voltage (E). The inductor and capacitor are used to filter the grid current and voltage respectively, in order to reduce ripples and ensure a smooth and stable output. The inductor and capacitor in the full bridge bidirectional AC-DC power converter serve as filters. The inductor is used to filter the grid current while the bus capacitor is used to filter the voltage in order to reduce ripples. This helps to ensure a smooth and stable output from the converter.

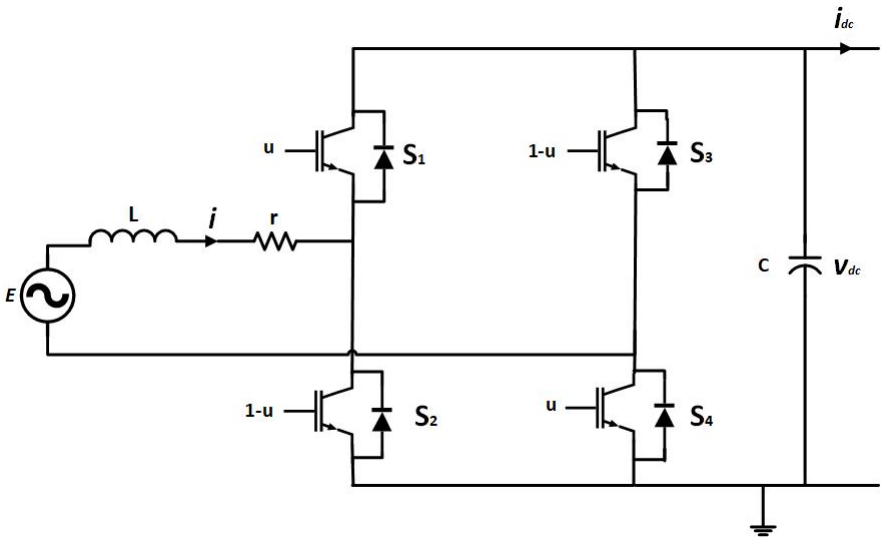

Fig. 3.36 Bidirectional AC-DC converter

The diagram of the AC-DC converter is shown in Fig. 3.36. The converter has two arms consisting of two switches each. The switches S_1 and S_4 are operated complementary to switches S_2 and S_3. The duty cycle u is used by a PWM circuit to operate the switches.

The direction of the current during the first half of cycle in grid-to-vehicle mode is shown in Fig. 3.37 while the direction of current flow during the second switching mode in V2G mode is shown in Fig. 3.37. Using the Kirchhoff's voltage and current laws, we can derive the following averaged mathematical model of the converter:

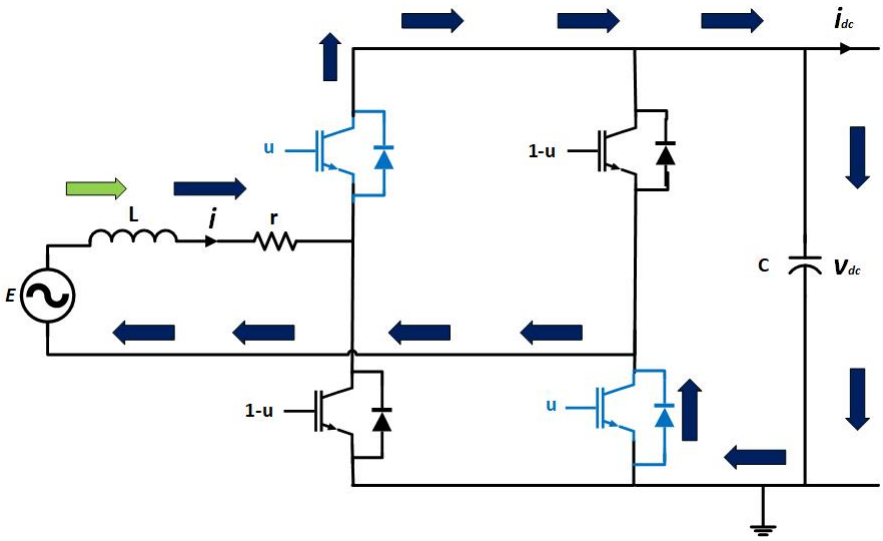

Fig. 3.37 Bidirectional AC-DC converter

$$\begin{cases} \dot{x}_1 = \dfrac{1}{L}[-x_1 r - x_2(2u-1) + E] \\ \dot{x}_2 = \dfrac{1}{C}[x_1(2u-1) - I_{dc}] \end{cases} \tag{3.28}$$

where x_1 and x_2 are the average grid current and average dc bus voltage respectively and u is the duty ratio that is used to generate PWM signals for the switches.

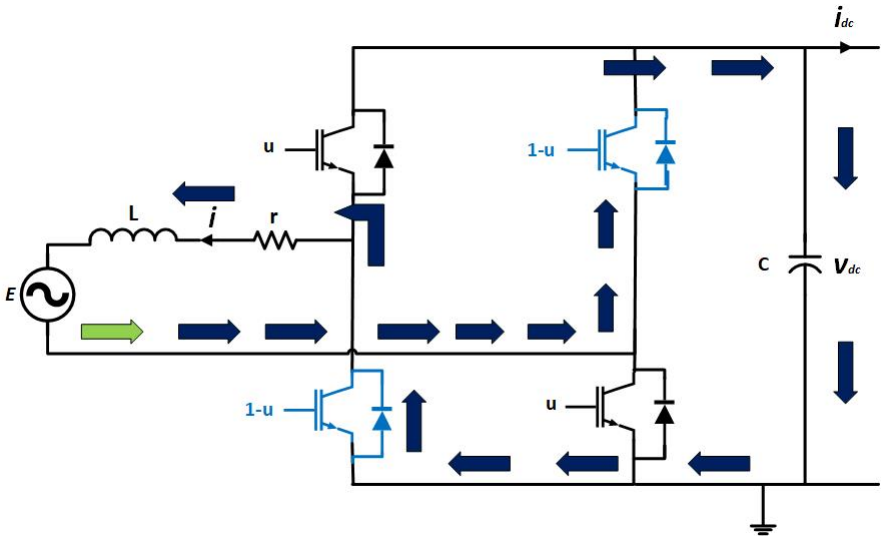

Fig. 3.38 Bidirectional AC-DC converter

3.4.2 Controller Formulation of the TCB-based Control Approach for the AC-DC Converter

As discussed before, the first step is the generation of the reference signal that would govern the behavior of the converter parameters. Let the vector of the state variable be $\mathbf{x} = \{ x_1, x_2\}$, control variable vector $\mathbf{u} = \{\mathrm{u}\}$ and the algebraic variable $\mathbf{y} = \{y_{r0}\}$.

For the second step we need to derive the coordinates of the equilibrium point in the composite domain ($\mathbf{x}$, $\mathbf{u}$), denoted as ($\mathbf{x}$*, $\mathbf{u}$*). This step is done by setting Equation (3.28) to zero and hence finding the steady state values of equilibrium points.

$$\begin{cases} x_1^* = \alpha E \\ x_2^* = y_{r0} \\ u^* = \frac{E+2y_{r0}-\sqrt{E_1^2-4I_{dc}ry_{r0}}}{4y_{r0}} \end{cases} \tag{3.29}$$

where α is given by:

$$\alpha = \frac{y_{r0}}{V^2}(-c_2 e_{x_2} C + i_{DC}) \tag{3.30}$$

This expression has been derived in [90] and establishes the relationship between the desired grid current and the grid voltage.

The third step is to design the adaptation mechanism for the minimization of the following tracking errors:

$$\begin{cases} e_{x_1} = w_{x_1}(x_1 - x_1^*) \\ e_{x_2} = w_{x_2}(x_2 - x_2^*) \\ e_u = w_u(u - u^*) \end{cases} \tag{3.31}$$

Based on Equation (3.29) and the error vectors defined above, the expression for the control equation becomes:

$$\dot{u} = -K\left[\frac{dx_1}{du} w_{x_1}^2 (x_1 - x_1^*) + \frac{dx_2}{du} w_{x_2}^2 (x_2 - x_2^*) + w_u^2 (u - u^*)\right] \tag{3.32}$$

where K is the gain factor, with constant value and w_{x_1}, w_{x_2} and w_u are weights defined for system respectively.

The sensitivity parameters $s_1 = \frac{dx_1}{du}$ and $s_2 = \frac{dx_2}{du}$ are calculated based on the converter model given in Equation (3.28):

$$\begin{cases} \dot{s}_1 = -\dfrac{1}{L}(-s_1 r - 2s_2 u - 2x_2 + y_2) \\ \dot{s}_2 = \dfrac{1}{C}(2s_1 u + 2x_1 - y_1) \end{cases} \tag{3.33}$$

3.4.3 Simulation Results for the AC-DC Converter

The simulation for the bidirectional converter has been done in Matlab/Simulink environment using ODE 45 solver. The parameters used for converter and the value of controller gains is given in Table 3.8 and Table 3.9. As mentioned before, the aim of the controller design is to ensure constant reference voltage tracking of the DC voltage and unitary power factor of the grid voltage and current in face of variations in load conditions.

In each test result, the load current of the converter has been varied as shown in Fig. 3.39. As seen from the figure, the load current is kept constant at 5 A for time t = 0 to t = 0.4 s before being increased to 10 A till time t = 0.7 s. At this moment, the

Table 3.8 Specifications of AC-DC Converter

Description of parameters	Nominal value
Input voltage, E (RMS)	230 V
Reference output voltage, V_o	400 V
Capacitance, C	3000 uF
Inductance, L	4.06 mH
Load Current, A	5 A
Switching frequency, f_s	10 kHz
Inductor resistance, R_L	0.1 Ω

Table 3.9 Controller Gains

Description of parameters	Nominal value
TCB Gain, K	0.035
α_1	3
α_2	0.5
β	7
c_2	50

load current is stepped down to -5 A to show the performance of the controller in the inverter mode as well. The large sudden variations in the load current have been used to test the robustness of the control under extreme conditions.

Fig. 3.40 shows the DC output voltage of the converter with the reference voltage set to 400 V, while Fig. 3.41 shows the grid current under conditions of variable load current. We can see from both figures the effects of sudden variations in the load current. At 0.4 s as the load current requirement is increased, the the grid current also increases but as the load current requirement is reversed, i.e. we operate in V2G mode, the phase of grid current shifts. This change in phase of grid current can be seen better in Fig. 3.42 which shows that the phase of grid current is opposite to that of Grid voltage after t = 0.7s.

3.4.4 Comparison with a Lyapunov Redesign-based Controller

To evaluate our controller's effectiveness, we reproduced a Lyapunov redesign based controller (LC) from the literature [90]. Both controllers were subject to identical external disturbances in the load current. Fig. 3.43 displays the DC output voltage for both controllers.

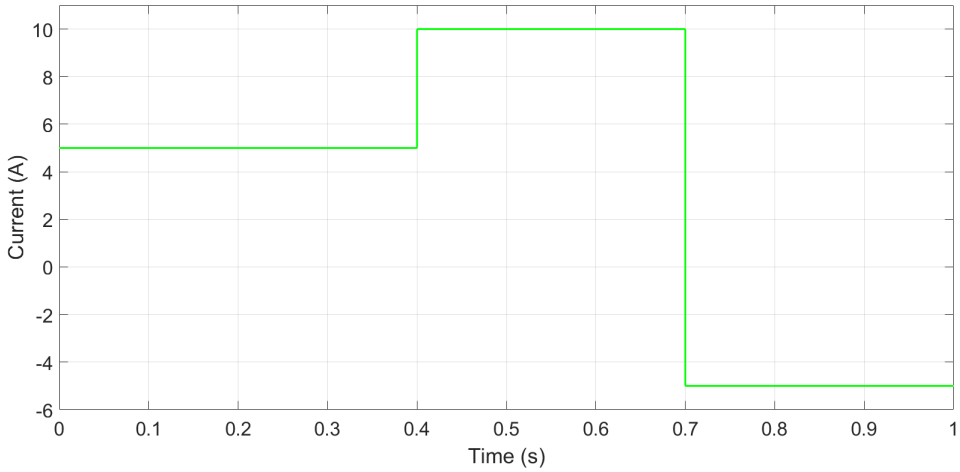

Fig. 3.39 DC load current.

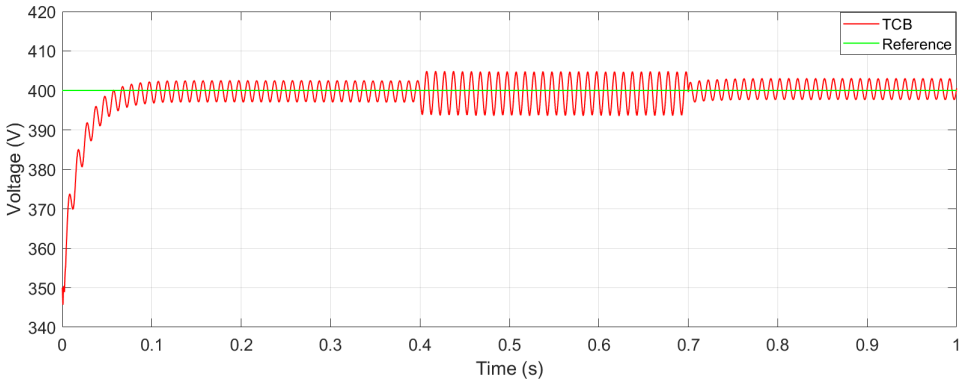

Fig. 3.40 DC bus voltage.

The figure demonstrates that both controllers perform exceptionally well under the given conditions. Neither controller exhibits voltage overshoot, and they show almost comparable rise times. The TCB controller offers a minor additional advantage of a slightly reduced ripple magnitude.

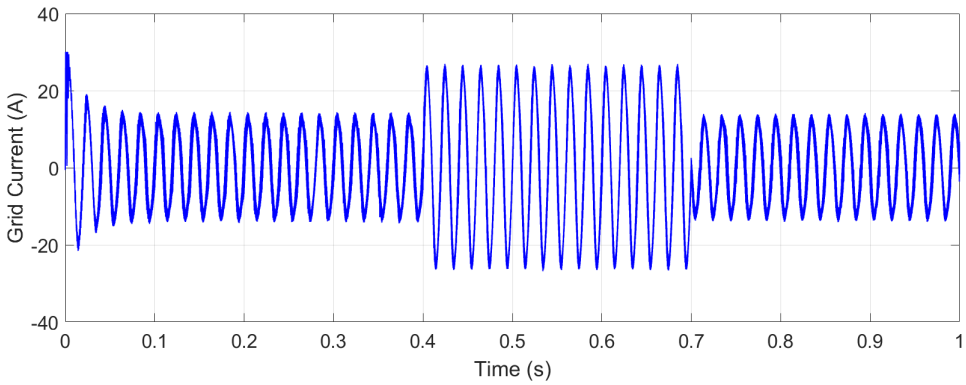

Fig. 3.41 Grid current.

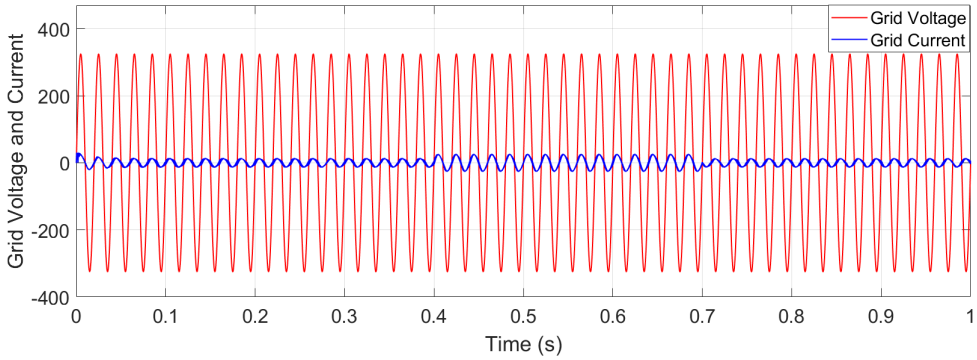

Fig. 3.42 Grid voltage and grid current.

3.4.5 Concluding Remarks

In this section, the use of the TCB controller has been demonstrated for single-phase Vehicle to Grid technology to enhance the power quality and efficiency of EV chargers. The controller can dynamically change the output power of the EV charger based on the grid conditions and user preferences while keeping a high power factor and low harmonic distortion. The controller also guarantees the stability and robustness of the V2G system under various operating conditions and disturbances.

The simulations for this application were conducted in MATLAB/Simulink environment. The controller's robustness has been rigorously tested by applying extreme variations in the load current required from the AC-DC bidirectional converter. The results indicate that the TCB controller performs comparatively well with respect to the other Lyapunov redesign-based controller proposed in the literature.

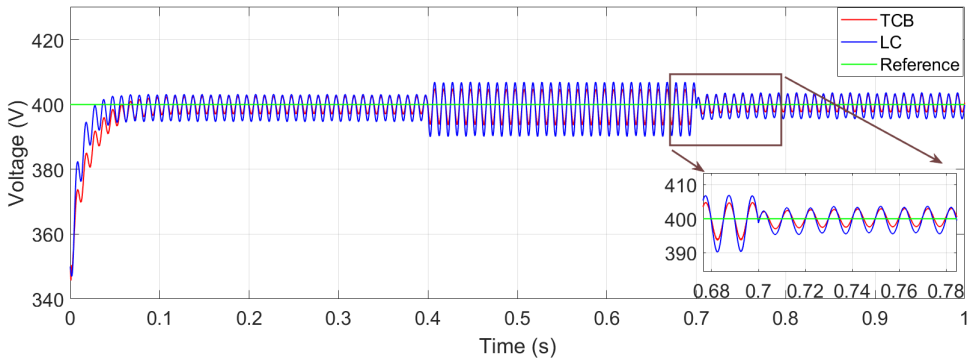

Fig. 3.43 DC Voltage output comparison

Chapter 4

Regulation of a Three-phase Inverter for UPS application

4.1 Introduction to Three-phase Voltage Source Inverter

Three-phase inverters play a crucial role in modern electrical systems. Their ability to convert Direct Current (DC) to Alternating Current (AC) is absolutely fundamental for the operation of many industries ranging from industrial automation to renewable energy systems. It is of utmost importance that these three-phase inverters are able to provide robust performance, reliability, and flexibility even in increasingly harsh operating circumstances.

A three-phase inverter converts DC input into three-phase AC output by employing power electronic components such as insulated-gate bipolar transistors (IGBTs) or metal-oxide-semiconductor field-effect transistors (MOSFETs). The primary function of these inverters is to generate three sinusoidal voltages that are 120 degrees out of phase with each other, which are essential for powering three-phase loads. The inverter's operation is governed by modulation techniques such as PWM, which ensures smooth and precise control of the output voltage and frequency.

In industrial settings, three-phase inverters are used in driving AC motors, which are at the basis of many manufacturing and processing plants. They enable precise control over motor speed and torque, thereby providing optimized performance in

applications such as conveyors, pumps, fans, and compressors. Moreover, these inverters are also essential components in Uninterruptible Power Supply (UPS) systems, providing an AC power source during conditions of grid failures. It is absolutely essential that the UPS is able to perform reliably and achieve good output voltage regulation as they are often used to provide power to critical equipment such as medical equipment, data centers and communication systems [91].

In commercial buildings, three-phase inverters are increasingly used in HVAC (heating, ventilation, and air conditioning) systems. These systems require three-phase inverters to control and maintain the speed of compressor, fans and other equipments. This is done to ensure adequate comfort levels of residential and commercial buildings but also to make the overall system more energy efficient [92].

The three-phase inverters are also a backbone of modern electrically propelled vehicles. In EVs or hybrid vehicles, inverters convert the DC from the battery into AC to drive the electric motor. They also play a crucial role for the operation of power traction motors of electric trains and trams ensuring their smooth operation.

The telecommunications infrastructure relies on three-phase inverters to maintain stable power supply systems, particularly in remote or off-grid locations. These inverters are critical in ensuring uninterrupted communication services. In agriculture, three-phase inverters are utilized in variable-frequency drives to control water pumps in irrigation systems, improving energy efficiency and water management. They are also used in grain handling and processing machinery, ensuring efficient operation and processing.

Finally, one of the most important contribution of three-phase inverters has been their role in the modern renewable sources based energy systems. In solar PV systems, these inverters convert the DC output from solar panels into AC power suitable for the electrical grid or local consumption. Similarly, in wind energy systems, three-phase inverters are used to convert the variable frequency AC generated by wind turbines into a stable AC supply, facilitating efficient integration with the grid. These applications are crucial for harnessing renewable energy and reducing dependence on fossil fuels. This topic will be explored in more detail in the next chapter which will focus on the role of three-phase inverters acting as Grid-Forming (GFM) Inverters.

No matter the application, it is absolutely necessary that the three-phase inverter must be able to deliver reliable, high-quality power under various operational conditions. It is the responsibility of the control system to ensure that the inverter is able

to provide a rapid dynamic response under varying load conditions, a minimal Total Harmonic Distortion (THD) in the output voltage, and a robust tracking performance. The controller should also be able to provide assured stability, and strong resilience against model mismatches and parameter variations. These attributes ensure that the inverter consistently provides reliable performance, even in the face of challenging operational conditions. The importance of a robust control mechanism for a three-phase inverter cannot be overstated.

In the literature, various control strategies for PWM converters have been introduced aiming to achieve high power factor and minimal harmonic distortion in input line currents. Some of the linear control strategies that have been proposed in papers are Phase and Amplitude Control (PAC) [93, 94], Hysteresis Current Control (HCC) [95, 96], and Predicted Current Control with Fixed Switching Frequency (PCFF) [97]. As with all control methodologies, these techniques have their advantages and disadvantages. PAC is effective in reducing steady-state current harmonics and output voltage ripple, but it introduces a DC current component on the AC side, negatively impacting the DC load current and voltage during transients. HCC offers fast dynamic response, high accuracy, no DC offset, and strong robustness. However, its average switching frequency varies with the DC load current, leading to uneven and random switching patterns that impose additional stress on the switching devices. PCFF provides a fast dynamic response and a consistent switching pattern, which reduces stress on switching devices, but it is sensitive to parameter variations.

These control strategies along with other linear control techniques offer a range of benefits and drawbacks ranging from complexity of the control circuit, switching frequencies, to complications in transient responses. One common drawback among all the linear approaches is their inability to ensure system stability during large-signal disturbances. The state-space-averaged models of PWM inverters, derived using these strategies, are known to be nonlinear systems. Due to the challenges associated with controlling such nonlinear systems, much of the previous research has focused on applying linear control theory to small-signal linearized models of these DC-AC converters. However, these control laws typically only ensure system stability for small perturbations around the operating points of both state and input variables. Therefore, it is highly desirable to develop control strategies that can achieve global stability for the AC/DC converter without resorting to linearization of its mathematical model.

Given the importance of the three-phase inverter, different nonlinear control strategies have also been proposed to provide an improved response from the system. One of the frequently employed techniques is that of Model Predictive Control (MPC) that has been used for the regulation of a three-phase UPS system [98–100]. While an MPC is simple to implement, it is computationally demanding and its results do not show exceptional performance in terms of steady-state error and THD even when augmented with a current observer. Additionally, MPC relies on system parameters, which can be a limitation.

Another control approach is based on deadbeat controller. While it provides an exceptional response during transients, its performance is highly dependent on model uncertainties and parameter perturbations [101, 102]. The controller tends to become unstable if the parameters are not known exactly.

Unlike the deadbeat control approach, H_∞ controllers are based on robust control theory and are capable of handling system uncertainties. Nevertheless, the controllers generated using the method outlined in [103] are often too intricate for digital processors due to their high order. To address this, a suitable order reduction process is necessary to create a manageable controller, but this process may compromise the characteristics of the original controller. Additionally, the design specifications of these methods, including weighting functions and perturbation models, are complex, which can be seen as another disadvantage.

Another method based on feedback-linearization approach is proposed in [104]. The controller is able to obtain adequate total harmonic distortion results for both linear and nonlinear loads but it does not take into account the control performance under parametric uncertainties.

Among the traditional Lyapunov-based control approaches, Sliding mode control-based methodologies have been widely applied for the regulation of three-phase inverters [105], [106]. Sliding mode control is used because it is capable of providing protection against parametric uncertainties and offer a robust response in dynamic conditions. However, the drawback of SMC is that it suffers from time-varying frequency and chattering phenomenon.

Another Lyapunov function-based approach is based on the use of Lyapunov energy function. This methodology has been used for the regulation of a rectifier and an active filter application respectively [107, 108]. In the derivation of this approach, it is ensured that the derivative of the Lyapunov function is negative under

all possible operating conditions. However, this approach suffers from considerable steady-state error and large amount of total harmonic distortion in the output voltage. This methodology has been recently improved upon in [91] by the introduction of output voltage feedback loops. This results in considerable mitigation of steady-state errors and improvement in harmonics in the output voltage. This research work also compares its performance against deadbeat and SMC controllers presented in the literature and highlights the advantages of their proposed approach. Due to the excellent performance of this controller, we have used the controller as a benchmark to compare against the TCB-based controller.

In this section, the aim is to show the performance of the TCB-based control approach for a three-phase standalone inverter. In the simulations performed in Matlab/Simulink, the inverter specifications have been proposed for its application in as a UPS system. It has been tested under various dynamic conditions and its superior performance has been highlighted. Furthermore, its comparison with the performance of another improved Lyapunov-based control approach is shown as well.

Section 4.2 shows the mathematical model of the three-phase inverter system that is used to derive the TCB control approach. Section 4.3 shows the application of the TCB-based control approach. The results are shown in Section 4.4, while the concluding remarks are drawn in Section 4.5.

4.2 Three-phase Inverter Modeling

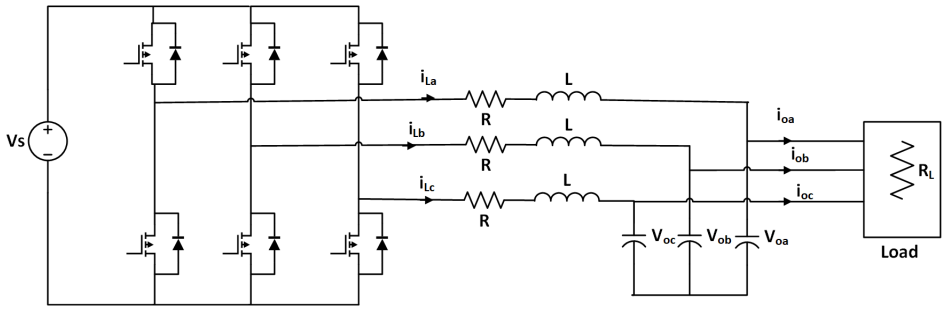

Fig. 4.1 Three-phase inverter with LC filter.

A three-phase inverter with LC filter is shown in Fig. 4.1. The mathematical model can be derived using Kirchhoff's current and voltage laws as follows:

$$\begin{cases} \frac{di_{La}}{dt} &= \frac{1}{L}(\frac{\mu_a V_s}{2} - Ri_{La} - v_{oa}) \\ \frac{di_{Lb}}{dt} &= \frac{1}{L}(\frac{\mu_b V_s}{2} - Ri_{Lb} - v_{ob}) \\ \frac{di_{Lc}}{dt} &= \frac{1}{L}(\frac{\mu_b V_s}{2} - Ri_{Lc} - v_{oc}) \\ \frac{dv_{oa}}{dt} &= \frac{1}{C}(i_{La} - i_{oa}) \\ \frac{dv_{ob}}{dt} &= \frac{1}{C}(i_{Lb} - i_{ob}) \\ \frac{dv_{oc}}{dt} &= \frac{1}{C}(i_{Lc} - i_{oc}) \end{cases} \tag{4.1}$$

where i_{La}, i_{lb} and i_{lc} are the the three-phase inductor currents expressed in the *abc* frame, similarly V_{oa}, V_{ob} and V_{oc} are output capacitor voltages expressed in the *abc* reference frame, and finally i_{oa}, i_{ob} and i_{oc} are the load currents.

The inputs to the system are the *abc* components of duty ratio, defined as μ_a, μ_b and μ_c, while L, C, R and R_L are the inductor, capacitor, inductor resistance and load values of the converter, respectively.

$$\begin{cases} \frac{di_{La}}{dt} &= \frac{1}{L}(\frac{\mu_a V_s}{2} - Ri_{La} - v_{oa}) \\ \frac{di_{Lb}}{dt} &= \frac{1}{L}(\frac{\mu_b V_s}{2} - Ri_{Lb} - v_{ob}) \\ \frac{di_{Lc}}{dt} &= \frac{1}{L}(\frac{\mu_b V_s}{2} - Ri_{Lc} - v_{oc}) \\ \frac{dv_{oa}}{dt} &= \frac{1}{C}(i_{La} - i_{oa}) \\ \frac{dv_{ob}}{dt} &= \frac{1}{C}(i_{Lb} - i_{ob}) \\ \frac{dv_{oc}}{dt} &= \frac{1}{C}(i_{Lc} - i_{oc}) \end{cases} \tag{4.2}$$

If we define the average inductor currents i_{La}, i_{Lb} and i_{Lc} as x_1, x_2 and x_3, and the average output voltages V_{oa}, V_{ob} and V_{oc} as x_4, x_5 and x_6, we get the following differential equations:

$$\begin{cases} \dot{x}_1 &= \frac{1}{2}\mu_a V_s - Rx_1 - x_4 \\ \dot{x}_2 &= \frac{1}{2}\mu_b V_s - Rx_2 - x_5 \\ \dot{x}_3 &= \frac{1}{2}\mu_c V_s - Rx_3 - x_6 \\ \dot{x}_4 &= x_1 - i_{oa} \\ \dot{x}_5 &= x_2 - i_{ob} \\ \dot{x}_6 &= x_3 - i_{oc} \end{cases} \tag{4.3}$$

4.3 Application of the MRAC-TCB Approach to a Three-phase Voltage-controlled Inverter

The TCB approach as mentioned previously can be broken down into three steps. In the first step, we can design a reference signal based on the desired trajectory of our output signal. In this particular case, the reference signal for our desired output denoted as y_{r0} are three sinusoidal waveforms generated in the *abc* reference frame. The general equation of these waveforms can be given by:

$$y_{r0} = A_m sin(\omega t) + \phi \tag{4.4}$$

where A_m is the desired reference amplitude, ω is the reference frequency and ϕ is the desired phase.

The second step is the derivation of the state variables response in steady-state in terms of the desired reference signal, y_{r0}. This can be done by equating equation (4.3) to zero. We get the following equations for the ideal response of the state variables:

$$\begin{cases} x_1^* = i_{oa} \\ x_2^* = i_{ob} \\ x_3^* = i_{oc} \\ x_4^* = y_{r0a} \\ x_5^* = y_{r0b} \\ x_6^* = y_{r0c} \\ u_a^* = \frac{2y_{r0a}(R+R_L)}{R_L V_S} \\ u_b^* = \frac{2y_{r0b}(R+R_L)}{R_L V_S} \\ u_c^* = \frac{2y_{r0c}(R+R_L)}{R_L V_S} \end{cases} \tag{4.5}$$

The third step is to design the adaptation mechanism for the minimization of the following tracking errors:

$$\begin{cases} e_1 = \alpha_1(x_1 - x_1^*) \\ e_2 = \alpha_1(x_2 - x_2^*) \\ e_3 = \alpha_1(x_3 - x_3^*) \\ e_4 = \alpha_2(x_4 - x_4^*) \\ e_5 = \alpha_2(x_5 - x_5^*) \\ e_6 = \alpha_2(x_6 - x_6^*) \\ e_7 = \beta(u_a - u_a^*) \\ e_8 = \beta(u_b - u_b^*) \\ e_9 = \beta(u_c - u_c^*) \end{cases} \tag{4.6}$$

Here, once again α_1, α_2, and β are weight vectors determined empirically. Using (1.37), the control equations for u_a, u_b and u_c come out as follows:

$$\dot{u}_a = -K\left[\alpha_1^2 v_1 e_1 + \alpha_1^2 v_2 e_2 + \alpha_2^2 v_3 e_3 + \alpha_2^2 v_4 e_4 + \alpha_2^2 v_5 e_5 + \alpha_2^2 v_6 e_6 + \beta^2 e_7 + \beta^2 e_8 + \beta^2 e_9\right] \tag{4.7}$$

$$\dot{u}_b = -K\left[\alpha_1^2 y_1 e_1 + \alpha_1^2 y_2 e_2 + \alpha_2^2 y_3 e_3 + \alpha_2^2 y_4 e_4 + \alpha_2^2 y_5 e_5 + \alpha_2^2 y_6 e_6 + \beta^2 e_7 + \beta^2 e_8 + \beta^2 e_9\right] \tag{4.8}$$

$$\dot{u}_c = -K\left[\alpha_1^2 z_1 e_1 + \alpha_1^2 z_2 e_2 + \alpha_2^2 z_3 e_3 + \alpha_2^2 z_4 e_4 + \alpha_2^2 z_5 e_5 + \alpha_2^2 z_6 e_6 + \beta^2 e_7 + \beta^2 e_8 + \beta^2 e_9\right] \tag{4.9}$$

where K is the gain factor with a constant value given in Table 4.1.

Here the sensitivity parameters $\mathbf{v}$, $\mathbf{y}$ and $\mathbf{z}$ are represented by $\frac{d\mathbf{x}}{du_a}$, $\frac{d\mathbf{x}}{du_b}$ and $\frac{d\mathbf{x}}{du_c}$, respectively.

$$\begin{cases} \dot{v}_1 = \dfrac{1}{L}(\dfrac{Vs}{2} - Rv_1 - v_4) \\ \dot{v}_2 = \dfrac{1}{L}(-Rv_2 - v_5) \\ \dot{v}_3 = \dfrac{1}{L}(-Rv_3 - v_6) \\ \dot{v}_4 = \dfrac{1}{C}(v_1 - \dfrac{v_4}{R_L}) \\ \dot{v}_5 = \dfrac{1}{C}(v_2 - \dfrac{v_5}{R_L}) \\ \dot{v}_6 = \dfrac{1}{C}(v_3 - \dfrac{v_6}{R_L}) \end{cases} \tag{4.10}$$

Similarly, we can derive the equations for the sensitivity parameters **y** and **z**.

$$\begin{cases} \dot{y}_1 = \dfrac{1}{L}(-Ry_1 - y_4) \\ \dot{y}_2 = \dfrac{1}{L}(\dfrac{Vs}{2} - Ry_2 - y_5) \\ \dot{y}_3 = \dfrac{1}{L}(-Ry_3 - y_6) \\ \dot{y}_4 = \dfrac{1}{C}(y_1 - \dfrac{y_4}{R_L}) \\ \dot{y}_5 = \dfrac{1}{C}(y_2 - \dfrac{y_5}{R_L}) \\ \dot{y}_6 = \dfrac{1}{C}(y_3 - \dfrac{y_6}{R_L}) \end{cases} \tag{4.11}$$

$$\begin{cases} \dot{z}_1 = \dfrac{1}{L}(-Rz_1 - z_4) \\ \dot{z}_2 = \dfrac{1}{L}(-Rz_2 - z_5) \\ \dot{z}_3 = \dfrac{1}{L}(\dfrac{Vs}{2} - Rz_3 - z_6) \\ \dot{z}_4 = \dfrac{1}{C}(z_1 - \dfrac{z_4}{R_L}) \\ \dot{z}_5 = \dfrac{1}{C}(z_2 - \dfrac{z_5}{R_L}) \\ \dot{z}_6 = \dfrac{1}{C}(z_3 - \dfrac{z_6}{R_L}) \end{cases} \tag{4.12}$$

Table 4.1 Specifications of the Three-phase Inverter

Description of parameters	Nominal value
Input voltage, V_S	350 V
Reference output voltage, V_{Oref}	170 V
Capacitance, C	25 uF
Inductance, L	6 mH
Inductor Resistance, R	0.1 Ω
Switching frequency, f_s	10 kHz

Table 4.2 Controller Gains and Observer Gains

Description of parameters	Nominal value
Controller Gain, K	6000
α_1	0.25
α_2	0.080
β	4.0
γ	0.35
k_1	1.25 x 10^3
k_2	1.25 x 10^3
k_3	1.75 x 10^4
k_4	1.75 x 10^4

4.4 Simulation Results

This section outlines the results of our proposed control method's simulation. Table 4.1 lists the parameters used for the three-phase inverter, while Table 4.2 details the control gains for the TCB controller. All simulations were conducted using Matlab/Simulink.

Fig. 4.2 shows the block diagram of our TCB based control system. As shown in the figure, we need sensors to measure Inductor and load currents (shown in blue) and capacitor voltages (shown in red). These values are used by TCB controller to generate μ_{abc} which are then used to drive the PWM generator.

The goal is to evaluate the robustness and adaptability of our controller in various scenarios. The first section presents the results when the control system is tested with a linear (resistive) load, while the second section displays the response with nonlinear loads.

4.4.1 Linear Load

Initially, the converter is run under 5 kW load conditions. To test the response of the controller, the load is suddenly doubled to 10 kW and then doubled again to 20 kW.

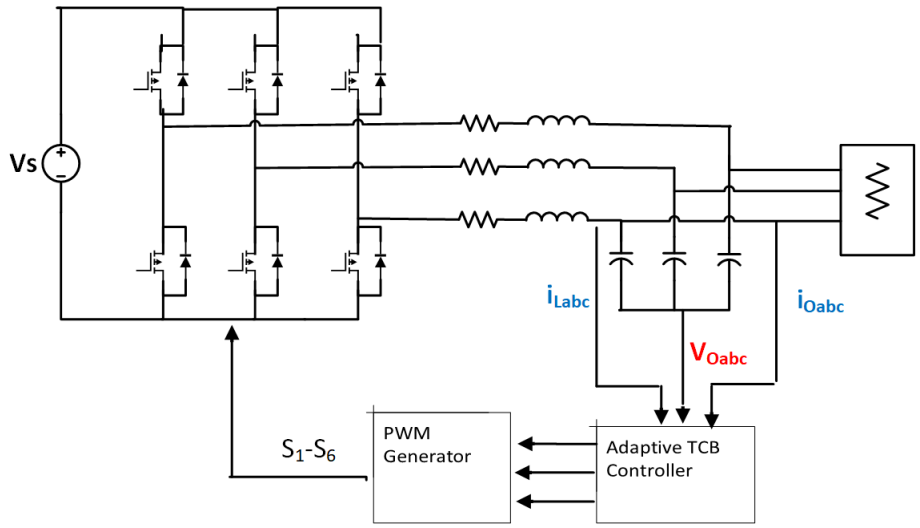

Fig. 4.2 Proposed diagram of the TCB-based control system for the inverter.

The output voltage response is shown in Fig. 4.3. As seen from the figure, there is no steady-state error and the recovery time is around 10 ms on average for each step change.

Similarly, the load current variation is shown in Fig. 4.4. With each step change, the load current doubles.

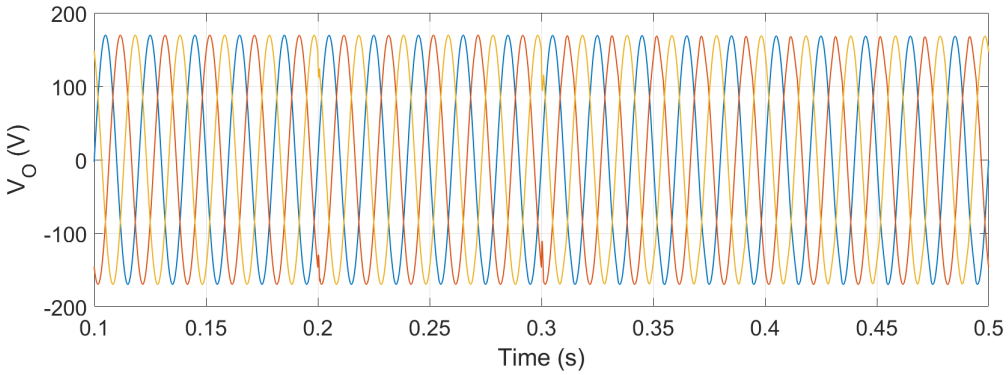

Fig. 4.3 Output voltage response under linear load variations.

The Total Harmonic Distortion of the output voltage was calculated under different load conditions. The THD% generally goes down as the value of load increases.

Furthermore, to evaluate the robustness of our controller against changes in input voltage, we reduced the input voltage from 350 V to 450 V and then restored it to the nominal value. The resulting output voltage is illustrated in Fig. 4.5(a), while

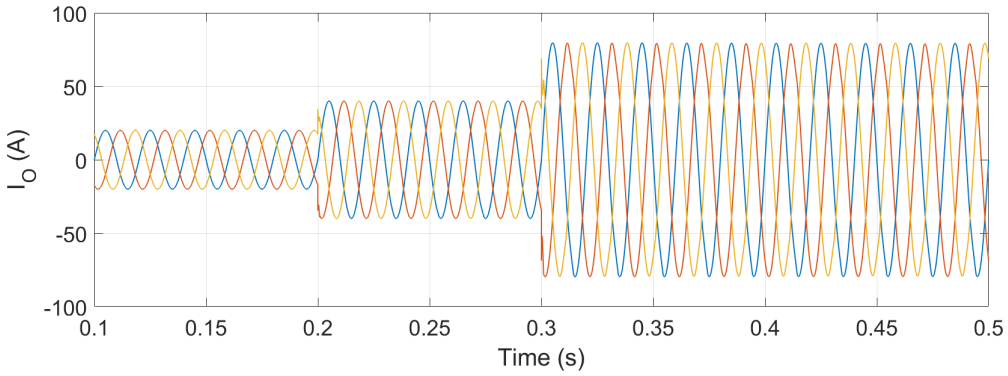

Fig. 4.4 Load current response under linear load variations.

Fig. 4.5(b) shows the reference variation in V_S. The output voltage response of the inverter exhibited a negligible steady-state error.

The controller performance was subsequently evaluated under unbalanced load conditions. In this test, phase c was disconnected at precisely 0.3 seconds. The resulting output voltage and load current are depicted in Fig. 4.6(a). As shown in Fig. 4.6(b), the current drops to zero at $t = 0.3$ s, but Fig. 4.6(a) demonstrates that this fault does not affect the phase voltage.

Lastly, a strong control system accounts for parametric uncertainties. Therefore, the LC parameter values have been adjusted to range from 50% to 200% of their nominal values. Fig. 4.7 shows the output voltage under different percentage changes of parametric uncertainties. Fig. 4.7(a) shows the output voltage when both inductor and capacitor are at 50% of their nominal values. Fig. 4.7(b) and Fig. 4.7(c) shows that when the value of inductor and capacitor are increased beyond the nominal values, the voltage waveforms get better. This is reflected in the THD% values. The THD% is lowest for LC parameter reduced to 50% values and is 2.65%. With LC parameters increased to 200% and 400%, THD reduces to 0.5% and 0.2% respectively.

4.4.2 Nonlinear Load

The nonlinear load designed to test the control system is illustrated in Fig. 5.7. This setup consists of a three-phase diode rectifier, a capacitor C_d, and inductors L_d

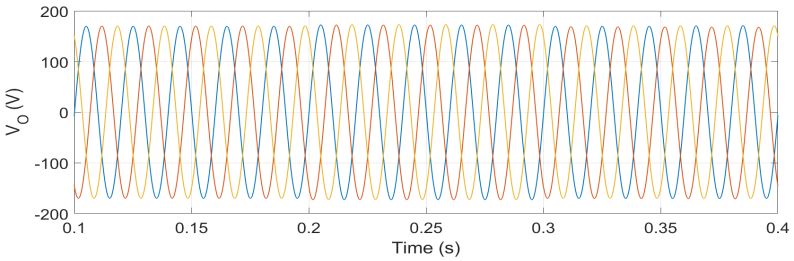

(a)

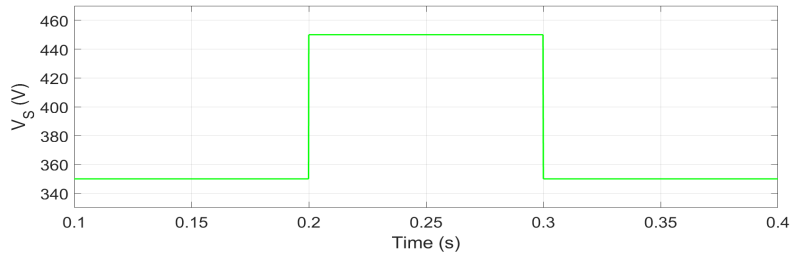

(b)

Fig. 4.5 (a) Output voltage and (b) Input voltage variations

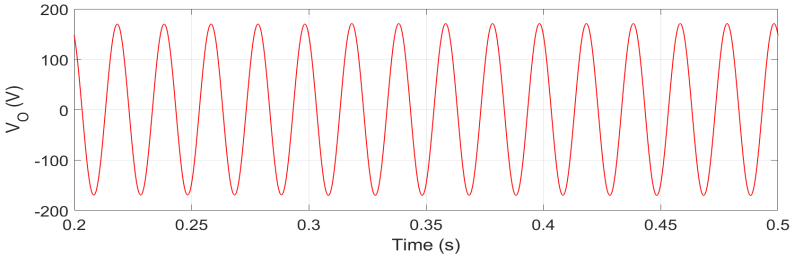

(a)

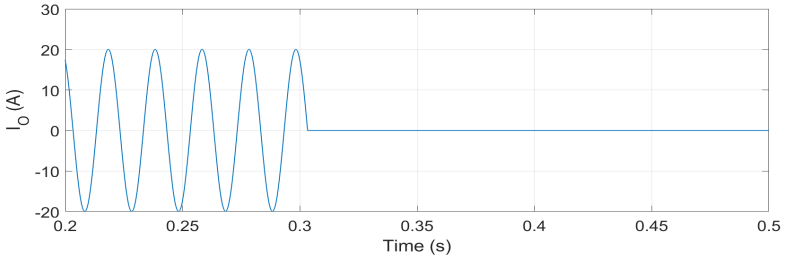

(b)

Fig. 4.6 (a) Output voltage and (b) Load current under phase fault condition.

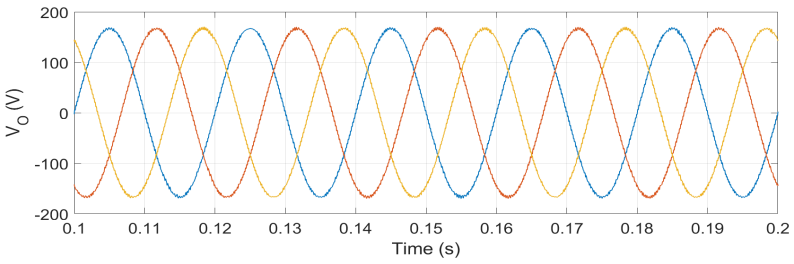

(a)

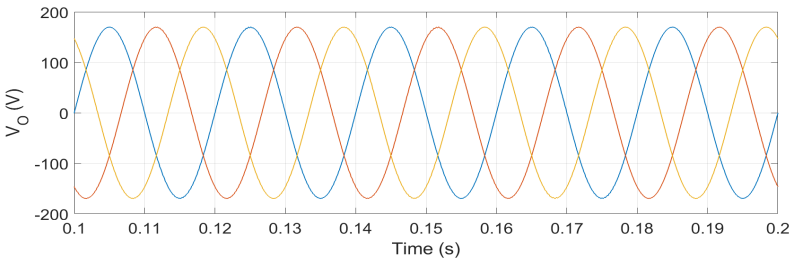

(b)

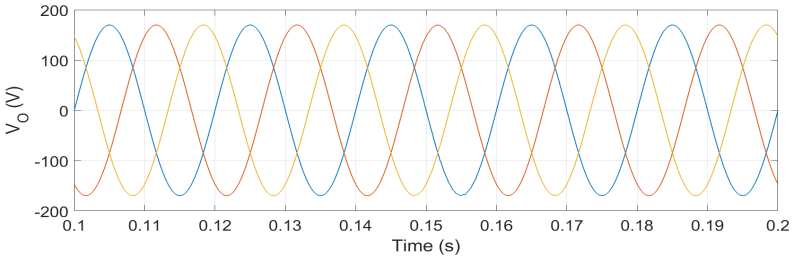

(c)

Fig. 4.7 Output voltage under (a) 50% of nominal values (b) 200% of nominal values (c) 400% of nominal values.

along with a load. The inductance and capacitance values are 10 mH and 10 μF, respectively.

Fig. 5.8 shows the output voltage and current response. Even under these nonlinear load conditions, the THD% is only 1.31%. This is well below the 8% limit specified by the IEEE Std 519-2014 standard.

The relationship of THD% with load is inversely proportional to load. As load increases, the THD% keep decreasing. But even under low load conditions, the overall THD% remains well within the standard limit. The total harmonic distortion is shown in Fig. 4.10 shows the THD% graph from the simulation.

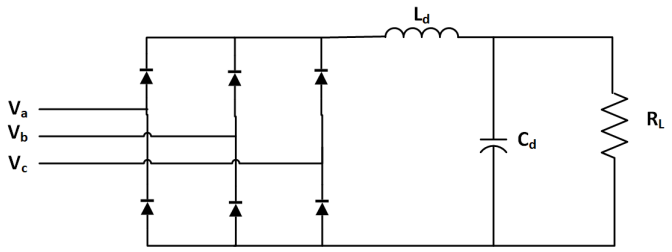

Fig. 4.8 Three-phase diode rectifier based nonlinear load.

4.4.3 Comparison with Nonlinear Controllers Proposed in the Literature

In this section we present a comparison of our controller with a Lyapunov Energy (LE) function controller proposed in [108] for three-phase active filter. The performance of LE controller was evaluated for various linear and nonlinear load. The output voltage shows a THD% of around 1% for linear loads and a THD% of 3.46% for nonlinear load. For the TCB controller, the THD% remains less than 0.40 % for linear loads and less than 1.31% for nonlinear load.

This comparison is shown in Fig. 4.11 and in Fig. 4.12 for nonlinear loads. The steady-state errors for both controllers are negligible.

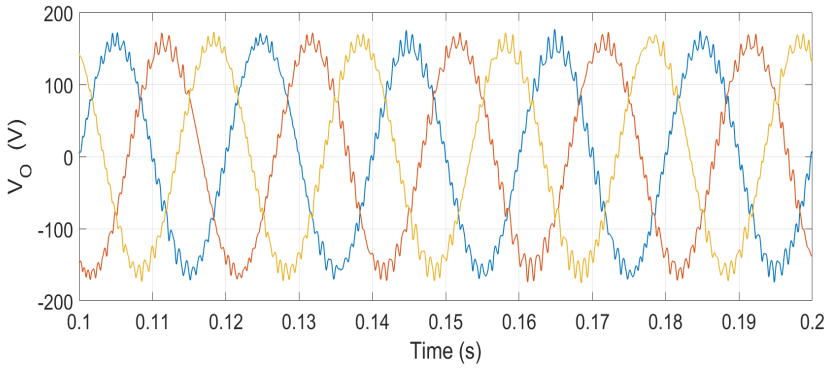

(a)

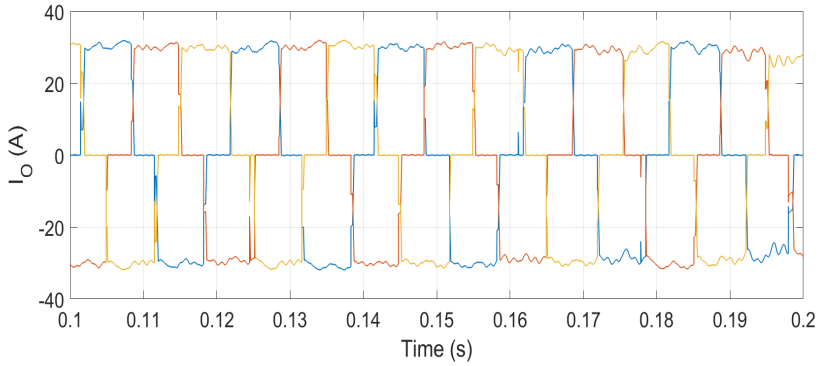

(b)

Fig. 4.9 (a) Output voltage and (b) Load current under nonlinear load.

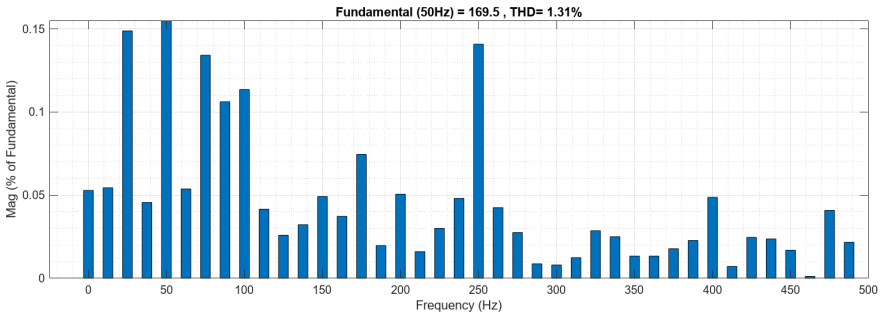

Fig. 4.10 THD% for nonlinear load

4.5 Concluding Remarks

This chapter has introduced a TCB-based adaptive control method for a UPS inverter. The proposed control architecture ensures global stability of the closed-loop system for both linear and nonlinear loads. It achieves low steady-state errors and low total harmonic distortion under various linear and nonlinear load conditions. As the load increases, THD% decreases to negligible levels. The robustness of this approach is also demonstrated by maintaining low steady-state errors and low THD% even with significant variations in inductor and capacitor parameters. Furthermore, comparison with another Lyapunov-based control techniques has also been shown highlighting the better performance of the TCB-based controller.

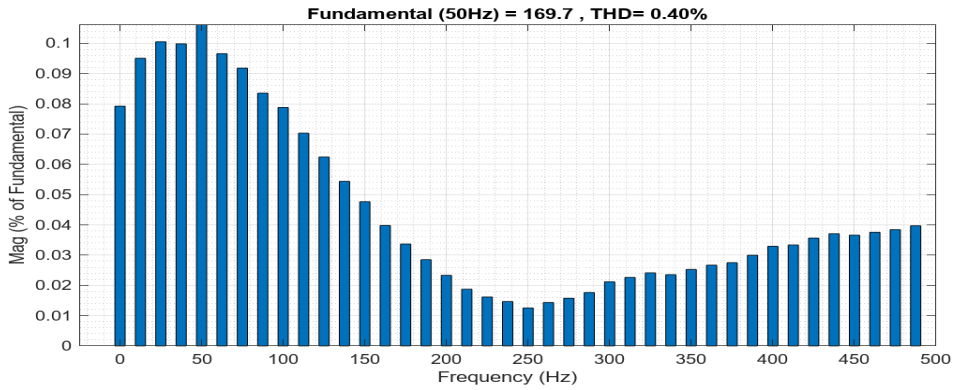

(a)

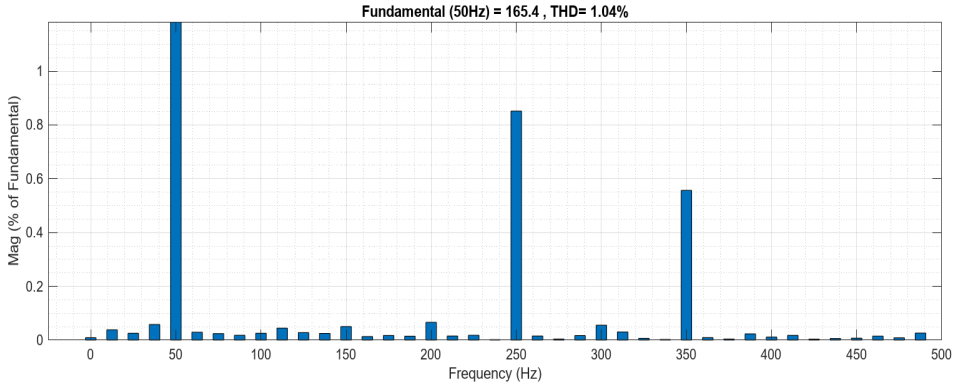

(b)

Fig. 4.11 THD% of (a) TCB-based control system (b) LE controller for linear loads.

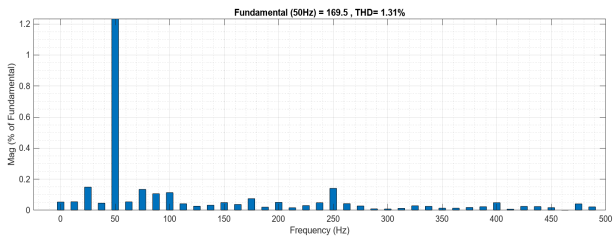

(a)

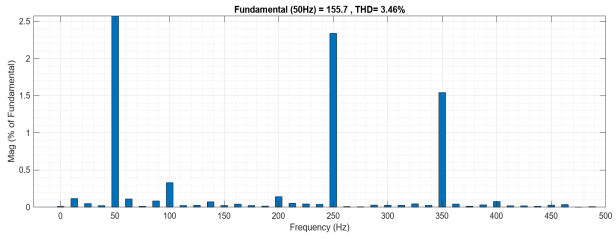

(b)

Fig. 4.12 THD% of (a) TCB-based control system (b) LE controller for nonlinear loads.

Chapter 5

Application of an Observer-based Adaptive Control Approach for Three-phase Grid-forming Inverters

Microgrids have an ever growing share in today's power generation and have become an essential part of our energy infrastructure today. These microgrids enable us to use renewable energy resources such as Photovoltaic (PV) arrays and wind turbines by interfacing them with the grid using inverter-based power electronic systems. Traditionally, these inverters operate in the grid-following mode, in which they rely on and operate in synchronization with the main grid. However, as the presence of inverter-based renewable resources continue to increase, there is an ever growing need for them to act as primary power sources autonomously.

Grid-forming (GFM) inverters have the ability to act independently of the main grid and establish and maintain fixed frequency and voltage within the technical limits. The GFM inverters are capable of stable and reliable power conversion. In fact, because of their fast response and enhanced controllability, studies have shown that they are capable of regulating the grid voltage and frequency even more effectively than synchronous machines [109]. Furthermore, they have additional advantages compared to grid-following inverters such as the ability to provide black-start capabilities in case of main grid outages [110].

All these capabilities of the GFM inverters are, however, dependent on the effectiveness of the controller implemented for these three-phase inverter topologies.

Thus the control design of GFM inverters has been an intense area of research in recent years. The main aim is to design a robust control structure that can tackle instabilities caused by the transient conditions in the grid while providing a fast dynamic response.

Various GFM control methodologies have been proposed in the literature. The GFM control methods can be broadly categorized as direct and indirect. The indirect method is popular in literature because it is easier to design and apply. In this method, the regulation of inverter is done using a dual-loop structure composed of linear controllers [111, 112]. The inner loop is responsible for regulating the current while the outer loop controls the output voltage and frequency. The issue with this type of control is that the dual loop architecture tends to underperform when the output frequency fluctuates. It shows imbalance during transient and steady-state operations. This is because a dual-loop setup necessitates the outer voltage loop to possess a considerably lower bandwidth than the inner current loops. Consequently, there exists a built-in bandwidth constraint that adversely affect the regulation of higher-level regulation components [109, 113].

In comparison, in the direct method a single loop is used that enables the regulation of output voltage and frequency. This is important because for a GFM inverter operating in a microgrid, the voltage control is more important and has higher priority than the current control [114]. For this case, the load determines the value of current directly which is free to change as long as it stays below the overcurrent limit.

For the design of the controller, it is important to note that since the transients faced by the inverter system are often nonlinear in nature, overcoming their impact on the system often requires taking those nonlinearities into account. In light of this, the optimal design for controllers in these systems is naturally inclined towards nonlinear control strategies, which are intrinsically equipped to manage the system's nonlinear characteristics.

Different nonlinear control methodologies have been proposed in the literature for the regulation of three-phase inverters. One nonlinear methodology is based on the use of Model Predictive Control (MPC). An MPC is able to optimize control actions, taking into consideration system constraints, over a finite time horizon. However, the issue with the traditional MPC approach is that there is a tradeoff between performance and computational complexity especially when facing higher

order dynamics. Thus, there are performance limitations when it comes to their implementation in three-phase inverters [100, 110].

Another nonlinear methodology proposed for the regulation of three-phase inverters is the sliding-mode control. This technique is valued for its simplicity and robustness against disturbances and uncertainties in modeling. SMC has been predominantly used in a cascaded topology for the regulation of current in the inner loop [115, 116]. In [117], a variant of above methodology that uses an integral SMC current controller with an extended surface is proposed. Another innovative approach integrates predictive and sliding controllers, as proposed in [118]. Few studies have also adopted SMC for direct voltage control. An SMC augmented with fuzzy logic for a single phase uninterruptible power system has been proposed in [119]. Recently, it has been utilized in a direct control method where the SMC has been used together with an equivalent PD control to provide active damping and load rejection capabilities [114].

In this part of the research, we propose an observer-based adaptive control strategy using the TCB methodology for the regulation of a three-phase GFM inverter. An adaptive observer design is used to estimate the load resistance to avoid the use of load current sensors. In this application, our aim is to use the TCB control approach to tackle the issue of three-phase inverters for GFM purposes. The performance of our control approach is also compared against other linear [120] and nonlinear controllers [121], [122], [114] and remarks on the performance are made.

This chapter is organized as follows. Section 5.1 shows the mathematical modelling of the three-phase inverter that is used for the design of the controller. The application of this approach on the three-phase inverter and the design of observer is shown in section 5.2 and the simulation results are shown in Section 5.3. Finally, the concluding remarks are drawn in Section 5.4.

5.1 Three-phase Inverter Modeling

Fig. 5.1 depicts a three-phase inverter with LC filter. The mathematical model in the synchronously rotating dq frame is expressed as follows:

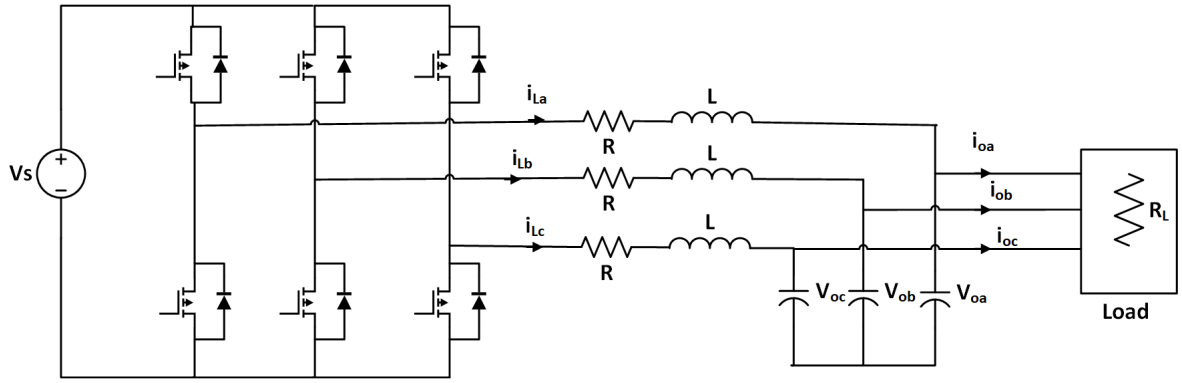

Fig. 5.1 Three-phase inverter with LC filter

$$\begin{cases} \dot{x}_1 &= \frac{1}{L}(\frac{\mu_d V_s}{2} - Rx_1 - x_3 + \omega L x_2) \\ \dot{x}_2 &= \frac{1}{L}(\frac{\mu_q V_s}{2} - Rx_2 - x_4 - \omega L x_1) \\ \dot{x}_3 &= \frac{1}{C}(x_1 - i_{od} + \omega C x_4) \\ \dot{x}_4 &= \frac{1}{C}(x_2 - i_{oq} - \omega C x_3) \end{cases} \tag{5.1}$$

where x_1, x_2 are the the three-phase inductor current expressed in the dq frame, i.e., i_{Ld} and i_{Lq}, while x_3 and x_4 are output voltages v_{od} and v_{oq}, respectively. Similarly, u_d and u_q are the dq representation of three-phase duty cycle. L, C, R and are the inductance, capacitance, and inductor resistance values of the converters, respectively. Moreover, ω is the angular frequency and i_{od} and i_{oq} are the load currents in the dq domain, and the load is represented by R_L.

5.2 Application of an Observer based MRAC-TCB Approach to a Three-phase Voltage-controlled Inverter

5.2.1 Adaptive State Observer Design for the Three-phase Inverter

The general application of the MRAC-TCB approach can be seen in [20],[18]. However, for this application, a state observer is used to estimate the unknown load

resistance under dynamic conditions. The use of state observers to estimate load has previously been used for DC-DC Boost converters in [123],[124].

For the design of the observer, both inductor current and output voltage are considered accessible. The observer is designed to estimate the value of the unknown load resistance R_L. Considering $1/R_L$ as θ, the following estimator equations can be written for the three-phase observer.

$$\begin{cases} \dot{\hat{x}}_1 &= \frac{1}{L}(\frac{\mu_d V_s}{2} - R\hat{x}_1 - \hat{x}_3 + \omega L\hat{x}_2) + K_1(x_1 - \hat{x}_1) \\ \dot{\hat{x}}_2 &= \frac{1}{L}(\frac{\mu_q V_s}{2} - R\hat{x}_2 - \hat{x}_4 - \omega L\hat{x}_1 + K_2(x_2 - \hat{x}_2) \\ \dot{\hat{x}}_3 &= \frac{1}{C}(\hat{x}_1 - x_3\hat{\theta} + \omega C\hat{x}_4) + K_3(x_3 - \hat{x}_3) \\ \dot{\hat{x}}_4 &= \frac{1}{C}(\hat{x}_2 - x_4\hat{\theta} - \omega C\hat{x}_3) + K_4(x_4 - \hat{x}_4) \end{cases} \tag{5.2}$$

where $\hat{x}_1$, $\hat{x}_2$,$\hat{x}_3$ and $\hat{x}_4$ are the estimates of their respective state variables and K_1 to K_4 are observer gains. $\hat{\theta}$ is the estimate of θ.

Next step is to design an adaptation law for $\hat{\theta}$. Let's start by defining the following state error terms:

$$\begin{cases} \tilde{x}_1 = x_1 - \hat{x}_1 \\ \tilde{x}_2 = x_2 - \hat{x}_2 \\ \tilde{x}_3 = x_3 - \hat{x}_3 \\ \tilde{x}_4 = x_4 - \hat{x}_4 \end{cases} \tag{5.3}$$

Using the equations (4.2) and (5.2), we get the following formulation:

$$\begin{cases} \dot{\tilde{x}}_1 &= \frac{1}{L}(-R\tilde{x}_1 - \tilde{x}_3 + \omega L\tilde{x}_2) - K_1\tilde{x}_1 \\ \dot{\tilde{x}}_2 &= \frac{1}{L}(-R\tilde{x}_2 - \tilde{x}_4 - \omega L\tilde{x}_1) - K_2\tilde{x}_2 \\ \dot{\tilde{x}}_3 &= \frac{1}{C}(\tilde{x}_1 - x_3\tilde{\theta} + \omega C\tilde{x}_4) - K_3\tilde{x}_3 \\ \dot{\tilde{x}}_4 &= \frac{1}{C}(\tilde{x}_2 - x_4\tilde{\theta} - \omega C\tilde{x}_3) - K_4\tilde{x}_4 \end{cases} \tag{5.4}$$

To find the adaptive law for $\hat{\theta}$, we consider the following Lyapunov function:

$$V = \frac{1}{2}L\tilde{x}_1^2 + \frac{1}{2}L\tilde{x}_2^2 + \frac{1}{2}C\tilde{x}_3^2 + \frac{1}{2}C\tilde{x}_4^2 + \frac{1}{2}\gamma\tilde{\theta}^2 \tag{5.5}$$

where γ is a design parameter. The time derivative of the Lyapunov function can be found as follows:

$$\dot{V} = -K_1\tilde{x}_1^2 - K_2\tilde{x}_2^2 - K_3\tilde{x}_3^2 - K_4\tilde{x}_4^2 + \tilde{\theta}(-\tilde{x}_3 x_3 - \tilde{x}_4 x_4 + \gamma\,\dot{\tilde{\theta}}) + f(x,\tilde{x}) \tag{5.6}$$

The adaptation law for $\tilde{\theta}$ can be determined by the following equation:

$$\dot{\hat{\theta}} = -\gamma(x_3\tilde{x}_3 + x_4\tilde{x}_4) \tag{5.7}$$

The function $f(x,\tilde{x})$ is such that when the adaptive TCB control law derives the state variables x to $\hat{x}$, the function goes to zero and hence we have a negative-definite Lyapunov function.

5.2.2 MRAC-TCB Design

As mentioned in the previous section, the MRAC-TCB approach is implemented through three distinct steps.

Initially, in the first step, the reference signal is generated to regulate the output of the converter. This reference signal in our case is the desired value of v_{od} and v_{oq} and are denoted as y_{od} and y_{oq}. The state variable vector **x** is composed of x_1, x_2,x_3, and x_4, the control variable vector **u** is u_d,u_q, and the algebraic variable **y** is y_{od}, y_{oq}.

Subsequently, the second step involves determining the coordinates of the equilibrium point within the composite domain (**x**, **u**), indicated as (**x***, **u***). To achieve this, the equilibrium point for steady-state values is derived by setting Equation (5.1) to zero. But due to the adaptive design in which the load resistance is determined using the observer, we redefine the load resistance R_L in terms of $\hat{\theta}$, resulting in the following equations:

$$\begin{cases} x_1^* = y_{od}\hat{\theta} \\ x_2^* = y_{oq}\hat{\theta} + Cy_{od}\omega \\ u_d^* = \frac{2}{V_s}(-CLy_{od}\omega^2 - Ly_{oq}\hat{\theta}\omega + Ry_{od}\hat{\theta} + y_{od}) \\ u_q^* = \frac{2}{V_s}(Ry_{oq}\hat{\theta} + Ly_{od}\hat{\theta}\omega + CRy_{od}\omega) \end{cases} \tag{5.8}$$

The third step is to design the adaptation mechanism for the minimization of the following tracking errors:

$$\begin{cases} e_1 = \alpha_1(x_1 - x_1^*) \\ e_2 = \alpha_1(x_2 - x_2^*) \\ e_3 = \alpha_2(x_3 - x_3^*) \\ e_4 = \alpha_2(x_4 - x_4^*) \\ e_5 = \beta(u_d - u_d^*) \\ e_6 = \beta(u_q - u_q^*) \end{cases} \tag{5.9}$$

The weight vectors α_1, α_2, and β are determined empirically to adjust the response of the system. Again, using the expression defined in Equation (1.37) and the error vector mentioned above, the control equation for u_d and u_q becomes:

$$\dot{u}_d = -K\Big[\alpha_1^2\frac{de_1}{du_d}e_1 + \alpha_1^2\frac{de_2}{du_d}e_2 + \alpha_2^2\frac{de_3}{du_d}e_3 + \alpha_2^2\frac{de_4}{du_d}e_4 + \beta^2\frac{de_5}{du_d}e_5 + \beta^2\frac{de_6}{du_d}e_6\Big] \tag{5.10}$$

$$\dot{u}_q = -K\Big[\alpha_1^2\frac{de_1}{du_q}e_1 + \alpha_1^2\frac{de_2}{du_q}e_2 + \alpha_2^2\frac{de_3}{du_q}e_3 + \alpha_2^2\frac{de_4}{du_q}e_4 + \beta^2\frac{de_5}{du_q}e_5 + \beta^2\frac{de_6}{du_q}e_6\Big] \tag{5.11}$$

where K is the gain factor with a constant value given in Table 5.2.

The derivatives of the error equations in (5.9) with respect to u_d are given by following equations:

$$\begin{cases} \frac{de_1}{du_d} = \alpha_1(\hat{y}_1 - y_{od}\frac{d\hat{\theta}}{du_d}) \\ \frac{de_2}{du_d} = \alpha_1(\hat{y}_2 - y_{oq}\frac{d\hat{\theta}}{du_d}) \\ \frac{de_3}{du_d} = \alpha_2\hat{y}_3 \\ \frac{de_4}{du_d} = \alpha_2\hat{y}_4 \\ \frac{de_5}{du_d} = \beta(\frac{2}{V_s}(Ly_{oq}\omega\frac{d\hat{\theta}}{du_d} - Ry_{od}\frac{d\hat{\theta}}{du_d}) + 1) \\ \frac{de_6}{du_d} = \beta(\frac{-2}{V_s}(Ry_{oq}\frac{d\hat{\theta}}{du_d} + Ly_{od}\omega\frac{d\hat{\theta}}{du_d})) \end{cases} \tag{5.12}$$

where $\hat{y}$ is a sensitivity parameter representing $\frac{d\hat{\mathbf{x}}}{du_d}$. $\hat{\mathbf{y}}$ can be calculated from (5.2) by the following set of equations:

$$\begin{cases} \dot{\hat{y}}_1 &= \frac{1}{L}(\frac{V_s}{2} - R\hat{y}_1 - \hat{y}_3 + \omega L\hat{y}_2) + K_1(y_1 - \hat{y_1}) \\ \dot{\hat{y}}_2 &= \frac{1}{L}(-R\hat{y}_2 - \hat{y}_4 - \omega L\hat{y}_1) + K_2(y_2 - \hat{y}_2) \\ \dot{\hat{y}}_3 &= \frac{1}{C}(\hat{y}_1 - y_3\hat{\theta} + \omega C\hat{y}_4) + K_3(y_3 - \hat{y}_3) \\ \dot{\hat{y}}_4 &= \frac{1}{C}(\hat{y}_2 - y_4\hat{\theta} - \omega C\hat{y}_3) + K_4(y_4 - \hat{y}_4) \end{cases} \tag{5.13}$$

The sensitivity parameter $\mathbf{y}$ representing $\frac{d\mathbf{x}}{du_d}$ can be derived by the following equations:

$$\begin{cases} \dot{y}_1 &= \frac{1}{L}(\frac{V_s}{2} - Ry_1 - y_3 + \omega Ly_2) \\ \dot{y}_2 &= \frac{1}{L}(-Ry_2 - y_4 - \omega Ly_1) \\ \dot{y}_3 &= \frac{1}{C}(y_1 - y_3/R_L + \omega Cy_4) \\ \dot{y}_4 &= \frac{1}{C}(y_2 - y_4/R_L - \omega Cy_3) \end{cases} \tag{5.14}$$

For the derivation of $\frac{d\hat{\theta}}{du_d}$ we use equation (5.7). We get:

$$\frac{d\hat{\theta}}{du_d} = -\gamma(y_3\tilde{x}_3 + \tilde{y}_3x_3 + y_4\tilde{x}_4 + \tilde{y}_4x_4) \tag{5.15}$$

Similarly, for the derivation of equations for the q-domain, we need to repeat the above procedure.

Again, by taking the derivatives of (5.9) with respect to u_q we obtain the following equations:

$$\begin{cases} \frac{de_1}{du_q} = \alpha_1(\hat{z}_1 - y_{oq}\frac{d\hat{\theta}}{du_q}) \\ \frac{de_2}{du_q} = \alpha_1(\hat{z}_2 - y_{oq}\frac{d\hat{\theta}}{du_q}) \\ \frac{de_3}{du_q} = \alpha_2\hat{z}_3 \\ \frac{de_4}{du_q} = \alpha_2\hat{z}_4 \\ \frac{de_5}{du_q} = \beta(\frac{2}{V_s}(Ly_{oq}\omega\frac{d\hat{\theta}}{du_q} - Ry_{od}\frac{d\hat{\theta}}{du_q})) \\ \frac{de_6}{du_q} = \beta(1 - \frac{2}{V_s}(Ry_{oq}\frac{d\hat{\theta}}{du_q} + Ly_{od}\omega\frac{d\hat{\theta}}{du_q})) \end{cases} \tag{5.16}$$

For the sensitivity parameter $\hat{z_1}$, again we can use Equation (5.2) and find its derivative against u_q. We get the following equations:

$$\begin{cases} \dot{\hat{z}}_1 &= \frac{1}{L}(-R\hat{z}_1 - \hat{z}_3 + \omega L\hat{z}_2) + K_1(z_1 - \hat{z_1}) \\ \dot{\hat{z}}_2 &= \frac{1}{L}(\frac{V_s}{2} - R\hat{z}_2 - \hat{z}_4 - \omega L\hat{z}_1) + K_2(z_2 - \hat{z}_2) \\ \dot{\hat{z}}_3 &= \frac{1}{C}(\hat{z}_1 - z_3\hat{\theta} + \omega C\hat{z}_4) + K_3(z_3 - \hat{z}_3) \\ \dot{\hat{z}}_4 &= \frac{1}{C}(\hat{z}_2 - z_4\hat{\theta} - \omega C\hat{z}_3) + K_4(z_4 - \hat{z}_4) \end{cases} \tag{5.17}$$

The sensitivity parameter $\mathbf{z}$ representing $\frac{d\mathbf{x}}{du_q}$ can be derived by the following equations:

$$\begin{cases} \dot{z}_1 &= \frac{1}{L}(-Rz_1 - z_3 + \omega Lz_2) \\ \dot{z}_2 &= \frac{1}{L}(\frac{V_s}{2} - Rz_2 - z_4 - \omega Lz_1) \\ \dot{z}_3 &= \frac{1}{C}(z_1 - z_3/R_L + \omega Cz_4) \\ \dot{z}_4 &= \frac{1}{C}(z_2 - z_4/R_L - \omega Cz_3) \end{cases} \tag{5.18}$$

For the derivation of $\frac{d\hat{\theta}}{du_1}$ we again use Equation (5.7). We get:

$$\frac{d\hat{\theta}}{du_q} = -\gamma(z_3\tilde{x}_3 + \tilde{z}_3x_3 + z_4\tilde{x}_4 + \tilde{z}_4x_4) \tag{5.19}$$

5.3 Simulation and Experimental Results

This section presents the simulation results of the proposed control approach. The parameters used for three-phase inverter are shown in Table 5.1. The control gains for the TCB controller and the load observer are shown in Table 5.2. The simulations are performed in the Matlab/Simulink environment.

Fig. 5.2 shows the block diagram of our observer-based TCB control system. As shown in the figure, we only need sensors to measure inductor currents (shown in blue) and capacitor voltages (shown in red). These values are transformed from the abc domain to the dq domain using the Park transformation. The resulting values of V_{Odq} and I_{Ldq} are then used by the load observer to estimate load resistor values. Finally, the adaptive TCB controller uses these values to generate μ_d and μ_q. These

Table 5.1 Specifications of the Three-phase Inverter

Description of parameters	Nominal value
Input voltage, V_S	650 V
Reference output voltage, V_{Oref}	320 V
Capacitance, C	25 uF
Inductance, L	6 mH
Inductor Resistance, R	0.1 Ω
Switching frequency, f_s	10 kHz

Table 5.2 Controller Gains and Observer Gains

Description of parameters	Nominal value
Controller Gain, K	6000
α_1	0.25
α_2	0.080
β	4.0
γ	0.35
k_1	1.25 x 10^3
k_2	1.25 x 10^3
k_3	1.75 x 10^4
k_4	1.75 x 10^4

values are used to derive the six switches S_1 to S_6 after inverse Park transformation to convert μ_d and μ_q to μ_{abc} domain.

The aim is to test our controller's robustness and adaptivity under different scenarios. The first section shows the results when control system is tested with linear (resistive) load while the second section shows the response with nonlinear loads. The final section shows the comparison of the proposed system with a Sliding Mode Direct Voltage controller proposed in the literature [114].

5.3.1 Linear Load

Fig. 5.3 shows the output voltage when the load is successively halved from R_L = 80 Ω to 2.5 Ω at every 0.1 s interval. The steady-state error remains negligible throughout the various load value variations. On average the recovery time is around 20 ms for each step change.

The corresponding $\hat{\theta}$ calculated by the observer is shown in Fig. 5.4(a). Similarly, the load current variation is shown in Fig. 5.4(b).

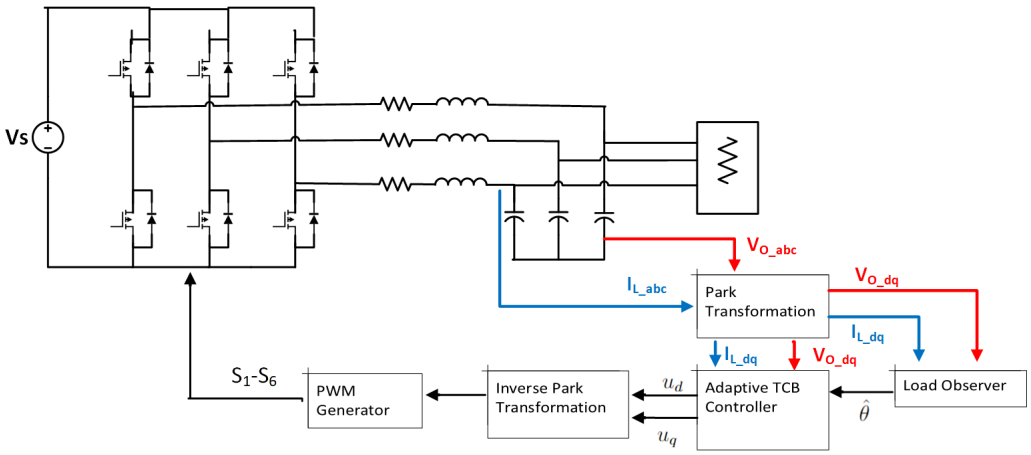

Fig. 5.2 Proposed diagram of the observer-based TCB adaptive control system.

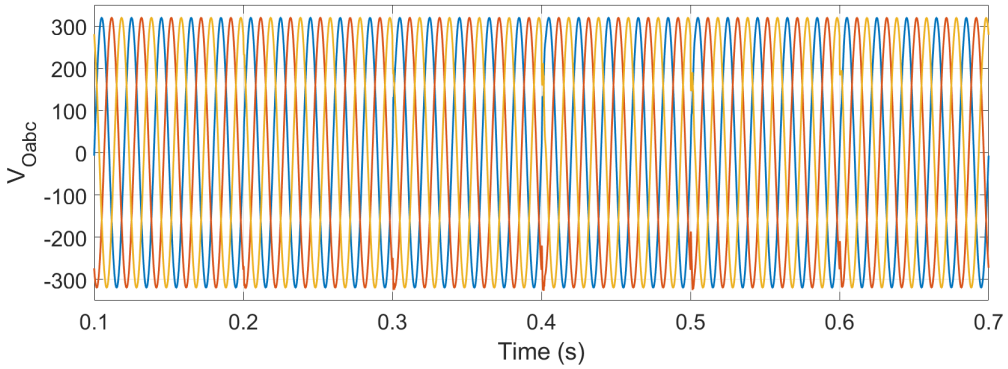

Fig. 5.3 Output voltage response under linear load variations.

Table 5.3 shows the Total Harmonic Distortion (THD) percentage at different values of load resistance. As seen from the table, THD% increases from 0.086% for $R_L = 2.5\ \Omega$ to 0.16% for $R_L = 80\ \Omega$.

To test the robustness of our controller under input voltage variations, the input voltage is stepped down from 650 V to 550 V and then stepped back to the nominal value. The resulting output voltage is shown in Fig. 5.5(a) and Fig. 5.5(b) is the reference variation in V_S. There was negligible steady-state error in the output voltage response of the inverter V.

The performance of the controller was next tested under unbalanced load conditions. For this test, phase c was opened at exactly 0.2 s. The corresponding output voltage and load current are shown in Fig. 5.6. Fig. 5.6(b) shows the current goes to

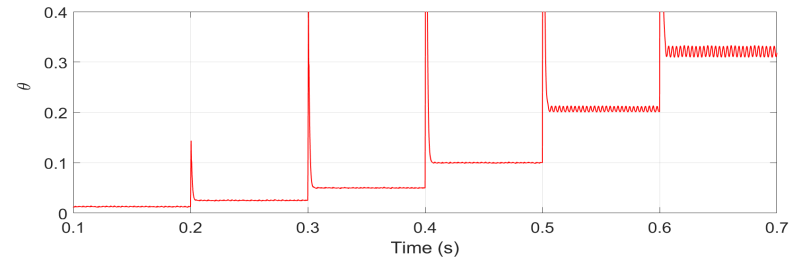

(a)

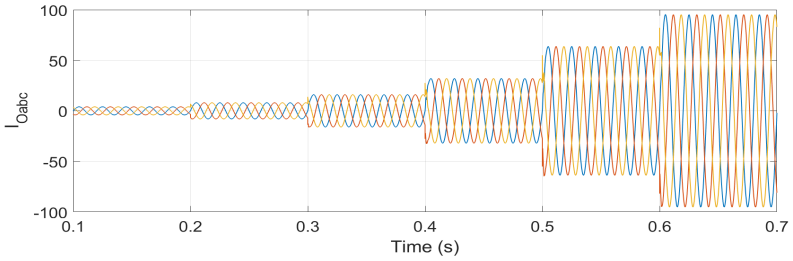

(b)

Fig. 5.4 (a) Observer output in response to load variations (b) Output current in response to load variations.

Table 5.3 THD% under Different Linear Load Conditions

Load Resistance R_L (Ω)	THD%
80	0.16
40	0.14
20	0.11
10	0.10
5	0.09
2.5	0.08

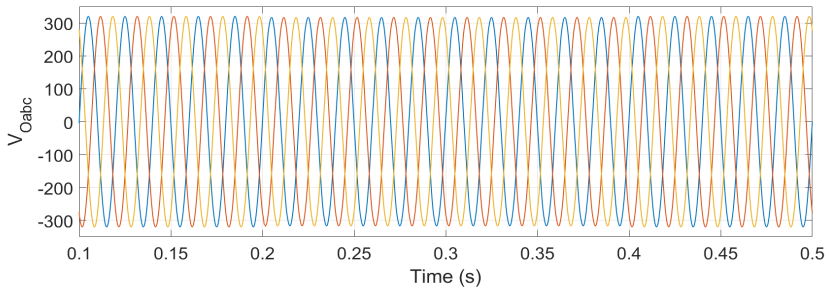

(a)

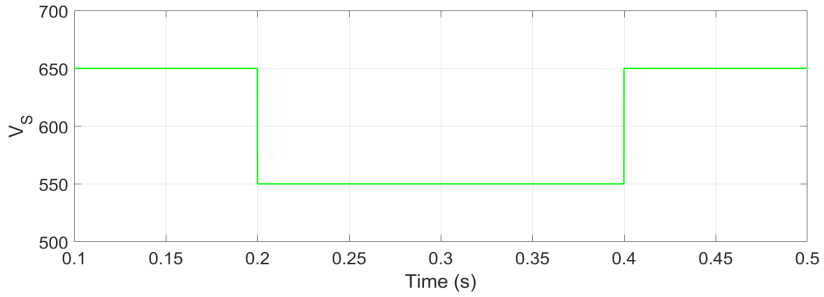

(b)

Fig. 5.5 (a) Output voltage and (b) Input voltage variations

zero at $t = 0.2$ s, but as it can be seen from Fig. 5.6(a) the fault has no bearing on the voltage of the phase.

Finally, a robust control system also has an allowance for parametric uncertainties. Hence, the values of LC parameters have been varied from 50% to 200% of nominal values. Table 5.4 shows the effects of parameter mismatch and its effects on THD%. As seen from the table, as value of both inductor and capacitor increases, the values of THD% decrease. In the harshest condition, i.e., L and C values 50% of their nominal values, we get the maximum THD% of 4.80%.

Table 5.4 THD% under Inductor and Capacitor Parameter Uncertainties

$C = 12.5\ \mu$F		$C = 25\ \mu$F		$C = 50\ \mu$F	
Inductance (mH)	THD%	Inductance (mH)	THD%	Inductance (mH)	THD%
3	4.80	3	1.45	3	0.11
6	0.26	6	0.10	6	0.07
12	0.14	12	0.07	12	0.05

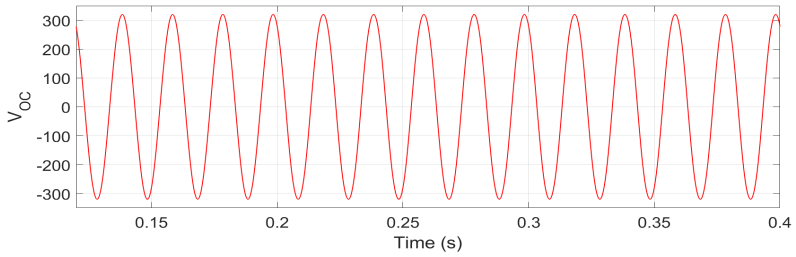

(a)

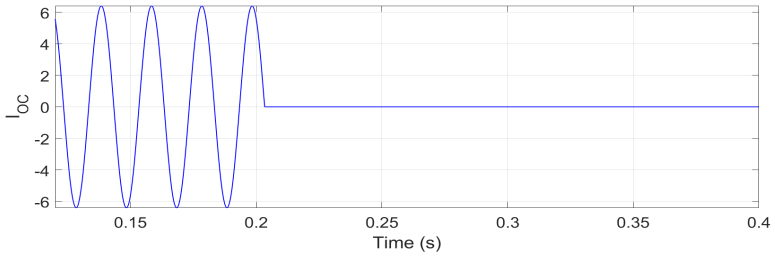

(b)

Fig. 5.6 (a) Output voltage and (b) Load current under phase fault condition

5.3.2 Nonlinear Load

The nonlinear load proposed for the testing of the control system is shown in Fig. 5.7. It is a three-phase diode rectifier with capacitor C_d and inductor L_d parameters and a load. The values of the inductor and capacitor parameters are 6.5 mH and 5 μF, respectively.

The output voltage and current under nonlinear load is shown in Fig. 5.8. As seen from Fig. 5.8(a), there is negligible steady-state error and while the output is not as smooth as in the case of linear load, the THD% is 1.86% (for load of 70 Ω). This is well below the 8% limit specified by the IEEE Std 519-2014 Standard.

The relationship of THD% with load is as shown in Table 5.5. As it can be seen from the table, the THD% decreases with an increase in load. But even under low load conditions, the overall THD% remains well within the standard limit.

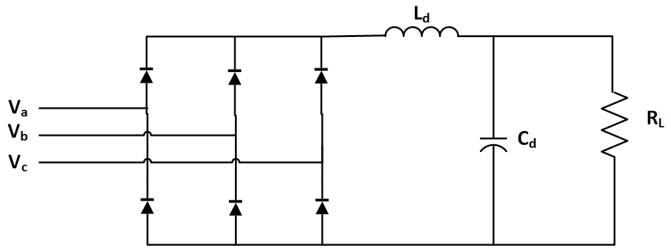

Fig. 5.7 Three-phase diode rectifier-based nonlinear load

Table 5.5 THD% under Different Nonlinear Load Conditions

Load Resistance R_L (Ω)	THD%
500	0.40
400	0.43
300	0.51
200	0.70
100	1.39
75	1.86
50	2.91

5.3.3 Comparison with Nonlinear Controllers Proposed in the Literature

In this section we present a comparison between the TCB-based controller and a Sliding Mode Direct Voltage controller (SMDVC) proposed in [114]. The performance of the SMDVC controller with three-phase diode bridge rectifier nonlinear load is shown in Fig. 5.9. As seen from the figure, the SMDVC controller has a smooth output with negligible steady-state error. Furthermore, the THD response of the SMDVC controller alongside our controller for load $R_L = 70\ \Omega$ is shown in Fig. 5.10. As seen from the figure, both controllers show little harmonic distortions. The 5^{th} and 7^{th} harmonics are present for both controller but their magnitude is mitigated. But overall, response of our controller (THD% of 1.83% as compared to 2.12%) shows a better response. The steady-state errors of both controllers are negligible.

As shown in Table 5.6, the TCB-based control system does not require the use of load sensors. Apart from the Model predictive controller proposed in [121] which also uses observers, the other reported control systems do use sensors for measuring load current. However, the MPC based controller does have a very

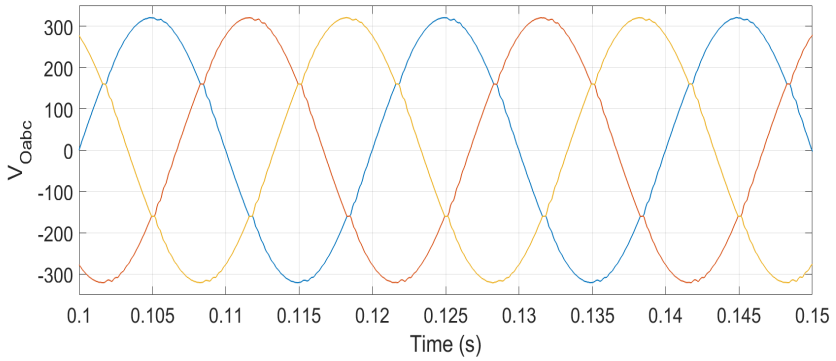

(a)

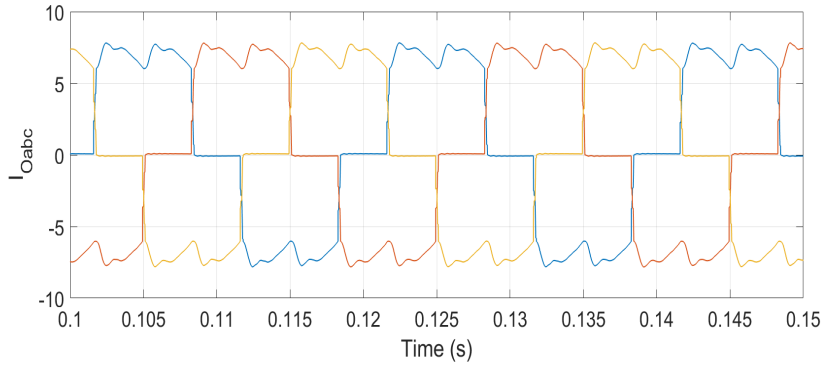

(b)

Fig. 5.8 (a) Output voltage and (b) Load current under nonlinear load

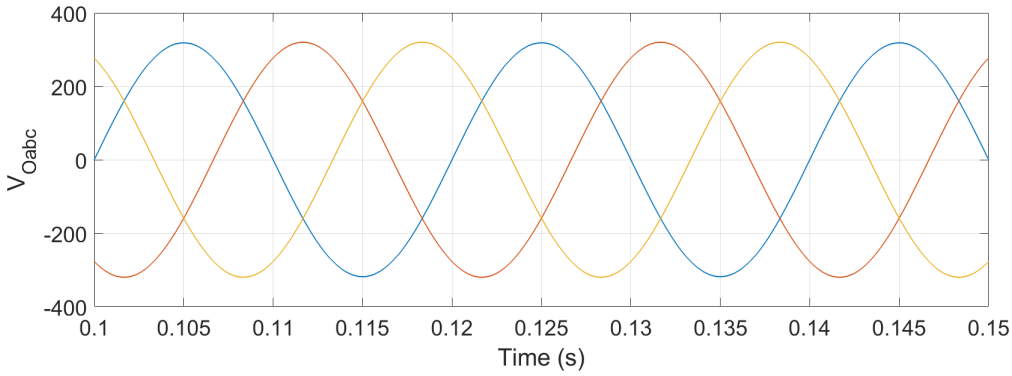

Fig. 5.9 Output voltage response of SMDVC under nonlinear load.

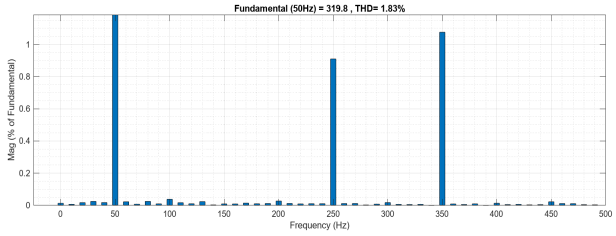

(a)

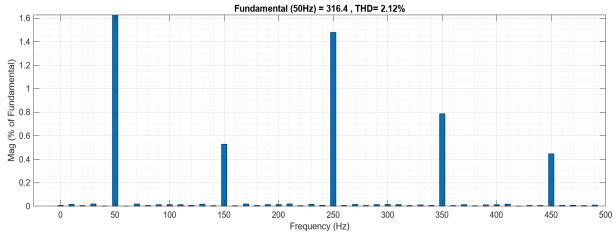

(b)

Fig. 5.10 THD of (a) TCB based control system (b) SMDVC controller

high computational burden and does not operate on constant frequency like other approaches.

The feedforward PI controller is simpler to implement in comparison with other proposed control techniques but it can only guarantee local stability around the operating point. Other Lyapunov based control approach and the SMDVC do offer robustness and low steady-state errors, but in case of [122] requires the use of additional current sensors. In SMDVC, while they do make use of sensors for measuring both inductor and load current, they do mitigate the overall cost by

Table 5.6 Comparison of the Proposed Control System with Control Schemes Proposed in the Literature.

References	[120]	[121]	[122]	[114]	This Thesis
Control Strategy	Feedforward PI control	FCS MPC control	Lyapunov function-based approach	SMDVC	TCB-based control
Large Signal Stability Guaranteed	No	Not reported	Yes	Yes	Yes
Load Current Sensors	3	0	3	3	0
Computational Burden	Low	Very High	Medium	Medium	Medium
Switching Frequency	Fixed	Varying	Fixed	Fixed	Fixed
THD%	0.48	2.31	1.046	0.19	0.16
Steady-state error %	0.123	3.629	1.046	Negligible	Negligible

designing observer for estimating output voltage. However, in practice, it is usually difficult to have access to load current information.

5.4 Concluding Remarks

In this chapter a TCB-based adaptive control approach for a grid-forming inverter has been proposed. An observer has also been designed to estimate the value of load to reduce the number of sensors required to implement the control system. The proposed control architecture guarantees global stability of the closed loop system for both linear and nonlinear loads. The proposed approach shows negligible steady-state errors and low THD% for various load conditions. As the load increases, the THD% decreases to negligible values. Furthermore, the robustness of the proposed approach can also be seen by varying LC parameters from the low steady-state errors and low THD% even under high inductor and capacitor parametric uncertainties.

Chapter 6

Real-time Simulation and Hardware Prototype of a MRAC-TCB based Three-phase Inverter

In order to test the validity of the proposed controller in real-time, a prototype of the control system applied to an existing three-phase inverter was built in the laboratory. Furthermore, simulations of a Grid-Forming Inverter were performed in Real-time simulator OPAL-RT 5700 using the RT-LAB software.

6.1 Validation of proposed control by Three-Phase Inverter Prototype setup

For practical and safety reasons, the inverter prototype was set up to operates at a smaller, more manageable scale. However, the underlying mechanisms of the inverter settings and control design remain the same. The setup built in the laboratory is shown in Fig. 6.1.

As shown in the figure, the setup consists of a three-phase IGBT switches being controlled using a microcontroller implemented in STM32 Cube IDE. The filter consists of inductors and capacitors connected in parallel. The input voltage as shown in the figure is given by connecting two voltage sources in series. Two pairs

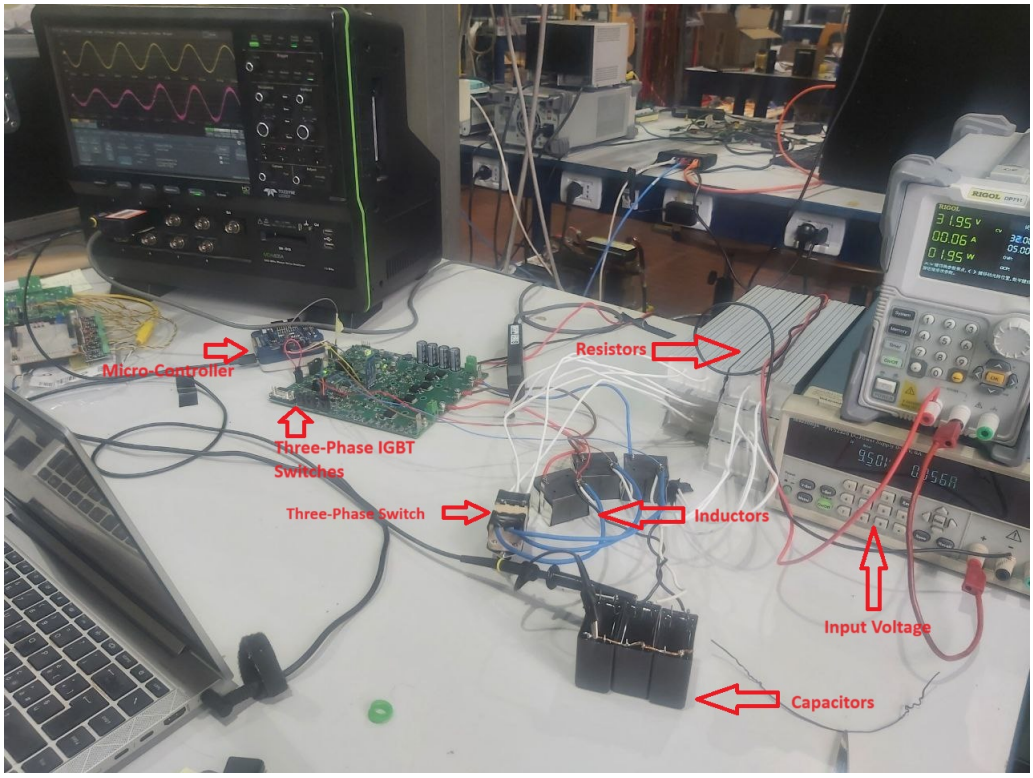

Fig. 6.1 Laboratory Setup.

of three resistors are used as load. They are connected in parallel through a switch that is turned on or off to test the performance of our controller in real-time.

The new parameter values are shown in Table 6.1. The input voltage is fixed at 40 V, for a desired output voltage of 24 V phase to phase. The inductors used are 100 μH each with a saturation current of 9 A. Three film capacitors of 20 μF each were used. Initially, the load was fixed at 3.3 Ω. To test the validity of the controller, the load was varied by connecting another pair of 3.3 Ω loads in parallel, so when the switch is turned on, the load is halved to a value of 1.65 Ω. The programming of the controller was done in STM32 Cube IDE. In the program, the data from the microcontroller was sent directly to Matlab for monitoring and analysis purposes. The three-phase IGBT switches were operated at a frequency of 40 kHz to decrease the operational values of inductors required in the LC filter. The values of the controller gains are given in Table 6.2.

Table 6.1 Nominal Parameter Values of the Prototype

Description of parameters	Nominal value
Input Voltage, V_S	40V
Inductor	100 μH
Capacitor	20 μF
Load Resistors	3.3 Ω
Output Voltage, V_O	24 V (pp)
Nominal Frequency, f	50 Hz
‘ Switching Frequency, f_{sw}	40 kHz

Table 6.2 Controller gains and Observer Gains

Description of parameters	Nominal value
Controller Gain, K	1
α_1	1.25
α_2	0.080
β	4.0
γ	7
k_1	5.5 x 10^4
k_2	5.35 x 10^4
k_3	5 x 10^2
k_4	2 x 10^4

6.1.1 Experimental Results

Initially, the controller was operated at the nominal values given in Table 6.1. For a load of 3.3 Ω, with the converter operated at steady-state we get the following waveforms for voltage and inductor current on the oscilloscope. It should be noted that for the ease of voltage sensor implementation, the voltage was sensed between the phase and neutral points. Hence, the voltage seen in these figures here is actually 24 V divided by $\sqrt{3}$. This can also be seen from the fact that the voltages and current in the oscilloscope waveforms are in fact in phase.

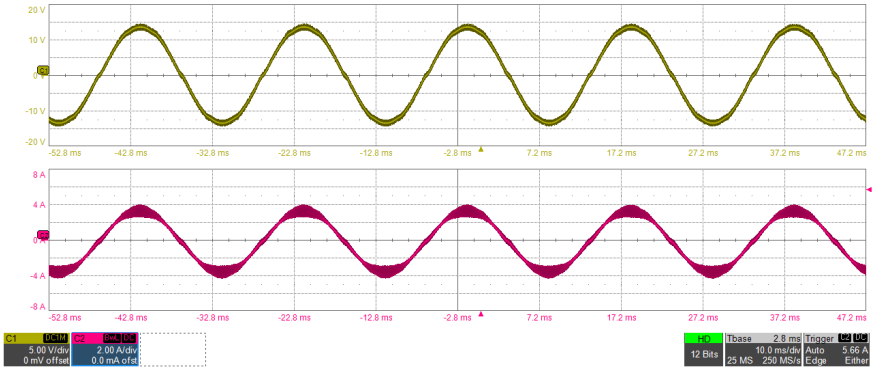

Fig. 6.2 Oscilloscope waveform for 3.3 Ω load.

As shown in Fig. 6.2, the voltage is tracked perfectly for the given reference value. The inductor current is perfectly in phase with the voltage. The slight perturbation in the voltage waveform at zero crossing is due to dead time implemented in the operation of IGBT switches to prevent shorting of switches.

As stated earlier, the data is transferred to Matlab from the microcontroller and sensors. Using a simple script, the following graphs of voltage and current can be drawn for these set of conditions, as shown in Fig. 6.3. Through the Matlab script, the voltage was converted to phase to neutral value.

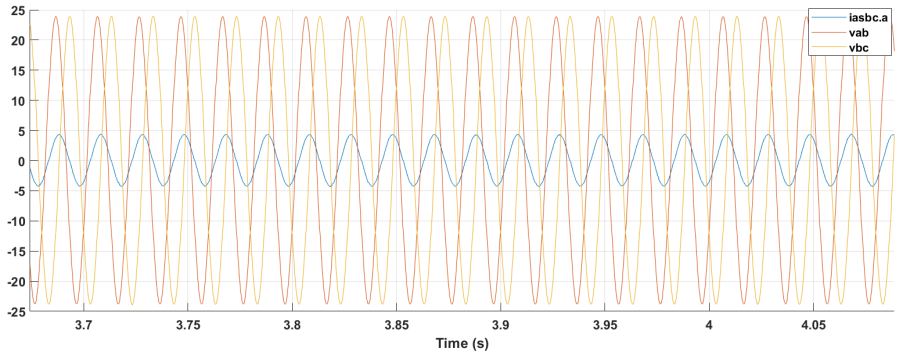

Fig. 6.3 Matlab results for 3.3 Ω load.

The next step in the testing was to turn the switch on and monitor the performance of the controller when the load resistance is halved. The resulting oscilloscope waveform is shown in Fig. 6.4.

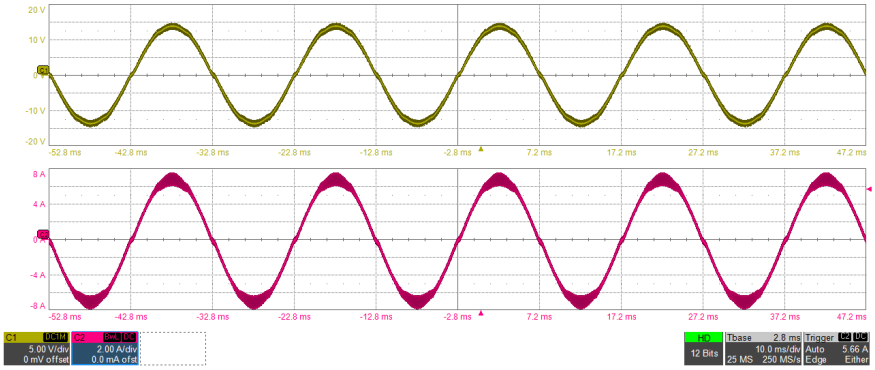

Fig. 6.4 Oscilloscope results for 1.65 Ω load.

As seen in the figure, the voltage remains constant while the current is doubled. The corresponding voltage and current waveforms from Matlab are shown in Fig.

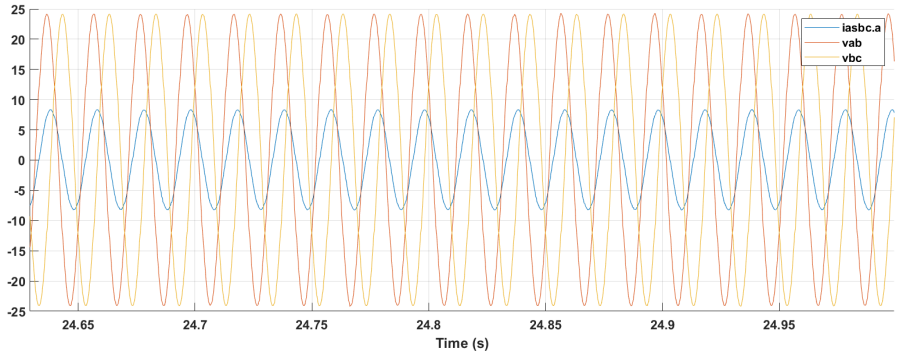

Fig. 6.5 Matlab results for 1.65 Ω load.

6.5, which also shows how the voltage remains constant while the current doubles in value.

But the most important part of the transition period when the switch is turned on. To validate the performance of controller, multiple screenshots of voltage and current waveforms were recorded at the instant of switching from 3.3 Ω load to 1.65 Ω load. These oscilloscope screenshots are shown in Fig. 6.6.

Fig. 6.6 shows instances of four different times when the switch was turned on. The results show that while the current was doubled each time, the voltage remained constant for each case.

This can also be seen from the figures plotted from gathered data in Matlab. Two instances of triggers are shown in Fig. 6.7. As seen in both figures, even when the load is increased by a factor of two, the voltage is held at a constant value, thus confirming the effectiveness of the proposed controller.

6.1.2 Comparison with another dual loop PID controller

To compare the results obtained for the regulation of inverter prototype, a dual-loop cascaded controller with an outer voltage loop and an inner current control loop has also been implemented.

To test its performance, again the linear load was stepped down from 3.3 Ω to 1.65 Ω.The variations in the load voltage as shown in the oscilloscope can be seen in figure 6.8.

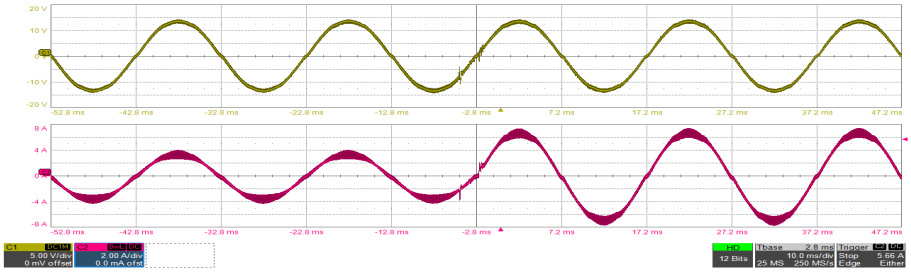

(a)

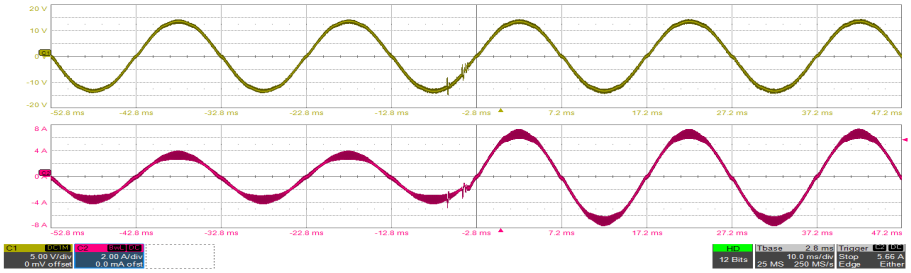

(b)

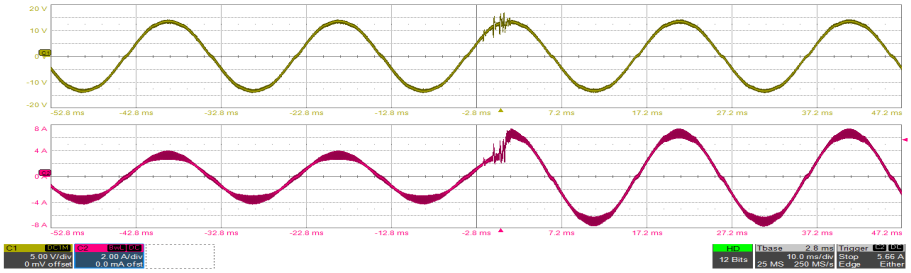

(c)

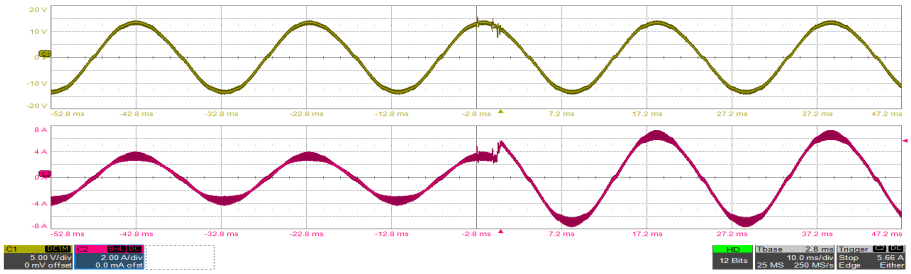

(d)

Fig. 6.6 Voltage and current waveforms screenshots for different trigger points.

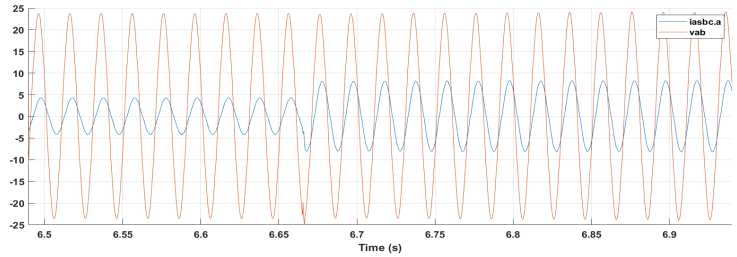

(a)

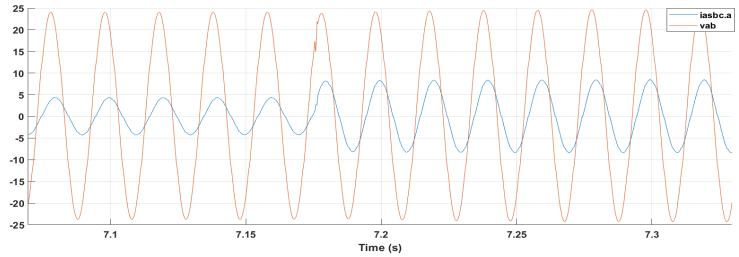

(b)

Fig. 6.7 Voltage and current waveforms as plotted in Matlab for two different trigger instances.

Data was again also collected in MATLAB. The output voltage response due to load change is shown in Fig. 6.9. As seen from the figure, there is no significant steady-state error in the response (same as in our case) but the voltage does take longer to reach the steady-state value (approximately 20 ms). Concerning the Total Harmonic Distortion, for the TCB controller the resulting THD% is 1.258%, while for the cascaded control loop the THD% is around 3.275%.

6.2 Real-time Simulation of a Grid-Forming Inverter

In order to test the performance of our controller for the proposed GFM inverter, it was deemed appropriate to also validate it by testing it in a real-time simulator using OPAL-RT 5700. This allows the operators to study the response of our proposed controller without a physical implementation but the simulation is performed in real-time.

Hardware-in-the-Loop (HIL) is a technique that enables the real-time simulation of a physical system. This approach is primarily used to examine prototypes or new

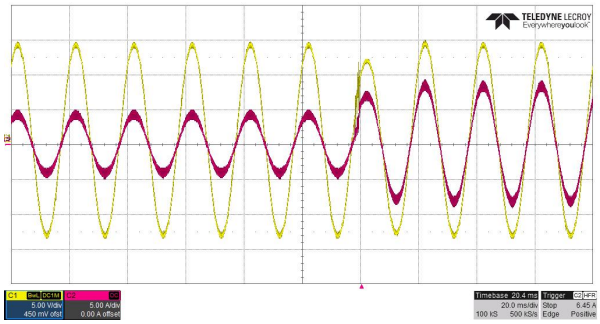

Fig. 6.8 An output voltage response of a cascaded dual loop controller on oscilloscope.

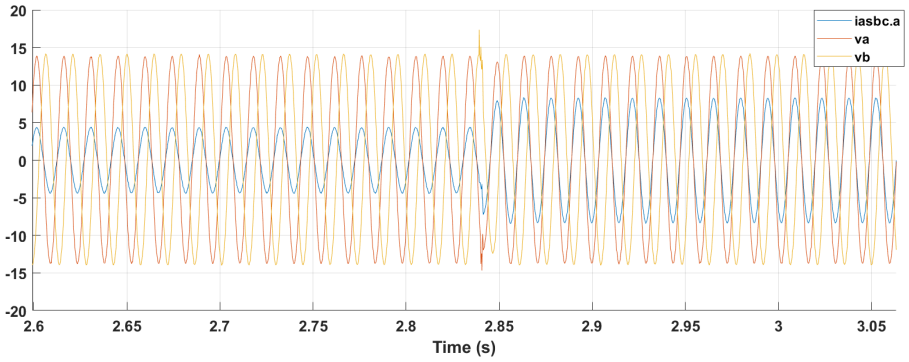

Fig. 6.9 An output voltage response of a cascaded dual loop controller as collected in Matlab.

technologies intended for integration into actual energy systems. It allows for testing protection devices, control algorithms, and power electronic devices without directly connecting them to the main system. There are two main reasons for avoiding direct connection:

- Connecting an untested physical device to the grid could endanger both the grid stability and the device itself. Simulations provide a safe environment to test devices under virtually all possible fault conditions and operating scenarios.
- During the early stages of development, a prototype may only exist as a mathematical model or simulation, rather than a physical device.

In the case analyzed, the inverter model was loaded into an Electric Hardware Solver (eHS) based simulator capable of operating at high frequency (time step of 1 μs). The controller was loaded in Matlab/Simulink and operated at a more manageable time-step of 40 μs.

To test the controller, the load was changed from 80 Ω to 20 Ω. The resulting variation in the output voltage is shown in Fig. 6.10.

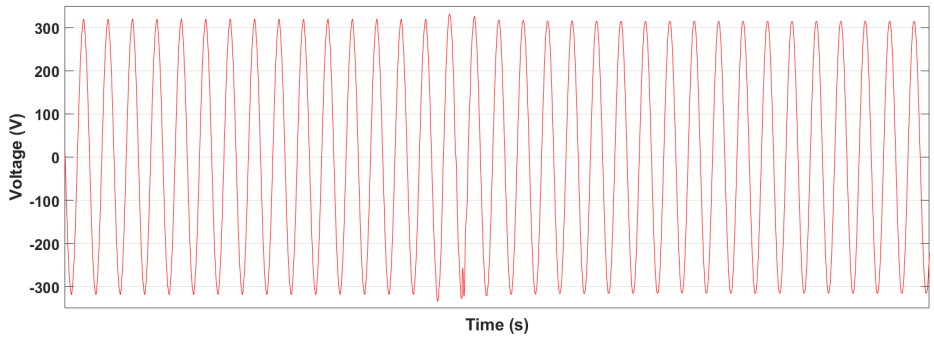

Fig. 6.10 Real-time simulation results for 80 Ω to 20 Ω load variation.

The corresponding change in the value of $\hat{\theta}$ is shown in Fig. 6.11.

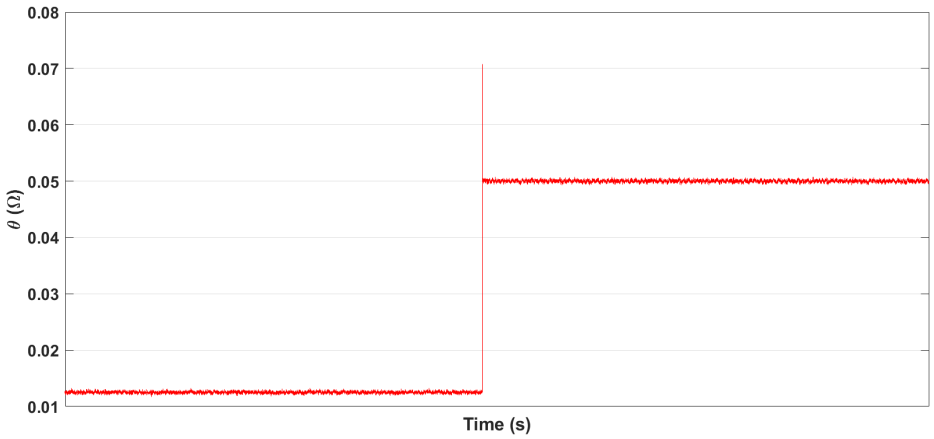

Fig. 6.11 Real-time simulation results for 80 Ω to 20 Ω load variation for Theta.

Similarly, the output voltage due to input voltage variation is shown in Fig. 6.12.

As seen from the figures, the simulations worked in real-time as well. Even for large load and input voltage variations, there was no corresponding voltage variation in the output voltage.

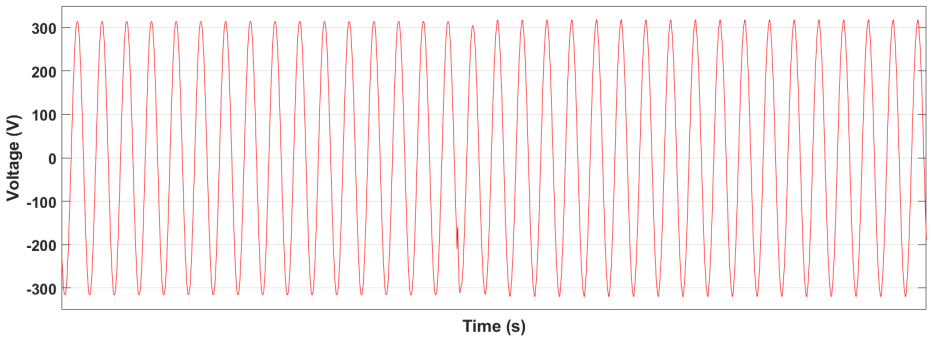

Fig. 6.12 Real-time simulation results for input voltage variation.

Chapter 7

Conclusion

This thesis has developed and demonstrated the effectiveness of applying an advanced adaptive control strategy for power converters, leveraging the Torelli Control Box approach. The central aim has been to address the dynamic and fast transient conditions posed by renewable energy sources in modern power systems, ensuring stability, efficiency, and robust performance across various applications.

The research presented herein highlights several significant contributions to the field of power systems and power converter control. The research started by using the TCB approach to effectively convert dynamics constrained by Differential Algebraic Equations into Ordinary differential equations, simplifying the modeling of Non-Isolated Single Input Multiple Output DC-DC converters. This was validated through simulations performed in Matlab/Simulink environment.

Then the TCB approach was successfully applied to both ideal and non-ideal Buck and Boost DC-DC converter topologies. The results showcased improved control responses, as verified by hardware prototypes, indicating the robustness and effectiveness of the proposed control strategy.

Similarly, the application of the proposed approach was extended towards renewable energy systems. A novel MPPT algorithm was proposed, based on the TCB approach. The control algorithm was developed and tested, showing effective performance even under varying environmental conditions. This contribution underscores the adaptability of the TCB approach in optimizing energy harvesting from RES.

The regulation of a single-phase inverter for bidirectional power flow in V2G systems was also demonstrated. The TCB approach facilitated efficient and reliable control, highlighting its potential for enhancing the integration of electric vehicles into the power grid.

Finally, the TCB approach was extended to three-phase inverters for uninterruptible power supply applications and grid-forming operations. The TCB formulation is suitable for both abc and dq coordinates for controller design. Comprehensive testing, both in simulation and through hardware prototypes, confirmed the capability of the approach to maintain stability and performance in various operational scenarios.

Each chapter of this thesis has incrementally built upon the foundational TCB principles, applying them to increasingly complex and practical scenarios. The simulations and experimental results consistently validate the theoretical findings, demonstrating the versatility and reliability of the TCB-based approach across different types of power converters and applications.

In conclusion, this thesis has contributed a novel and effective control strategy for power converters, applicable to grid-connected converters supplied by renewable energy systems. The adaptive nature of the TCB approach, grounded in the Lyapunov stability theory, offers a promising alternative to traditional control methods, simplifying implementation while ensuring robust performance. The outcomes of this research pave the way for more efficient and resilient microgrids, promoting greater integration of renewable energy sources into modern power systems. Future work may explore further optimization and scaling of the TCB-based approach, as well as its application to other emerging technologies in the energy sector.

References

[1] Marian Wilhun. Over one trillion watts of wind and solar installed. https://www.pv-magazine.com/2018/08/02/milestone-over-one-trillion-watts-of-wind-and-solar-installed/, 2018.

[2] Sayan Samanta. *Modeling and Control of Grids of Near Future with Converters and Synchronous Machines*. The Pennsylvania State University, 2023.

[3] Pontus Roos. A comparison of grid-forming and grid-following control of VSCs, Dissertation Uppsala Universitet, Sweden, 2020.

[4] Ngoc-Bao Lai, Andres Tarrasó, Gregory N Baltas, Leonardo V Marin Arevalo, and Pedro Rodriguez. External inertia emulation controller for grid-following power converter. *IEEE Transactions on Industry Applications*, 57(6):6568–6576, 2021.

[5] Dinesh Pattabiraman, Robert H Lasseter, and Thomas M Jahns. Comparison of grid following and grid forming control for a high inverter penetration power system. In *2018 IEEE Power & Energy Society General Meeting (PESGM)*, pages 1–5. IEEE, 2018.

[6] Ali Tayyebi, Florian Dörfler, Friederich Kupzog, Zoran Miletic, and Wolfgang Hribernik. Grid-forming converters–inevitability, control strategies and challenges in future grids application. 2018.

[7] Jean-Jacques E Slotine, Weiping Li, et al. *Applied nonlinear control*, volume 199. Prentice hall Englewood Cliffs, NJ, 1991.

[8] Tom Athay, Robin Podmore, and Sudhir Virmani. A practical method for the direct analysis of transient stability. *IEEE Transactions on Power Apparatus and Systems*, (2):573–584, 1979.

[9] Mania Ribbens-Pavella and Frank J Evans. Direct methods for studying dynamics of large-scale electric power systems—a survey. *Automatica*, 21(1):1–21, 1985.

[10] Anantha Pai. *Energy function analysis for power system stability*. Springer Science & Business Media, 1989.

[11] Mania Pavella, Damien Ernst, and Daniel Ruiz-Vega. *Transient stability of power systems: a unified approach to assessment and control*. Springer Science & Business Media, 2012.

[12] Alberto Isidori. Feedback control of nonlinear systems. *International Journal of Robust and Nonlinear Control*, 2(4):291–311, 1992.

[13] Hassan K Khalil. *Control of nonlinear systems*. Prentice Hall, New York, NY, 2002.

[14] Björn Wittenmark. *Adaptive control*. Addison-Wesley, 1989.

[15] Shankar Sastry and Marc Bodson. *Adaptive control: stability, convergence and robustness*. Courier Corporation, 2011.

[16] Muhammad Ahmed Qureshi, Francesco Torelli, Andrea Mazza, and Gianfranco Chicco. Application of artificial dynamics to represent non-isolated single-input multiple-output DC-DC converters with averaged models. In *2021 56th International Universities Power Engineering Conference (UPEC)*, pages 1–6. IEEE, 2021.

[17] Muhammad Ahmed Qureshi, Salvatore Musumeci, Francesco Torelli, Alberto Reatti, Andrea Mazza, and Gianfranco Chicco. Application of a novel adaptive control approach for the regulation of power converters. In *2022 57th International Universities Power Engineering Conference (UPEC)*, pages 1–6. IEEE, 2022.

[18] Muhammad Ahmed Qureshi, Salvatore Musumeci, Francesco Torelli, Alberto Reatti, Andrea Mazza, and Gianfranco Chicco. Application of advanced model reference adaptive control for bidirectional AC-DC converters. In *2023 58th International Universities Power Engineering Conference (UPEC)*, pages 1–5. IEEE, 2023.

[19] Muhammad Ahmed Qureshi, Francesco Torelli, Salvatore Musumeci, Alberto Reatti, Andrea Mazza, and Gianfranco Chicco. A novel adaptive control approach for maximum power-point tracking in photovoltaic systems. *Energies*, 16(6):2782, 2023.

[20] Muhammad Ahmed Qureshi, Salvatore Musumeci, Francesco Torelli, Alberto Reatti, Andrea Mazza, and Gianfranco Chicco. A novel model reference adaptive control approach investigation for power electronic converter applications. *International Journal of Electrical Power & Energy Systems*, 156:109722, 2024.

[21] Robert David Middlebrook and Slobodan Ćuk. A general unified approach to modelling switching-converter power stages. In IEEE, editor, *1976 IEEE Power Electronics Specialists Conference*, pages 18–34.

[22] Chi Kong Tse, Yuk Ming Lai, and Herbert Ho-Ching Iu. Hopf bifurcation and chaos in a free-running current-controlled cuk switching regulator. *IEEE Transactions on Circuits and Systems I: Fundamental Theory and Applications*, 47(4):448–457, 2000.

[23] Robert W. Erickson, Slobodan. Ćuk, and Robert David Middlebrook. Large-signal modelling and analysis of switching regulators. In *1982 IEEE Power Electronics Specialists Conference*, pages 240–250, 1982.

[24] Philip T. Krein, Joseph Bentsman, Richard M. Bass, and Bernard L. Lesieutre. On the use of averaging for the analysis of power electronic systems. *IEEE Transaction on Power Electronics*, 5(2):182–190, April 1990.

[25] George C Verghese, Malik E Elbuluk, and John G Kassakian. A general approach to sampled-data modeling for power electronic circuits. *IEEE Transactions on Power Electronics*, (2):76–89, 1986.

[26] David C Hamill, Jonathan HB Deane, and David J Jefferies. Modeling of chaotic DC-DC converters by iterated nonlinear mappings. *IEEE Transactions on Power Electronics*, 7(1):25–36, 1992.

[27] Xiaolu Lucia Li, Zheng Dong, and K Tse Chi. Complete family of two-stage single-input multioutput configurations of interconnected power converters. *IEEE Transactions on Power Electronics*, 35(4):3713–3728, 2019.

[28] Sreeshma Markkassery, Akshit Saradagi, Arun D Mahindrakar, N Lakshminarasamma, and Ramkrishna Pasumarthy. Modeling, design and control of non-isolated single-input multi-output zeta–buck–boost converter. *IEEE Transactions on Industry Applications*, 56(4):3904–3918, 2020.

[29] Shmuel Ben-Yaakov. Behavioral average modeling and equivalent circuit simulation of switched capacitors converters. *IEEE Transactions on Power Electronics*, 27(2):632–636, 2011.

[30] Marek S Makowski. On systematic modeling of switched capacitor DC-DC converters: Incremental graph approach. In *2010 IEEE 12th Workshop on Control and Modeling for Power Electronics (COMPEL)*, pages 1–6. IEEE, 2010.

[31] Thomas Souvignet, Bruno Allard, and Xuefang Lin-Shi. Sampled-data modeling of switched-capacitor voltage regulator with frequency-modulation control. *IEEE Transactions on Circuits and Systems I: Regular Papers*, 62(4):957–966, 2015.

[32] Elisa Mostacciuolo, Stephan Trenn, and Francesco Vasca. Partial averaging for switched DAEs with two modes. In *2015 European Control Conference (ECC)*, pages 2896–2901. IEEE, 2015.

[33] Francesco Torelli and Alfredo Vaccaro. A generalized computing paradigm based on artificial dynamic models for mathematical programming. *Soft Computing*, 18:1561–1573, 2014.

[34] Maria Bella Ferrera Prieto, Salvador Perez Litran, Eladio Duran Aranda, and Juan Manuel Enrique Gomez. New single-input, multiple-output converter topologies: Combining single-switch nonisolated DC-DC converters for single-input, multiple-output applications. *IEEE Industrial Electronics Magazine*, 10(2):6–20, 2016.

[35] Eladio Durán, Salvador P Litrán, María Bella Ferrera, and José Manuel Andújar. A zeta-buck-boost converter combination for single-input multiple-output applications. In *IECON 2016-42nd Annual Conference of the IEEE Industrial Electronics Society*, pages 1251–1256. IEEE, 2016.

[36] Sreeshma Markkassery, Arun D Mahindrakar, N Lakshminarasamma, and Ramkrishna Pasumarthy. Modelling of non-isolated single-input-multi-output DC-DC converter. In *2018 IEEE International Conference on Power Electronics, Drives and Energy Systems (PEDES)*, pages 1–6. IEEE, 2018.

[37] Francesco Torelli, Pasquale Montegiglio, Antonio De Bonis, João PS Catalão, Gianfranco Chicco, and Andrea Mazza. A new approach for solving DAE systems applied to distribution networks. In *2014 49th International Universities Power Engineering Conference (UPEC)*, pages 1–6. IEEE, 2014.

[38] Muhammad Ahmad Qureshi, Iftikhar Ahmad, and Muhammad Faizan Munir. Double integral sliding mode control of continuous gain four quadrant quasi-z-source converter. *IEEE Access*, 6:77785–77795, 2018.

[39] Hassan El Fadil and Fouad Giri. Backstepping based control of PWM DC-DC boost power converters. In *2007 IEEE international symposium on Industrial Electronics*, pages 395–400. IEEE, 2007.

[40] Kasinathan Padmanathan, Uma Govindarajan, Vigna K Ramachandaramurthy, Baskaran Jeevarathinam, et al. Integrating solar photovoltaic energy conversion systems into industrial and commercial electrical energy utilization—a survey. *Journal of Industrial Information Integration*, 10:39–54, 2018.

[41] Calogero Cavallaro, Salvatore Musumeci, C Santonocito, and Marco Pappalardo. Smart photovoltaic UPS system for domestic appliances. In *2009 International Conference on Clean Electrical Power*, pages 699–704. IEEE, 2009.

[42] Mohammad I Fahmi, Rajprasad Rajkumar, Roselina Arelhi, and D Isa. Solar PV system for off-grid electrification in rural area. 2014.

[43] Abhishek Awasthi, Amitabh Sinha, Asheesh K Singh, and R Veeraganesan. Solar PV fed grid integration with energy storage system for electric traction application. In *2016 10th International Conference on Intelligent Systems and Control (ISCO)*, pages 1–5. IEEE, 2016.

[44] Nian Liu and Minyang Cheng. Effectiveness evaluation for a commercialized PV-assisted charging station. *Sustainability*, 9(2):323, 2017.

[45] Furquan Nadeem, SM Suhail Hussain, Prashant Kumar Tiwari, Arup Kumar Goswami, and Taha Selim Ustun. Comparative review of energy storage systems, their roles, and impacts on future power systems. *IEEE Access*, 7:4555–4585, 2018.

[46] Dalila Beriber and Abdelaziz Talha. MPPT techniques for PV systems. In *4th International Conference on Power Engineering, Energy and Electrical Drives*, pages 1437–1442. IEEE, 2013.

[47] Bouchra Bakhiyi, France Labrèche, and Joseph Zayed. The photovoltaic industry on the path to a sustainable future—environmental and occupational health issues. *Environment International*, 73:224–234, 2014.

[48] Filippo Chimento, Salvatore Musumeci, Angelo Raciti, C Sapuppo, and Mario Di Guardo. A control algorithm for power converters in the field of photovoltaic applications. In *2007 European Conference on Power Electronics and Applications*, pages 1–9. IEEE, 2007.

[49] Mohammad Sarvi and Ahmad Azadian. A comprehensive review and classified comparison of MPPT algorithms in PV systems. *Energy Systems*, 13(2):281–320, 2022.

[50] Mohamed Derbeli, Cristian Napole, Oscar Barambones, Jesus Sanchez, Isidro Calvo, and Pablo Fernández-Bustamante. Maximum power point tracking techniques for photovoltaic panel: A review and experimental applications. *Energies*, 14(22):7806, 2021.

[51] Leopoldo Gil-Antonio, Martha Belem Saldivar-Marquez, and Otniel Portillo-Rodriguez. Maximum power point tracking techniques in photovoltaic systems: A brief review. In *2016 13th International Conference on Power Electronics (CIEP)*, pages 317–322. IEEE, 2016.

[52] Eftichios Koutroulis and Frede Blaabjerg. A new technique for tracking the global maximum power point of PV arrays operating under partial-shading conditions. *IEEE Journal of Photovoltaics*, 2(2):184–190, 2012.

[53] Tat Luat Nguyen and Kay-Soon Low. A global maximum power point tracking scheme employing direct search algorithm for photovoltaic systems. *IEEE Transactions on Industrial Electronics*, 57(10):3456–3467, 2010.

[54] KL Lian, JH Jhang, and IS Tian. A maximum power point tracking method based on perturb-and-observe combined with particle swarm optimization. *IEEE Journal of Photovoltaics*, 4(2):626–633, 2014.

[55] Kinattingal Sundareswaran, Vethanayagam Vigneshkumar, Peddapati Sankar, Sishaj P Simon, P Srinivasa Rao Nayak, and Sankaran Palani. Development of an improved P&O algorithm assisted through a colony of foraging ants for MPPT in PV system. *IEEE Transactions on Industrial Informatics*, 12(1):187–200, 2015.

[56] Ankur Kumar Gupta, Rupendra Kumar Pachauri, Tanmoy Maity, Yogesh K Chauhan, Om Prakash Mahela, Baseem Khan, and Pankaj Kumar Gupta. Effect of various incremental conductance MPPT methods on the charging of battery load feed by solar panel. *IEEE Access*, 9:90977–90988, 2021.

[57] Young-Hyok Ji, Doo-Yong Jung, Jun-Gu Kim, Jae-Hyung Kim, Tae-Won Lee, and Chung-Yuen Won. A real maximum power point tracking method for mismatching compensation in PV array under partially shaded conditions. *IEEE Transactions on Power Electronics*, 26(4):1001–1009, 2010.

[58] Héctor Felipe Mateo Romero, Miguel Ángel González Rebollo, Valentín Cardeñoso-Payo, Victor Alonso Gómez, Alberto Redondo Plaza, Ranganai Tawanda Moyo, and Luis Hernández-Callejo. Applications of artificial intelligence to photovoltaic systems: a review. *Applied Sciences*, 12(19):10056, 2022.

[59] Mostefa Kermadi, Zainal Salam, Ali M Eltamaly, Jubaer Ahmed, Saad Mekhilef, Cherif Larbes, and El Madjid Berkouk. Recent developments of MPPT techniques for PV systems under partial shading conditions: a critical review and performance evaluation. *IET Renewable Power Generation*, 14(17):3401–3417, 2020.

[60] Amit Kumer Podder, Naruttam Kumar Roy, and Hemanshu Roy Pota. MPPT methods for solar PV systems: a critical review based on tracking nature. *IET Renewable Power Generation*, 13(10):1615–1632, 2019.

[61] Zain Ahmad Khan, Laiq Khan, Saghir Ahmad, Sidra Mumtaz, Muhammad Jafar, and Qudrat Khan. RBF neural network based backstepping terminal sliding mode MPPT control technique for PV system. *Plos one*, 16(4):e0249705, 2021.

[62] Ali M Eltamaly. A novel musical chairs algorithm applied for MPPT of PV systems. *Renewable and Sustainable Energy Reviews*, 146:111135, 2021.

[63] Liang Mingyu, Cai Xinhong, and Cao Bingyu. Random inertia weight pso based MPPT for solar PV under partial shaded condition. In *IOP Conference Series: Earth and Environmental Science*, volume 585, page 012028. IOP Publishing, 2020.

[64] Walid SE Abdellatif, Mohamed Saad Mohamed, Shimaa Barakat, and Ayman Brisha. A fuzzy logic controller based MPPT technique for photovoltaic generation system. *International Journal on Electrical Engineering & Informatics*, 13(2), 2021.

[65] Amar B. Shinde, Amruta S. Deshpande, and Snehal Unde. Design and simulation of self-tuning pid controller with MPPT for solar array using matlab/simulink. In *2022 13th International Conference on Computing Communication and Networking Technologies (ICCCNT)*, pages 1–6, 2022.

[66] Arun Ghosh, Siva Ganesh Malla, and Chandrasekhar Narayan Bhende. Small-signal modelling and control of photovoltaic based water pumping system. *ISA Transactions*, 57:382–389, 2015.

[67] Hammad Armghan, Iftikhar Ahmad, Ammar Armghan, Saud Khan, Muhammad Arsalan, et al. Backstepping based non-linear control for maximum power point tracking in photovoltaic system. *Solar Energy*, 159:134–141, 2018.

[68] Muhammad Arsalan, Ramsha Iftikhar, Iftikhar Ahmad, Ammar Hasan, K Sabahat, and A Javeria. MPPT for photovoltaic system using nonlinear backstepping controller with integral action. *Solar Energy*, 170:192–200, 2018.

[69] Mohammed A Alsumiri and Lin Jiang. Sliding mode maximum power point tracking controller for photovoltaic energy conversion system with a SEPIC converter. In *Proceedings of the Eighth Saudi Students Conference in the UK*, pages 463–475. World Scientific, 2016.

[70] Siew-Chong Tan, Yuk-Ming Lai, K Tse Chi, Luis Martínez-Salamero, and Chi-Kin Wu. A fast-response sliding-mode controller for boost-type converters with a wide range of operating conditions. *IEEE Transactions on Industrial Electronics*, 54(6):3276–3286, 2007.

[71] Siew-Chong Tan and Yuk-Ming Lai. Constant-frequency reduced-state sliding mode current controller for cuk converters. *IET Power Electronics*, 1(4):466–477, 2008.

[72] Tong Yang, Ning Sun, Yongchun Fang, Xin Xin, and He Chen. New adaptive control methods for n-link robot manipulators with online gravity compensation: Design and experiments. *IEEE Transactions on Industrial Electronics*, 69(1):539–548, 2021.

[73] Li Sun. Helicopter hovering control design based on model reference adaptive method. In *2019 IEEE 3rd Information Technology, Networking, Electronic and Automation Control Conference (ITNEC)*, pages 1621–1624. IEEE, 2019.

[74] WD Morse and KA Ossman. Model following reconfigurable flight control system for the AFTI/f-16. *Journal of Guidance, Control, and Dynamics*, 13(6):969–976, 1990.

[75] Hossein Safamehr, Tooraj Abbasian Najafabadi, and Farzad Rajaei Salmasi. Adaptive control of grid-connected inverters with nonlinear LC filters. *IEEE Transactions on Power Electronics*, 38(2):1562–1570, 2023.

[76] Francesco Torelli and Alfredo Vaccaro. A generalized computing paradigm based on artificial dynamic models for mathematical programming. *Soft Computing*, 18(8):1561–1573, 2014.

[77] Ning Xie, Franco Torelli, Ettore Bompard, and Alfredo Vaccaro. Dynamic computing paradigm for comprehensive power flow analysis. *IET generation, transmission & distribution*, 7(8):832–842, 2013.

[78] Francesco Torelli, Alfredo Vaccaro, and Ning Xie. A novel optimal power flow formulation based on the Lyapunov theory. *IEEE Transactions on Power Systems*, 28(4):4405–4415, 2013.

[79] Francesco Torelli, Pasquale Montegiglio, Antonio De Bonis, João PS Catalão, Gianfranco Chicco, and Andrea Mazza. A new approach for solving DAE systems applied to distribution networks. In *2014 49th International Universities Power Engineering Conference (UPEC)*, pages 1–6. IEEE, 2014.

[80] Ramsha Iftikhar, Iftikhar Ahmad, Muhammad Arsalan, Neelma Naz, Naghmash Ali, and Hammad Armghan. MPPT for photovoltaic system using nonlinear controller. *International Journal of Photoenergy*, 2018, 2018.

[81] Mustafa Engin Başoğlu and Bekir Çakır. Comparisons of MPPT performances of isolated and non-isolated DC–DC converters by using a new approach. *Renewable and Sustainable Energy Reviews*, 60:1100–1113, 2016.

[82] Ignacio Galiano Zurbriggen and Martin Ordonez. PV energy harvesting under extremely fast changing irradiance: State-plane direct MPPT. *IEEE Transactions on Industrial Electronics*, 66(3):1852–1861, 2019.

[83] Sava Marinkov, Bram de Jager, and Maarten Steinbuch. Extremum seeking control with data-based disturbance feedforward. In *2014 American Control Conference*, pages 3627–3632, 2014.

[84] Simone Baldi, Antonis Papachristodoulou, and Elias B Kosmatopoulos. Adaptive pulse width modulation design for power converters based on affine switched systems. *Nonlinear Analysis: Hybrid Systems*, 30:306–322, 2018.

[85] Vishwanatha Siddhartha and Yogesh V Hote. Systematic circuit design and analysis of a non-ideal DC-DC pulse width modulation boost converter. *IET Circuits, Devices & Systems*, 12(2):144–156, 2018.

[86] Miklos Csizmadia and Miklos Kuczmann. Extended feedback linearisation control of non-ideal DC-DC buck converter in continuous-conduction mode. *Power Electronics and Drives*, 7(1):1–8, 2022.

[87] Vlad Mihaly, Mircea Susca, and Petru Dobra. Passivity-based controller for nonideal DC-to-DC boost converter. In *2019 22nd International Conference on Control Systems and Computer Science (CSCS)*, pages 30–35. IEEE, 2019.

[88] Murat Yilmaz and Philip T. Krein. Review of the impact of vehicle-to-grid technologies on distribution systems and utility interfaces. *IEEE Transactions on Power Electronics*, 28(12):5673–5689, 2013.

[89] M. Bharathidasan and V. Indragandhi. Review of power factor correction (PFC) AC/DC-DC power electronic converters for electric vehicle applications. *IOP Conference Series: Materials Science and Engineering*, 906(1):012006, aug 2020.

[90] Aziz Rachid, Hassan EL Fadil, F. Z. Belhaj, K. Gaouzi, and Fouad Giri. Lyapunov-based control of single-phase AC-DC power converter for bev charger. In Soumia El Hani and Mohamad Essaaidi, editors, *Recent Advances in Electrical and Information Technologies for Sustainable Development*. Springer International Publishing, 2019.

[91] Sertac Bayhan, S Sajjad Seyedalipour, Hasan Komurcugil, and Haitham Abu-Rub. Lyapunov energy function based control method for three-phase UPS inverters with output voltage feedback loops. *IEEE Access*, 7:113699–113711, 2019.

[92] Dragan Jovcic, Nalin Pahalawaththa, and Mohamed Zavahir. Investigation of the use of inverter control strategy instead of synchronous condensers at inverter terminal of an HVDC system. *IEEE Transactions on Power Delivery*, 15(2):704–709, 2000.

[93] Youjun Zhang and Xinbo Ruan. Three-phase AC-AC converter with controllable phase and amplitude. *IEEE Transactions on Industrial Electronics*, 62(9):5689–5699, 2015.

[94] Rusong Wu, Shashi B Dewan, and Gordon R Slemon. Analysis of an AC-to-DC voltage source converter using PWM with phase and amplitude control. *IEEE Transactions on Industry Applications*, 27(2):355–364, 1991.

[95] Mansour Mohseni and Syed M Islam. A new vector-based hysteresis current control scheme for three-phase PWM voltage-source inverters. *IEEE Transactions on Power Electronics*, 25(9):2299–2309, 2010.

[96] Donald Grahame Holmes, Reza Davoodnezhad, and Brendan P McGrath. An improved three-phase variable-band hysteresis current regulator. *IEEE Transactions on Power Electronics*, 28(1):441–450, 2012.

[97] Zhanfeng Song, Changliang Xia, and Tao Liu. Predictive current control of three-phase grid-connected converters with constant switching frequency for wind energy systems. *IEEE Transactions on Industrial Electronics*, 60(6):2451–2464, 2012.

[98] Sergio Vazquez, Jose Rodriguez, Marco Rivera, Leopoldo G Franquelo, and Margarita Norambuena. Model predictive control for power converters and drives: Advances and trends. *IEEE Transactions on Industrial Electronics*, 64(2):935–947, 2016.

[99] Venkata Yaramasu, Marco Rivera, Mehdi Narimani, Bin Wu, and José Rodriguez. Model predictive approach for a simple and effective load voltage

control of four-leg inverter with an output *LC* filter. *IEEE Transactions on Industrial Electronics*, 61(10):5259–5270, 2014.

[100] Hoach The Nguyen, Jinuk Kim, and Jin-Woo Jung. Improved model predictive control by robust prediction and stability-constrained finite states for three-phase inverters with an output *LC* filter. *IEEE Access*, 7:12673–12685, 2019.

[101] Paolo Mattavelli. An improved deadbeat control for UPS using disturbance observers. *IEEE Transactions on Industrial Electronics*, 52(1):206–212, 2005.

[102] Mohammad Pichan, Hasan Rastegar, and Mohammad Monfared. Deadbeat control of the stand-alone four-leg inverter considering the effect of the neutral line inductor. *IEEE Transactions on Industrial Electronics*, 64(4):2592–2601, 2016.

[103] Tzann-Shin Lee, Kune-Shiang Tzeng, and Mai-Shiang Chong. Robust controller design for a single-phase UPS inverter using μ-synthesis. *IEE Proceedings-Electric Power Applications*, 151(3):334–340, 2004.

[104] Dong-Eok Kim and Dong-Choon Lee. Feedback linearization control of three-phase UPS inverter systems. *IEEE Transactions on Industrial Electronics*, 57(3):963–968, 2010.

[105] Osman Kukrer, Hasan Komurcugil, and Alper Doganalp. A three-level hysteresis function approach to the sliding-mode control of single-phase UPS inverters. *IEEE Transactions on Industrial Electronics*, 56(9):3477–3486, 2009.

[106] Mohammad Pichan and Hasan Rastegar. Sliding-mode control of four-leg inverter with fixed switching frequency for uninterruptible power supply applications. *IEEE Transactions on Industrial Electronics*, 64(8):6805–6814, 2017.

[107] Hasan Komurcugil and Osman Kukrer. Lyapunov-based control for three-phase PWM AC/DC voltage-source converters. *IEEE Transactions on Power Electronics*, 13(5):801–813, 1998.

[108] Salem Rahmani, Abdelhamid Hamadi, and Kamal Al-Haddad. A lyapunov-function-based control for a three-phase shunt hybrid active filter. *IEEE Transactions on Industrial Electronics*, 59(3):1418–1429, 2011.

[109] Arman Oshnoei and Frede Blaabjerg. Sliding mode-based model predictive control of grid-forming power converters. In *2023 European Control Conference (ECC)*, pages 1–6. IEEE, 2023.

[110] Fahmid Sadeque, Mehmetcan Gursoy, and Behrooz Mirafzal. Survey of control methods for grid-forming inverters–advancements from 2020 to 2023. In *2023 IEEE Kansas Power and Energy Conference (KPEC)*, pages 1–6. IEEE, 2023.

[111] Mohammad Sadegh Orfi Yeganeh, Arman Oshnoei, Nenad Mijatovic, Tomislav Dragicevic, and Frede Blaabjerg. Intelligent secondary control of islanded ac microgrids: A brain emotional learning-based approach. *IEEE Transactions on Industrial Electronics*, 70(7):6711–6723, 2022.

[112] Hector A Young, Victor A Marin, Cristian Pesce, and Jose Rodriguez. Simple finite-control-set model predictive control of grid-forming inverters with LCL filters. *IEEE Access*, 8:81246–81256, 2020.

[113] Mehmetcan Gursoy and Behrooz Mirafzal. Direct vs. indirect control schemes for grid-forming inverters–unveiling a performance comparison in a microgrid. *IEEE Access*, 2023.

[114] Cristian Lascu. Sliding-mode direct-voltage control of voltage-source converters with LC filters for pulsed power loads. *IEEE Transactions on Industrial Electronics*, 68(12):11642–11650, 2020.

[115] Ramon Guzman, Luis Garcia de Vicuña, Miguel Castilla, Jaume Miret, and Jordi de la Hoz. Variable structure control for three-phase LCL-filtered inverters using a reduced converter model. *IEEE Transactions on Industrial Electronics*, 65(1):5–15, 2017.

[116] Javier Morales, Luis Garcia de Vicuna, Ramon Guzman, Miguel Castilla, and Jaume Miret. Modeling and sliding mode control for three-phase active power filters using the vector operation technique. *IEEE Transactions on Industrial Electronics*, 65(9):6828–6838, 2018.

[117] Ramon Guzman, Luis Garcia de Vicuña, Miguel Castilla, Jaume Miret, and Helena Martin. Variable structure control in natural frame for three-phase grid-connected inverters with LCL filter. *IEEE Transactions on Power Electronics*, 33(5):4512–4522, 2017.

[118] Ikram Maaoui-Ben Hassine, Mohamed Wissem Naouar, and Najiba Mrabet-Bellaaj. Model predictive-sliding mode control for three-phase grid-connected converters. *IEEE Transactions on Industrial Electronics*, 64(2):1341–1349, 2016.

[119] Hasan Komurcugil. Rotating-sliding-line-based sliding-mode control for single-phase UPS inverters. *IEEE Transactions on Industrial Electronics*, 59(10):3719–3726, 2011.

[120] Yu Qi, Li Peng, Manlin Chen, and Zeyi Huang. Load disturbance suppression for voltage-controlled three-phase voltage source inverter with transformer. *IET Power Electronics*, 7(12):3147–3158, 2014.

[121] Patricio Cortes, Gabriel Ortiz, Juan I. Yuz, JosÉ Rodriguez, Sergio Vazquez, and Leopoldo G. Franquelo. Model predictive control of an inverter with output *LC* filter for UPS applications. *IEEE Transactions on Industrial Electronics*, 56(6):1875–1883, 2009.

[122] Jinsong He and Xin Zhang. A modified lyapunov-based control scheme for a three-phase UPS with an optimal third-order load current observer. In *2019 IEEE 10th International Symposium on Power Electronics for Distributed Generation Systems (PEDG)*, pages 233–236. IEEE, 2019.

[123] Said Oucheriah and Liping Guo. PWM-based adaptive sliding-mode control for boost DC-DC converters. *IEEE Transactions on Industrial Electronics*, 60(8):3291–3294, 2012.

[124] Rifqi Firmansyah Muktiadji, Makbul AM Ramli, Houssem REH Bouchekara, Ahmad H Milyani, Muhyaddin Rawa, Mustafa MA Seedahmed, and Firmansyah Nur Budiman. Control of boost converter using observer-based backstepping sliding mode control for DC microgrid. *Frontiers in Energy Research*, 10:828978, 2022.